Assessment and Improvement of Buckling Verification Methods for Monopiles

Master's Thesis

Attila Roth, Hidaya Haj Sassi

Structural and Civil Engineering, 4th June 2025

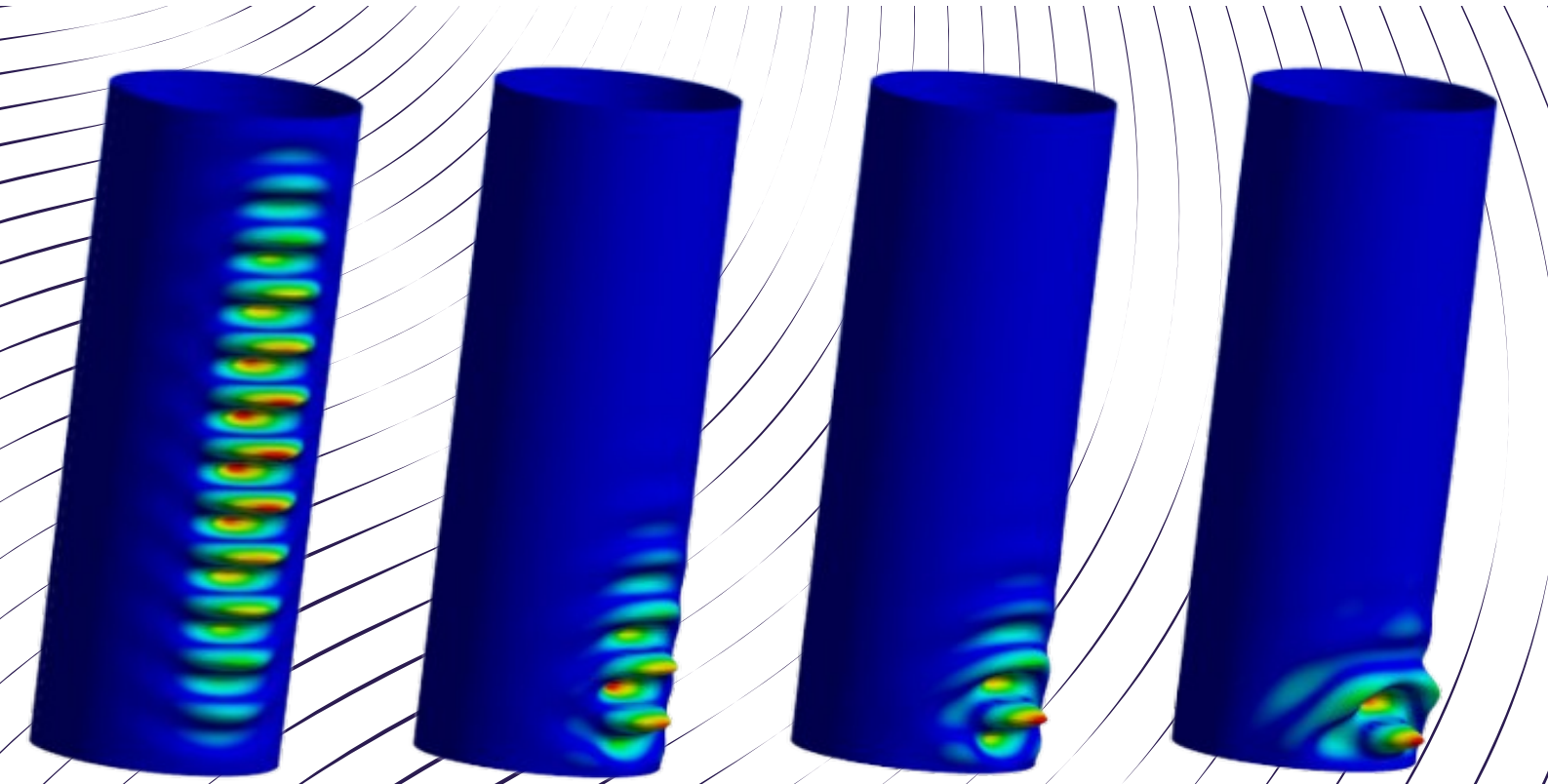

STUDENT REPORT
AALBORG UNIVERSITY

AALBORG UNIVERSITY
STUDENT REPORT

Faculty of Engineering and Science
Department of the Built Environment
Thomas Manns Vej 23
9220 Aalborg East
www.en.build.aau.dk

Title:

Assessment and Improvement of Buckling Verification Methods for Monopiles

Project type:

Master's Thesis

Authors:

Attila Roth
Hidaya Haj Sassi

Supervisors from AAU:

Dario Parigi
Jannie Sønderkær Nielsen

Reference persons from Vattenfall:

Dariusz Eichler
Kashif Kamran Toor

Academic credits:

45 ECTS

Project period:

Autumn 2024 – Spring 2025

Date of completion:

4th June 2025

Abstract:

With the rapid development of the offshore wind energy sector, attention has turned to optimising structural design practices. Current analytical methods for buckling verification of wind turbine supporting structures, e.g. monopiles, are suspected to be more conservative than necessary. In light of that, this project intends to assess the appropriacy of the current calculation methods in EN 1993-1-6 to typical monopiles and revise some of the formulations to reduce conservatism. The objective is pursued using a series of FEA of different types. The results show that the analytical methods are in many cases unconservative when only considering typical monopile geometries, support conditions and geometric imperfections. On the other hand, they become rather conservative when taking more realistic internal force distributions into account. Comparing the simplified case of linearly increasing bending moment with that of uniform bending moment reveals an underestimation of capacity of at least 7%. Improved analytical formulations are presented in the report, but the current topic is far from being exhausted, and researchers are thus encouraged to continue the work.

Keywords: monopiles, cylindrical shells, global bending, buckling, capacity curve, geometric nonlinearity, elastic-plastic, dimple, EN 1993-1-6, RRD, FEA, GMNIA

Published by Aalborg University

Contents

Preface

The present thesis with the title "Assessment and Improvement of Buckling Verification Methods for Monopiles" was prepared by Attila Roth and Hidaya Haj Sassi as completion of their Master's degree in Structural and Civil Engineering at Aalborg University. The project was proposed and initiated by Vattenfall, and the authors' choice was motivated by their devotion to understanding the complex behaviour of load-bearing structures.

As the title suggests, the topic is buckling in monopiles, and the focus is on assessing the currently available analytical buckling verification methods based on a series of advanced finite element analyses. After an introduction in chapter 1 and a thorough background study in chapter 2, the scope of the project is presented in chapter 3. Chapter 4 contains a detailed description of the finite element models, as well as the input and output of the different types of finite element analysis. A systematic assessment of one selected analytical method is included in chapter 5, concluding with a brief comparison with other available methods. Lastly, the effect of certain conditions in monopiles that differ from the assumptions in the analytical methods is investigated in chapter 6. The thesis is completed with a discussion of the findings and a conclusion in chapters 7 and 8, respectively.

This thesis is primarily intended for professionals and researchers within structural engineering who work with or are interested in buckling of steel cylindrical shells, more specifically monopiles or other similar structures. It is hoped that the following discussions and findings will provide valuable insight into the application of common European analytical shell buckling verification methods, including the challenges and potential shortcomings associated with them.

Generative AI was employed in the preparation of the present thesis, primarily for spell-check, grammar-check and paraphrasing for clarity. Furthermore, it was used to assist with IT-related issues and challenges encountered in connection with the numerical analyses.

We are deeply grateful to our supervisors, associate professors Jannie Sønderkær Nielsen and Dario Parigi, for their guidance and support throughout the project. They helped us find and stay on the right path and provided invaluable feedback on the content and structure of our thesis. We would also like to thank Aalborg University for granting us access to the high-performance computing platform UCloud, which is managed by the eScience Center at the University of Southern Denmark. It would have been impossible to perform such a considerable amount of numerical calculations in this relatively short time without it. Finally, we want to thank Vattenfall for initiating the project and providing us with the necessary information.

Attila Roth and Hidaya Haj Sassi
Aalborg, Denmark
4th June 2025

This page is intentionally left blank.

List of Symbols

Symbols used throughout this thesis are listed below, together with the most appropriate units. Other units might also occur. The sign $\sim$ means that units vary depending on the context the symbol is used in.

Latin letters

C_m	end boundary parameter for cylinders in bending	$-$
C_x	end boundary parameter for cylinders in compression	$-$
E	modulus of elasticity	GPa
E_t	tangent modulus	GPa
f_y	yield strength	MPa
f_Ω	length function	$-$
I	moment of inertia (second moment of area)	m^4
L	length (member length, span length, etc.)	m
M	bending moment	MNm
M_{cl}	classical elastic critical moment	MNm
M_{cr}	elastic critical moment	MNm
M_{pl}	plastic moment resistance	MNm
$M_{pl,I}$	plastic moment resistance accounting for imperfections	MNm
M_R	bending moment resistance in general or from FEA	MNm
M_{Rk}	characteristic buckling moment resistance	MNm
$M_{Rk,\mathrm{per}}$	characteristic buckling moment resistance of perfect structure	MNm
Q	fabrication tolerance quality parameter	$-$
r	radius of cylinder's middle surface	m
r/t	radius-to-thickness ratio	$-$
R_{cr}	elastic critical resistance	$\sim$
R_k	characteristic buckling resistance	$\sim$
R_{pl}	plastic resistance	$\sim$
t	cylinder wall thickness	m
V	shear force	MN
W	section modulus	m^3
X, Y, Z	coordinates in Cartesian coordinate system	$-$
R, θ, Z	coordinates in cylindrical coordinate system	$-$

Greek letters

α	elastic buckling reduction factor	$-$
α_G	elastic geometric reduction factor	$-$
α_I	elastic imperfection reduction factor	$-$
β	plastic range factor	$-$

δ_0	geometric imperfection amplitude	m
η	interaction exponent for buckling	–
η_0	squash limit interaction exponent	–
η_p	plastic limit interaction exponent	–
κ	plastic imperfection reduction factor	–
$\overline{\lambda}$	relative slenderness	–
$\overline{\lambda}_0$	squash limit relative slenderness	–
$\overline{\lambda}_p$	plastic limit relative slenderness	–
Λ	linear meridional bending half-wavelength	m
ν	Poisson's ratio in elastic range	–
$\sigma_{x,cl}$	classic elastic critical stress	MPa
$\sigma_{x,cr}$	elastic critical stress	MPa
$\sigma_{x,Rk}$	characteristic axial buckling stress	MPa
χ	buckling reduction factor	–
χ_h	hardening limit	–
ψ	ratio between top and bottom moment	–
ω	first relative length parameter for a cylindrical shell	–
Ω	second relative length parameter for a cylindrical shell	–

Subscripts

$_b$	parameters for cylinders in bending
$_x$	parameters for cylinders in axial compression

1 Introduction

The offshore wind energy sector has undergone significant development over the past decades, and the work still continues. However, there is a notion in the industry that analytical buckling verification methods used nowadays might be overly conservative for wind turbine supporting structures, such as monopiles.

Design codes usually contain detailed rules to follow in order to avoid buckling, and they provide many formulas that can be applied routinely during the design. However, those formulas are often based on certain assumptions and potential approximations and may include empirical and numerical coefficients. Therefore, their range of validity is limited, and they cannot account for all possible design conditions, e.g. specific boundary conditions, cross-sectional force distributions and geometric imperfections, as some of these are implicitly included in the calculation methods.

Conservatism leads to underestimation of a structure's capacity, resulting in unnecessary resource consumption and more expensive solutions. Overly conservative methods might be a result of an attempt to generalise and cover many different cases with one method. On the other hand, conservatism is sometimes inevitable to obtain the required level of safety. In general, less conservative results can be achieved using finite element analysis. However, advanced nonlinear FEA, necessary to appropriately model complex phenomena such as shell buckling, is usually time-consuming and is therefore sometimes avoided. For this reason, the current analytical methods may need to be reevaluated to reduce potential overdimensioning.

In view of the foregoing, the main purpose of the project is to assess and possibly revise the current calculation methods in European standard EN 1993-1-6, which can be applied to evaluate the buckling resistance of steel shells, in order to reduce potential conservatism when used to design monopiles for offshore wind turbines.

Figure 1.1 shows a monopile for an offshore wind turbine before installation, and an extracted monopile that underwent buckling is depicted in Figure 1.2.

Figure 1.1: Monopile before installation [1]

Figure 1.2: Buckling in a monopile [2]

The overall topic of the present project is buckling in monopiles, and similarly to most research projects, it comprises two main parts: a background study and the research. The background study is structured as illustrated in Figure 1.3, where the topic is explored by first investigating the theoretical and historical background of buckling in general as well as buckling in steel cylindrical shells, followed by a comprehensive review of the treatment of shell buckling in European design codes. EN 1993-1-6 provides detailed rules for evaluating the buckling resistance of steel shells in terms of both analytical and numerical methods, and the review covers two different analytical methods, including their comparison, along with a study of various numerical analysis types. To be more precise, the analytical methods in EN 1993-1-6 are in fact semi-analytical or semi-empirical, since many of the expressions are determined by fitting to data from a series of numerical analyses. However, for simplicity, they are referred to as analytical methods throughout this thesis.

The background study is presented in the next chapter, and building on that, the research work, including its scope and findings, is expanded in the remainder of the report.

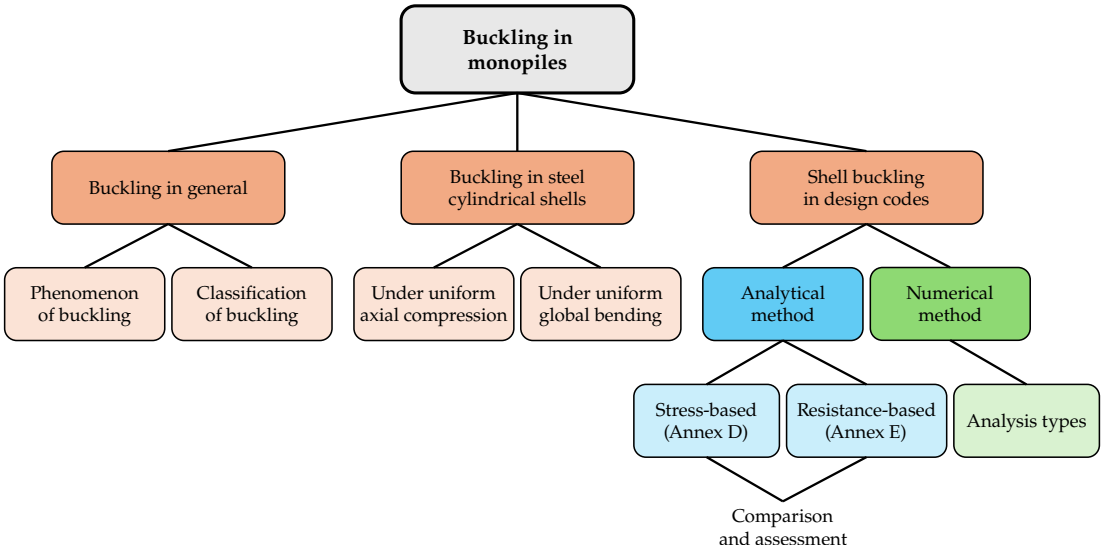

Figure 1.3: Structure of background study in the project

2 Background

2.1 Offshore Wind Turbines

The most common type of foundation for offshore wind turbines (OWT) is monopiles. They are applicable in water depths of up to 40 meters. However, it is claimed that with modern technology, monopiles can be applied in water depths of up to 55 meters [1]. In deeper waters, it is recommended to use other types of foundations, such as jackets or floating foundations.

As shown in Figure 2.1, an offshore wind turbine supported by a monopile consists of three main parts: the monopile, a transition piece and the wind turbine itself. Additionally, a ring stiffener is located between the monopile and transition piece, which is not shown in the figure. Its purpose is both to connect the transition piece and monopile and to stiffen the top of the monopile to avoid unwanted deformation. The parts above sea level are subjected to large horizontal wind loads, while the parts below sea level are subjected to wave and current loads, as illustrated in Figure 2.2.

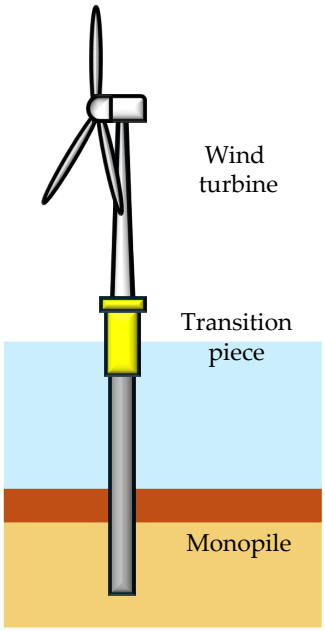

Figure 2.1: Parts of OWT

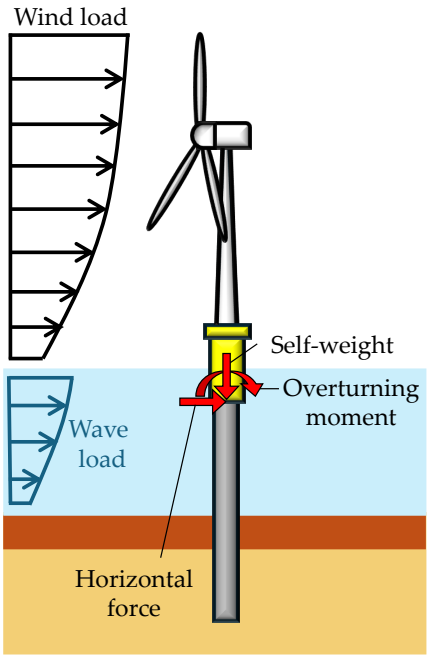

Figure 2.2: Loads on OWT

A monopile supporting an offshore wind turbine acts as a cantilever beam-column subjected to normal forces, shear forces, overturning moments and torsional moments. The normal force corresponds to the self-weight of the whole structure. The large horizontal forces generate similarly large overturning moments and shear forces, and if they act asymmetrically to the OWT, they also cause torsional moments. These forces are transferred through the monopile to the seabed and further into the soil.

The stresses from the loads on top of the monopile are visualised in Figure 2.4. They consist of normal stresses from the normal force and bending moment, and shear stresses from the shear force and torsional moment. The stresses act in the wall of the cylinder.

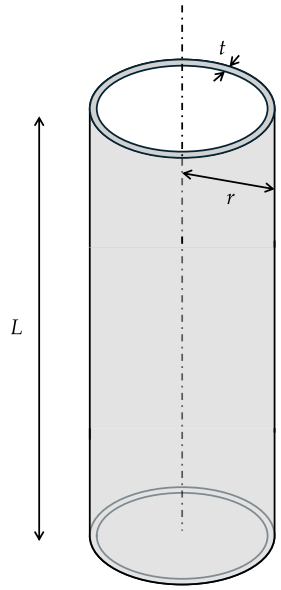

Figure 2.3: Cylindrical shell

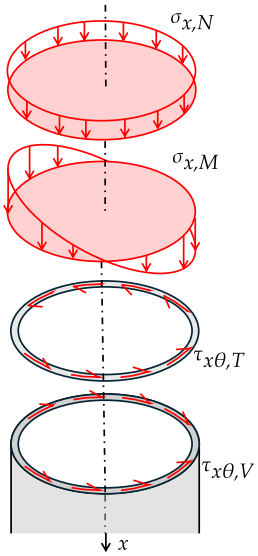

Figure 2.4: Stresses from loads

The geometry of a monopile is quite simple, as shown in Figure 2.3. It is a cylindrical shell defined by three dimensions, namely, the length, the wall thickness and the radius or diameter. The length of the monopile depends on several factors, e.g. the water depth, the soil conditions and the chosen type of connection to the transition piece. The thickness can vary between 50 and 150 mm, and the radius can vary between 2.5 and 6.5 m [3]. According to the information provided by Vattenfall, the typical range of the radius-to-thickness ratio for monopiles is between 35 and 65.

2.2 Buckling In General

2.2.1 The Phenomenon of Buckling

It has long been known that load-bearing members subjected to compression have a tendency to buckle and thus fail due to instability. A classical example is an axially compressed column, which is particularly sensitive to buckling. However, buckling is a collective word and includes numerous phenomena within structural mechanics characterised by extensive flexural and sometimes torsional deformation arising due to compressive stresses. It is an instability problem, that is, the structure or a part of it becomes unstable under a certain load, and in most cases, it happens suddenly and without warning. In general, the load that causes buckling is called the buckling load. Although the process of various buckling phenomena can be essentially different, the physics behind them is the same. When the buckling load is reached, the accumulated strain energy from compressive stresses in the system transforms into bending energy,

causing flexural deformation. Buckling is often associated with structural failure due to the total loss of load-bearing capacity or because of excessive deformation. However, certain structures can have remaining capacity after buckling called post-buckling resistance.

In general, structures can fail as a result of fracture in the material or instability, i.e. buckling. While material failure is controlled by the strength of the material, such as the yield strength or ultimate strength, buckling is practically independent of strength. In order to find out what buckling is governed by, one could refer to Salvadori and Heller [4], who wrote the following:

> *"A slender column shortens when compressed by a weight applied to its top, and, in so doing, lowers the weight's position. The tendency of all weights to lower their position is a basic law of nature. It is another basic law of nature that, whenever there is a choice between different paths, a physical phenomenon will follow the easiest path. Confronted with the choice of bending out or shortening, the column finds it easier to shorten for relatively small loads and to bend out for relatively large loads. In other words, when the load reaches its buckling value the column finds it easier to lower the load by bending than by shortening."*

Even though the language of these remarks is somewhat subjective, and they contain non-technical terms, they also capture the essence of the problem. In more technical terms, it could be reformulated as follows: *A basic law of nature is that systems take the path of least resistance when they deform* [5]. Since a system's or structure's ability to resist deformation is its stiffness, it infers that buckling is governed by a structure's stiffness. As opposed to strength, stiffness is an extensive property of a structure, which means that it depends not only on the structure's material but its geometry and boundary conditions as well. [5–7]

2.2.2 Classification of Buckling

Since buckling is a broad term, it can be classified based on different aspects, some of which are illustrated with a mind map in Figure 2.5.

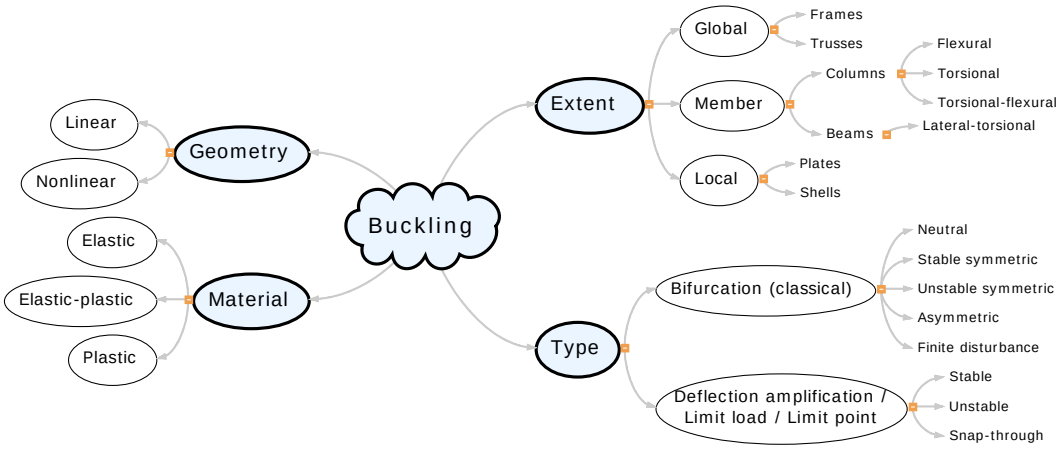

Figure 2.5: Classification of buckling — Mind map

Extent of buckling

Based on its extent, buckling can be labelled as global, member or local. Examples of each are shown in Figure 2.6. Global buckling, in some contexts called sway buckling, can for instance be observed in unbraced frames, and it is characterised by considerable relative displacement of member ends. [8]

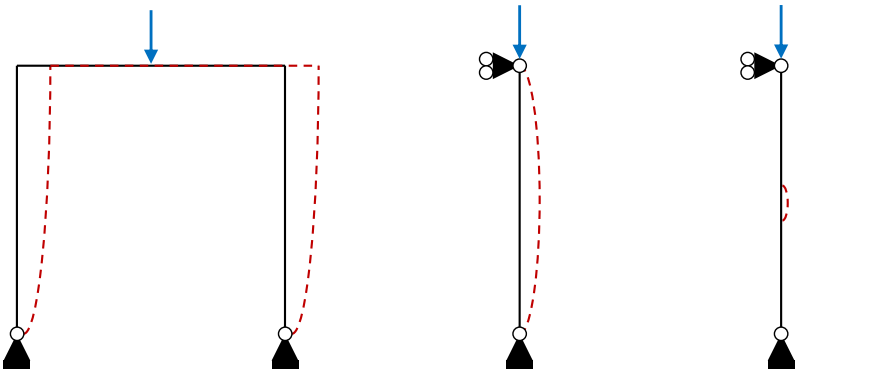

a) Global buckling (sway buckling of frame)

b) Member buckling (flexural column buckling)

c) Local buckling

Figure 2.6: Examples of classification based on extent

Member buckling is the classical buckling, where a slender member buckles under axial compression (column) or bending (beam). Depending on the shape of their cross-section, columns can exhibit flexural, torsional or torsional-flexural buckling, as shown in Figure 2.7. Flexural buckling is characterised by deflection about the minor axis of the member or about the major axis of laterally restrained members, and it can occur in members with any cross-sectional shape. Torsional buckling is associated with a twist of the cross-section, while torsional-flexural buckling involves both deflection and twist. The latter two are possible in members with asymmetric, single symmetric or cruciform cross-sections, e.g. L, T, U or X-shaped, as well as doubly-symmetric cross-sections with lateral restraints. [8]

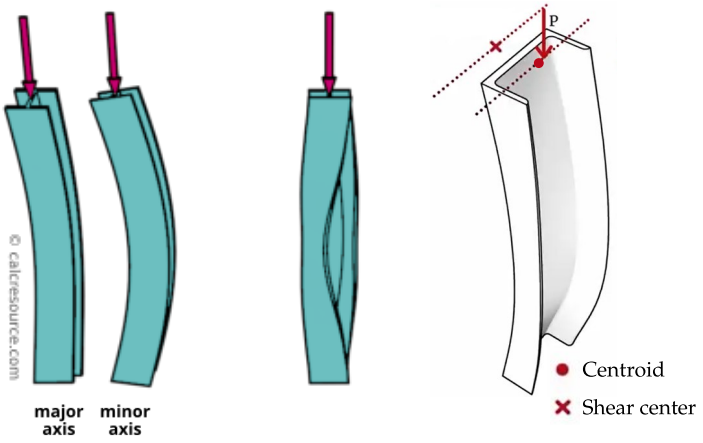

a) Flexural buckling

b) Torsional buckling

b) Torsional-flexural buckling

Figure 2.7: Examples of column buckling [9, 10, ed.]

Buckling in beams due to major axis bending is called lateral-torsional buckling. As illustrated in Figure 2.8, it is characterised by deflection of the flange where compressive stresses are present and a twist of the cross-section due to the stabilising effect of the tension flange. It primarily affects beams with open cross-sections, e.g. I, H and U-shaped, whereas beams with closed cross-sections, such as hollow sections and welded box sections, are not susceptible to lateral-torsional buckling [8].

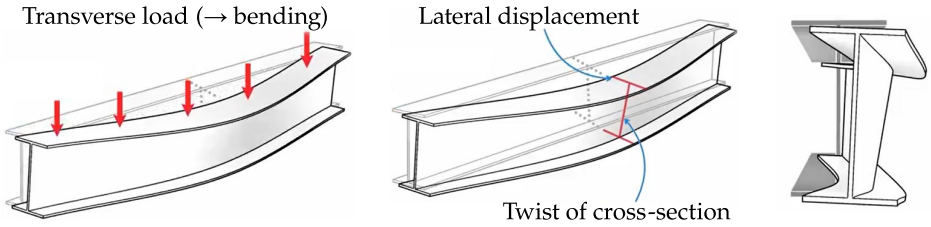

Figure 2.8: Example of lateral-torsional buckling [10, ed.]

Buckling can also occur locally in a slender part of a member's cross-section, limiting its resistance and rotation capacity [8]. Depending on the shape of the component that buckles, local buckling can be labelled as plate or shell buckling. Plates are nominally flat [11], while shells have a curved shape [12]. It is important to note that both plates and shells can experience buckling affecting them as a whole, e.g. as a column, which phenomenon is identical to member buckling. Examples of buckling in an axially compressed plate and shell are shown in Figures 2.9 and 2.10, respectively, including a visualisation of the difference between local and member buckling in these elements. In some contexts, the terms buckling of plates or shells may be used to mean both member and local buckling. Furthermore, the terms global and local buckling can in some literature or standards also be used differently than described here.

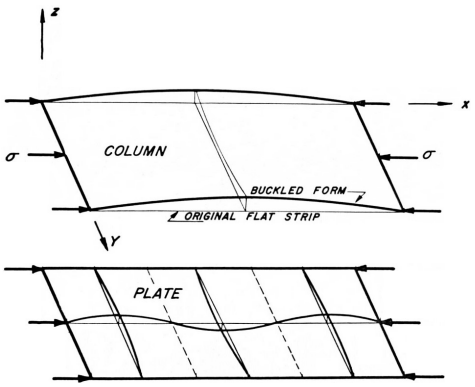

Figure 2.9: Buckling in plates [13]

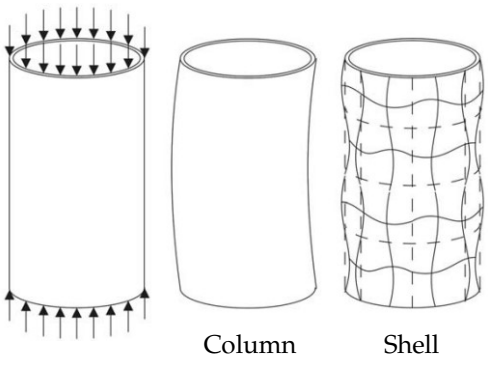

Figure 2.10: Buckling in shells [14]

Types of buckling

The phenomenon of buckling can be divided into different types or subphenomena. However, there is no universal consensus about the division. Technical working group 8.4 of ECCS [15], for example, defined two types of buckling, namely bifurcation and snap-through. Yoo and Lee [6] used the term deflection-amplification instead of

snap-through, covering a wider range of phenomena. Jerath [5] called it limit load, and extended the list with a so-called finite disturbance buckling. In this thesis, the authors decided to consider two fundamental types of buckling, namely bifurcation and deflection-amplification, together with different post-buckling behaviours, including e.g. snap-through and finite disturbance, as shown in the mind map in Figure 2.5. The following descriptions are based on the above-mentioned references [5, 6, 15]

Bifurcation-type buckling is the classical form of buckling characterised by a bifurcation point, where the primary or pre-buckling equilibrium path of a structure is intersected by a secondary or post-buckling path, as shown in Figure 2.11. The figure depicts examples of load-deformation curves in terms of axial compression versus lateral deformation, i.e. deflection. On the primary path, axial force normally leads to axial displacement and no deflection. However, a small lateral perturbation can cause the deformations to change to an alternate configuration referred to as buckling mode, and thus the response follows the secondary path. The load at the bifurcation point is usually called bifurcation load or critical load. The post-buckling response after bifurcation can either be neutral with zero stiffness a), stable symmetric with positive stiffness regardless of buckling mode b), unstable symmetric with negative stiffness regardless of buckling mode c), asymmetric with either positive or negative stiffness depending on the buckling mode d), or a combination of stable and unstable called finite disturbance with the stiffness first negative then becoming positive e). The letters for the different responses refer to the load-deformation curves shown in Figure 2.11. When a structure's stiffness is positive, it means that increasing loads lead to increasing deformations. Following the same logic, zero stiffness means increasing deformations with no change in loads, while negative stiffness means increasing deformations with decreasing loads.

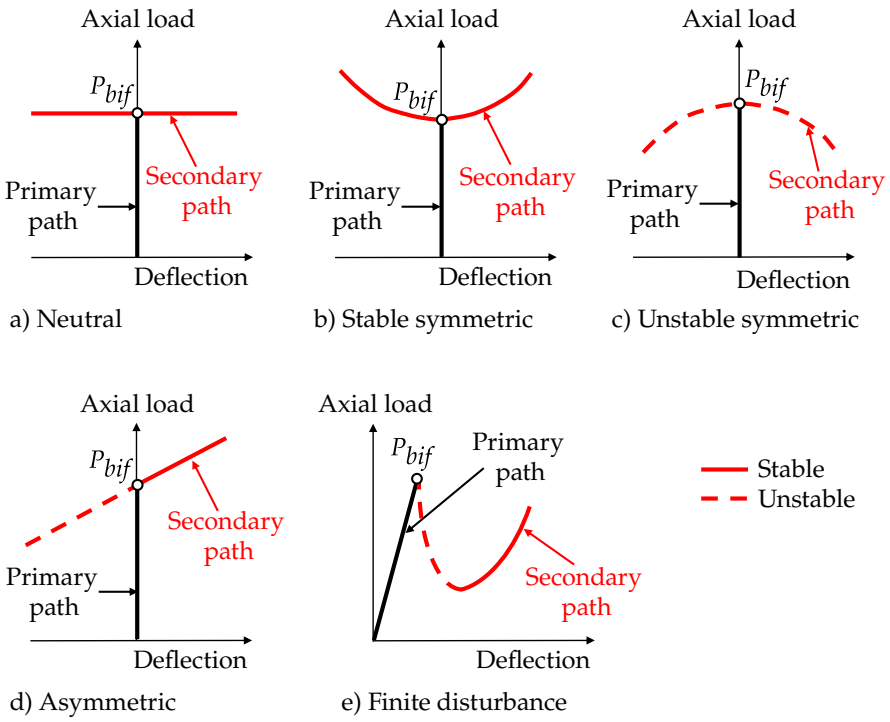

Figure 2.11: Load-deformation curves for bifurcation-type buckling [5, ed.]

Member buckling and plate buckling are typically characterised by stable symmetric or, in some cases, neutral post-buckling response, whereas most shells exhibit unstable symmetric bifurcation or finite disturbance buckling. Asymmetric bifurcation can be encountered if the secondary path is affected by the direction of the alternate deformation configuration, as in asymmetric structures, members or parts.

Bifurcation-type buckling can mostly only be observed in perfect or near-perfect structures. If imperfections are present, bifurcation is suppressed and deflection-amplification-type buckling occurs instead, as illustrated with load-deformation curves in Figure 2.12, where ε denotes the imperfection amplitude. Furthermore, deflection-amplification-type buckling also arises in structures with deflection prior to buckling caused by eccentricity or lateral loading, e.g. in spherical caps and arches. In these cases, the deformation configuration is predefined by the imperfections or the lateral loading, and thus deflection-amplification-type buckling is characterised by one single equilibrium path. As the name implies, the configuration of pre- and post-buckling deformations is the same, it is only the magnitude that keeps increasing after buckling. Similarly to bifurcation-type buckling, the post-buckling response can either be stable with positive stiffness a) & b), unstable with negative stiffness a) & c), or a combination of the two called snap-through with first negative then positive post-buckling stiffness d), as shown in Figure 2.12. In case of unstable and snap-through response, the load at buckling is referred to as limit load and is typically lower than the bifurcation load in the corresponding perfect system. In case of stable response, there is usually no apparent buckling load, although the bifurcation load of the corresponding perfect system can be considered as a reasonable lower bound.

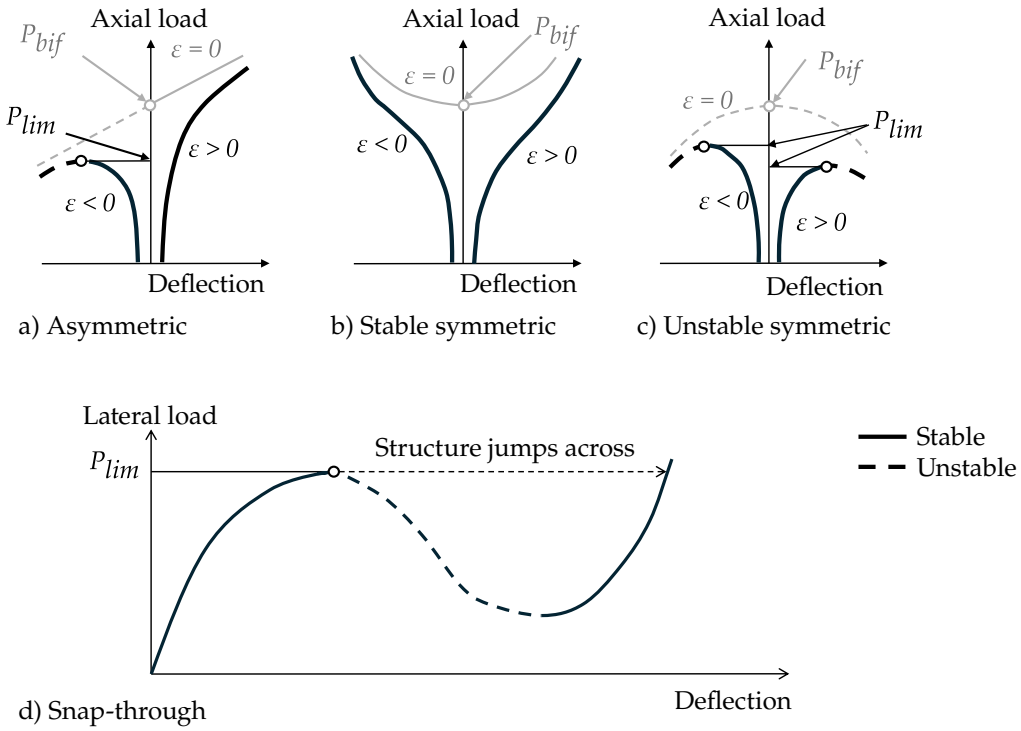

Figure 2.12: Load-deformation curves for deflection-amplification-type buckling [15, ed.]

Response of structure

Considering the response of a structure to loading, i.e. change in its geometry, buckling can be classified as either linear or nonlinear. In linear buckling, deflection prior to buckling is negligibly small, whereas it is considerable in case of nonlinear buckling. For example, a perfect centrally loaded elastic column responds linearly to axial loading, whereas by introducing an eccentricity to the load, the response changes to nonlinear as a result of the induced deflection. It should be noted that most real structures exhibit nonlinear buckling as a result of inevitable geometric imperfections and eccentricity of loading, and the assumption of linear buckling in certain cases produces unconservative results and unsafe design. That is especially true for structures experiencing unstable post-buckling behaviour. Furthermore, it should be mentioned that bifurcation-type buckling can occur in both linear and nonlinear cases, while deflection-amplification-type buckling is only possible in the nonlinear case, as shown in Figure 2.13.

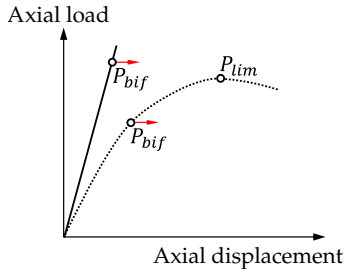

Figure 2.13: Example of linear and nonlinear buckling on axial load-displacement curve

Response of material

Considering the response of the material, buckling can be classified as elastic, plastic or elastic-plastic. In general, buckling in the elastic region is called elastic, and in the plastic region with hardening is called plastic. However, in a transitional region in between, local yielding and plasticity can influence buckling, and it is in that case classified as elastic-plastic. For instance, a short column or a semi-long column with a compact cross-section can most likely be loaded beyond yielding into the plastic region without buckling. In contrast, a long column or a semi-long column with a slender cross-section would probably buckle before the material's yield strength could be reached, i.e. within the elastic region, as illustrated in Figure 2.14.

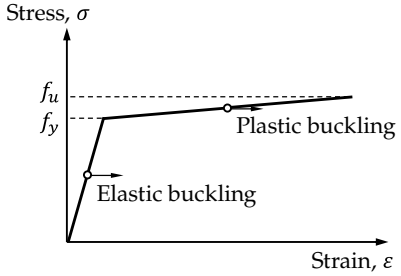

Figure 2.14: Example of elastic and plastic buckling on stress-strain curve

2.3 Buckling in Steel Cylindrical Shells

Steel cylindrical shells are widely used structural elements, e.g. as chimneys, piles, wind turbine towers, silos and tanks, and depending on their application, they can be subjected to different loading arrangements. Thereby, buckling in those structures can be essentially different. The two probably most common and also extensively studied simple load conditions in steel cylinders are uniform axial compression and uniform global bending, which are discussed in the following. This section focuses solely on elastic buckling in perfect steel cylindrical shells but considers both linear and nonlinear phenomena. The complex influence of plasticity and geometric imperfections is usually accounted for using semi-analytical methods from design codes, as discussed in the next section.

2.3.1 Uniform axial compression

Cylindrical shells under uniform axial compression can exhibit flexural column buckling, local shell buckling or local plate buckling depending on their relative length, as illustrated in Figure 2.15 for a perfect shell with a radius-to-thickness ratio of 100, assuming linear structural response. Since geometric nonlinearity and imperfections are disregarded, the shell exhibits bifurcation-type buckling. Two dimensionless length parameters are commonly used to describe the length relative to the radius and thickness, as shown in (2.1). If the length is large compared to the radius, the shell is long and will buckle as a column. If the length is small compared to the radius, the shell will behave like an infinitely wide plate strip and buckle locally as a plate. In the intermediate region where the length is neither large nor small compared to the radius, local shell buckling occurs as depicted on the two cylinders in Figure 2.15.

$$\omega = \frac{L}{r}\sqrt{\frac{r}{t}} = \frac{L}{\sqrt{rt}} \qquad \text{and} \qquad \Omega = \frac{L}{r}\sqrt{\frac{t}{r}} = \omega\frac{t}{r} \tag{2.1}$$

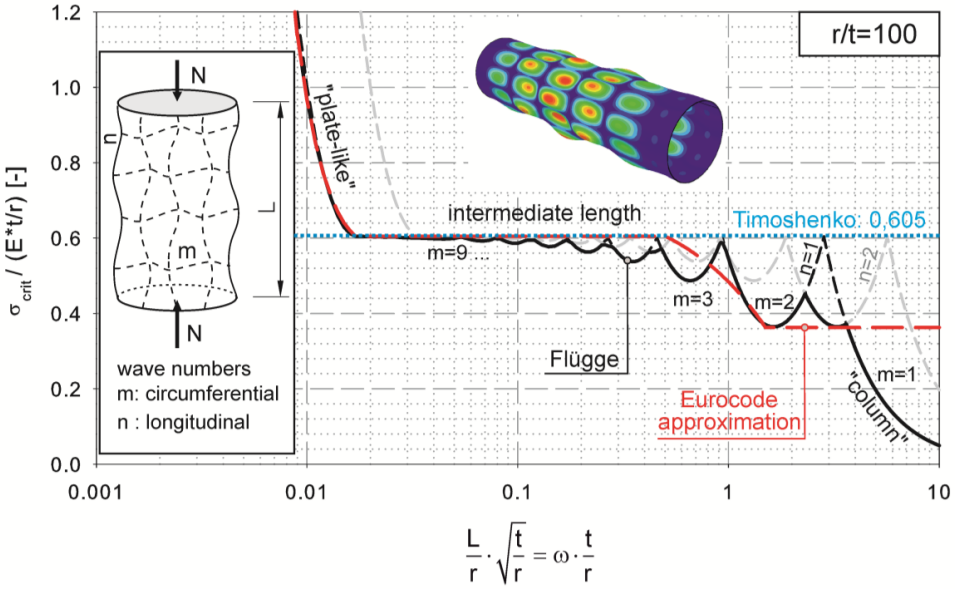

Figure 2.15: Normalised elastic critical axial stress acc. to linear buckling theories [16]

Historically, buckling of columns was studied extensively relatively early. In the 18th century, Euler studied elastic buckling in bars and columns, and he presented the first accurate column analysis in 1744. From the analysis, an expression was derived to estimate the critical load where flexural column buckling occurs [6]. Shell buckling started to get more attention later. The normal stress at linear elastic bifurcation in a perfect axially compressed cylinder of medium length under ideal boundary conditions was independently found by Lorenz in 1908, Timoshenko in 1910 and Southwell in 1914. It is known as the classical elastic critical stress and can be calculated as shown in eq. (2.2). [17]

$$\sigma_{x,cl} = \frac{E}{\sqrt{3(1-\nu^2)}}\frac{t}{r} \approx 0.605E\frac{t}{r} \tag{2.2}$$

More sophisticated shell buckling theories encompassing the effects of varying length and boundary conditions were presented later in the previous century, e.g. by Flügge in 1932 and Donnell in 1933. According to the Flügge theory, several buckling modes with almost identical elastic critical stresses exist with varying circumferential and longitudinal wave numbers m and n, as shown in Figure 2.15. By looking at the plot, it can also be seen that buckling modes with fewer circumferential waves occur at lower critical stresses and that those stresses can be up to 40% lower than the classical elastic critical stress. While the original Flügge theory only applies to linear elastic buckling phenomena, Donnell's theory also considers geometric nonlinearity but has other deficiencies, as discussed by Yamaki [18].

Yamaki presented a comprehensive summary of the nonlinear elastic stability of circular cylindrical shells under torsion, pressure and compression in 1984 [18]. According to his work using a modified version of the Flügge theory, the combined effect of varying length, boundary conditions and geometric nonlinearity on the classical elastic critical stress is as visualised in Figure 2.16. Eight different boundary conditions are considered in the figure: four simply supported (S1–S4) and four clamped (C1–C2). Two material-dependent relative length parameters are used as variables, which are closely related to the previously presented ω and Ω, as shown in (2.3). Assuming $\nu = 0.3$, the relationships become as in (2.4). The plots show curves with connected festoons similar to Figure 2.15, although in a seemingly more irregular pattern. In the intermediate length range, the ratio between the nonlinear elastic critical stress and the classical elastic critical stress becomes almost constant for each boundary condition. Also note that the plots include curves for $r/t = 100$ and $r/t = 1\,000$, but only a slight difference can be observed between them indicating that the ratio $\sigma_{x,cr,NL}/\sigma_{x,cl}$ expressed as a function of Z or Λ is independent of r/t.

$$\begin{aligned} Z &= \sqrt{1-\nu^2}\,\frac{L^2}{rt} = \sqrt{1-\nu^2}\,\omega^2 \\ \Lambda &= \sqrt{Z}\,\frac{t}{r} = \sqrt[4]{1-\nu^2}\,\omega\frac{t}{r} = \sqrt[4]{1-\nu^2}\,\Omega \end{aligned} \tag{2.3}$$

$$\begin{aligned} Z &= \sqrt{1-0.3^2}\,\omega^2 \approx 0.954\,\omega^2 \\ \Lambda &= \sqrt[4]{1-0.3^2}\,\Omega \approx 0.977\,\Omega \end{aligned} \tag{2.4}$$

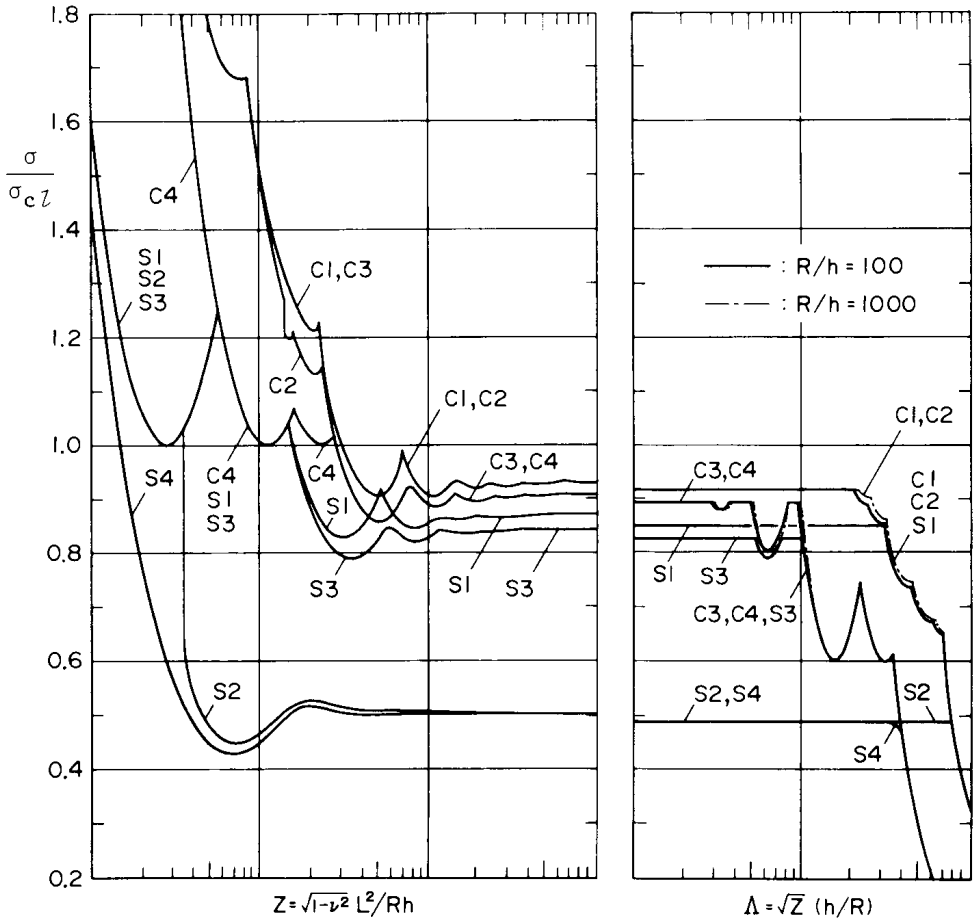

Figure 2.16: Normalised nonlinear elastic critical axial stress acc. to Yamaki [18, ed.]

The different shell theories have served as basis for the rules and calculation methods in design codes used nowadays. For example, in the current edition of EN 1993-1-6 [12], a simplified version of the original Flügge theory is applied together with the classical approximation (Timoshenko) at high number of waves m to calculate the axial linear elastic critical stress, as illustrated in Figure 2.15. In the future edition of EN 1993-1-6, currently available in draft version [19], the calculation method was further simplified by using the classical approximation for low values of m as well. In the standard, the elastic critical stress is defined as the product of its classical value and the coefficient C_x, see (2.5). The effect of geometric nonlinearity is included using the coefficient α_{xG} set to a constant 0.83, most likely based on Yamaki's work [18].

$$\sigma_{x,cr} = C_x \sigma_{x,cl} \approx 0.605 C_x E \frac{t}{r} \tag{2.5}$$

$$\sigma_{x,cr,NL} = \alpha_{xG} \sigma_{x,cr} = 0.83 \sigma_{x,cr} \tag{2.6}$$

It should be emphasised that the above-discussed buckling resistances are mainly theoretical in case of elastic bifurcation-type buckling of perfect cylinders. In reality, geometric imperfections and plasticity typically have a significant negative effect, resulting in a reduced buckling resistance. This fact has long been known, and in the previous century, the professional community tried to gain more knowledge about the matter using experiments. Despite the fact stated in a recent research paper that

axially compressed cylinders have historically been the most tested shell systems producing the largest test dataset [20], these experimental data do not provide a suitable basis for either deriving analytical calculation methods or reliably calibrating partial safety factors. The reason for that is the large scatter observed in the results, as seen in Figure 2.17, and the fact that important information about the specimens was not recorded to explain it properly. Therefore, it has become more common in the last decade to use results from numerical calculations rather than experiments for the above-mentioned purposes.

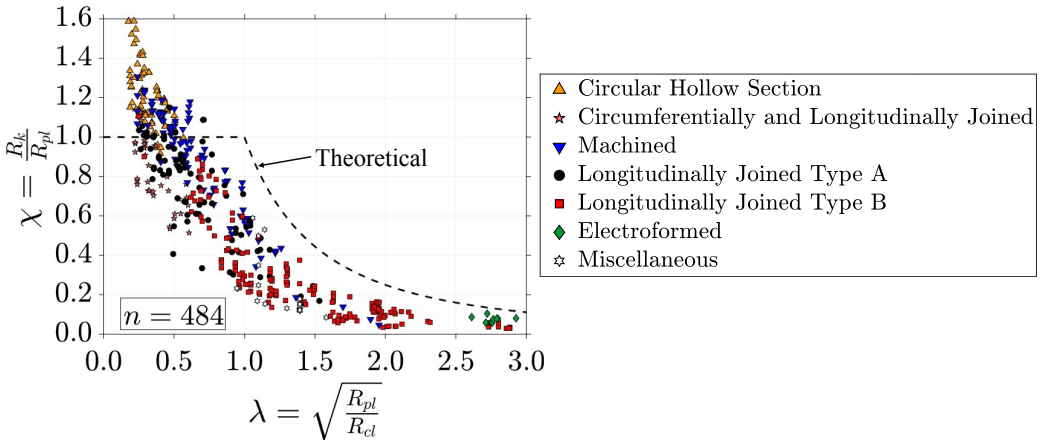

Figure 2.17: Test results for cylinders under axial compression [20, ed.]

2.3.2 Uniform global bending

When dealing with cylinders in uniform global bending, the critical load where buckling occurs is commonly expressed as an internal force (bending moment) rather than a stress. Even though the classical elastic critical stress $\sigma_{x,cl}$ in (2.2) was derived for a cylinder in uniform axial compression, its product with the elastic section modulus W_{el} is typically employed as a reference resistance. It is called the classical elastic critical moment M_{cl} and can be calculated as shown in (2.7). Note that an approximate value of the elastic section modulus is used in the equation, which provides an adequate estimate for thin-walled cylinders.

$$M_{cl} = \sigma_{x,cl} W_{el,shell} = \frac{E}{\sqrt{3(1-\nu^2)}} \frac{t}{r} \pi r^2 t = \frac{\pi}{\sqrt{3(1-\nu^2)}} E r t^2 \approx 1.901 E r t^2 \tag{2.7}$$

As opposed to uniform axial compression, cylinders in uniform global bending do not exhibit member buckling or local plate buckling, only local shell buckling, which results in a slightly more straightforward relationship between the linear elastic critical moment M_{cr} and its classical approximation M_{cl}. Despite that, the difference between the two moments was first studied only recently by Rotter et al. [21], who defined a conservative approximation of the ratio as shown in (2.8) for cylinders with clamped end supports. They claim that the relationship is effectively independent of the r/t ratio when expressed in terms of ω. However, a small scatter can be observed when looking closely at Figure 2.18. Fajuyitan et al. have later investigated the effect of boundary conditions and presented a curve with clear festoons when using simple

end supports for $r/t = 100$ as shown in Figure 2.19, which suggests that the scatter in Figure 2.18 is not random and that there may indeed be a dependency on r/t.

$$\frac{M_{cr}}{M_{cl}} = 1 + \frac{4}{\omega^2} \tag{2.8}$$

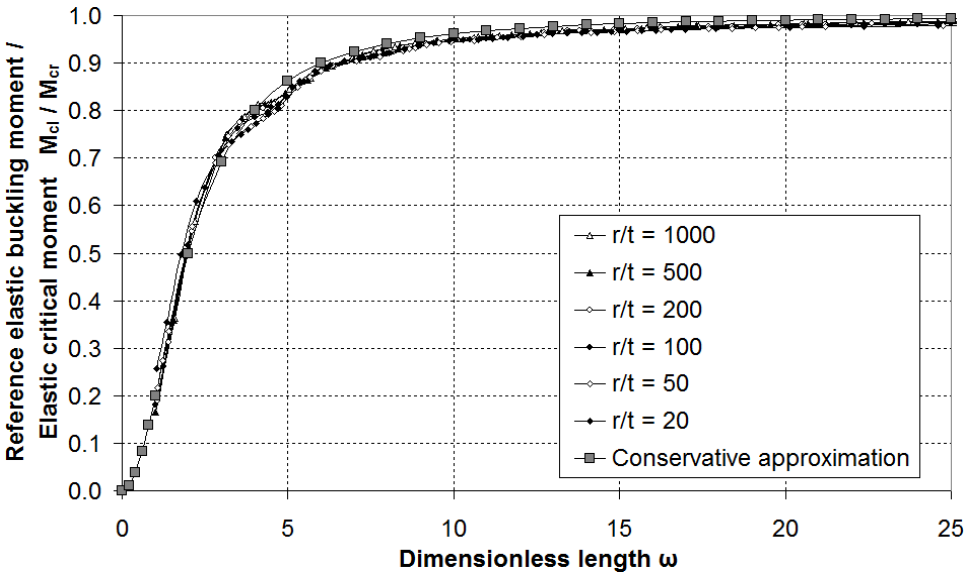

Figure 2.18: Ratio of M_{cl} to M_{cr} for different r/t ratios [21]

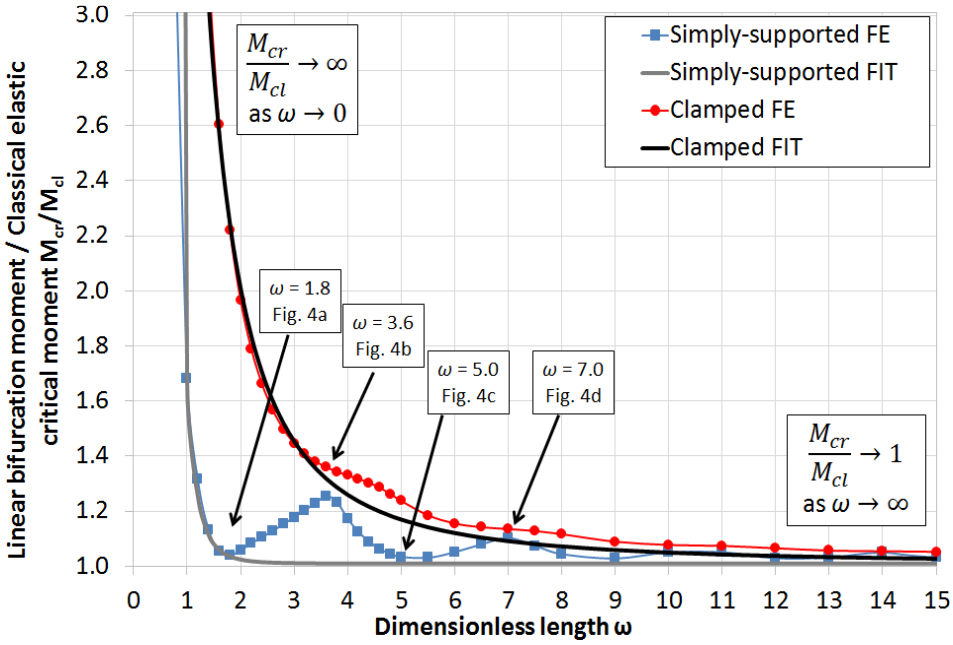

Figure 2.19: Ratio of M_{cr} to M_{cl} for different support conditions [22]

When accounting for geometric nonlinearity in cylinders under global bending, the buckling behaviour becomes complex due to the coupling between cross-sectional ovalisation and local bifurcation-type buckling as recently described by Rotter et al.

[21]. Even though that research paper is from 2014, analytical treatments of this phenomenon have a history of around a century. Only a brief discussion of the problem's theoretical background is included in the following, mainly based on the findings of Rotter et al. [21]. For more details, the reader is referred to the cited paper.

Cylindrical shells under global bending exposed to nonlinear buckling can exhibit snap-through buckling, local bifurcation-type buckling, instability due to cross-sectional ovalisation or a combination of the latter two, depending on their relative length. According to Rotter et al. [21], as well as based on earlier studies, four distinct domains of this behaviour can be identified and described as follows:

- In short cylinders, the end boundaries effectively restrain both local bifurcation-type buckling and cross-sectional ovalisation. According to Rotter et al. [21], they experience snap-through buckling caused by significant geometric softening due to the growth of a central meridional fold at moments considerably higher than M_{cr}, see Figure 2.20. Cylinders are classified as short up to $\omega \approx 5$, although such geometries are rarely used in practice.

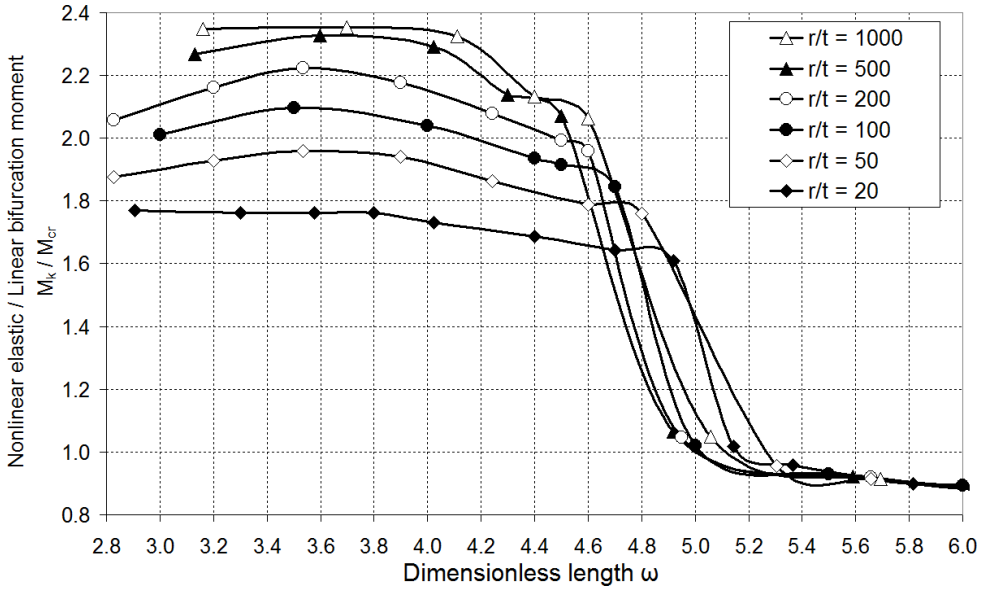

Figure 2.20: Ratio of nonlinear and linear elastic buckling moments in short cylinders [21]

- In medium-length cylinders, the end boundaries still restrain cross-sectional ovalisation, but allow local bifurcation buckling. Thus, buckling occurs at moments close to M_{cr}. As seen in Figure 2.21, the relationship between the nonlinear and linear elastic buckling moments can be visualised as a curve of connected festoons corresponding to distinct buckling modes. The fluctuation decreases with increasing length and eventually settles on a plateau. Rotter et al. [21] proposed the upper boundary of the medium-length domain to be at $\omega \approx 0.5\, r/t$, or more naturally expressed in terms of the second relative length as a single value $\Omega \approx 0.5$, as shown in Figure 2.22. This is, however, only valid for $r/t \geq 50$, since in cylinders with ratios below that, the curve of festoons

cannot reach a horizontal plateau before it enters the transitional domain and ovalisation begins.

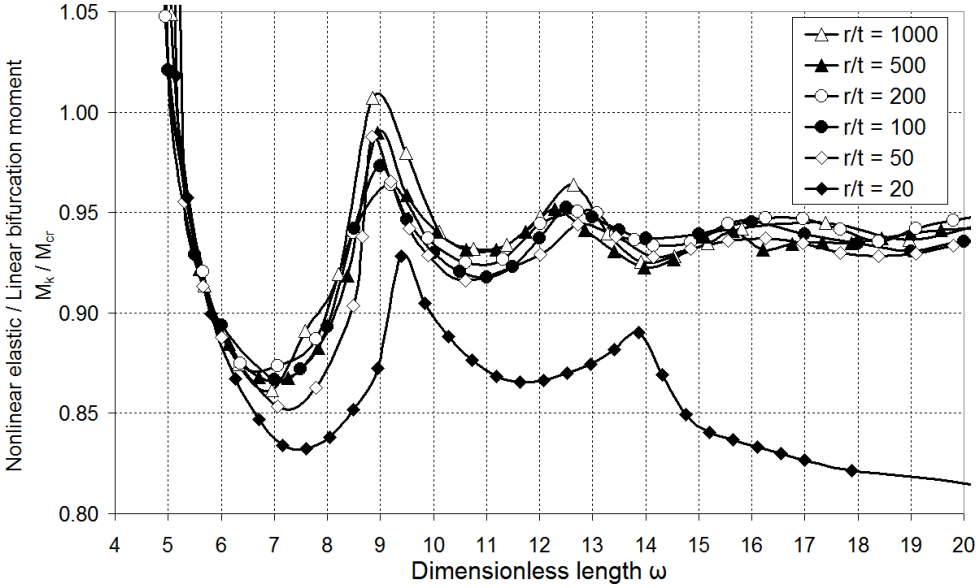

Figure 2.21: Ratio of nonlinear and linear elastic buckling moments in medium-length cylinders as a function of ω [21]

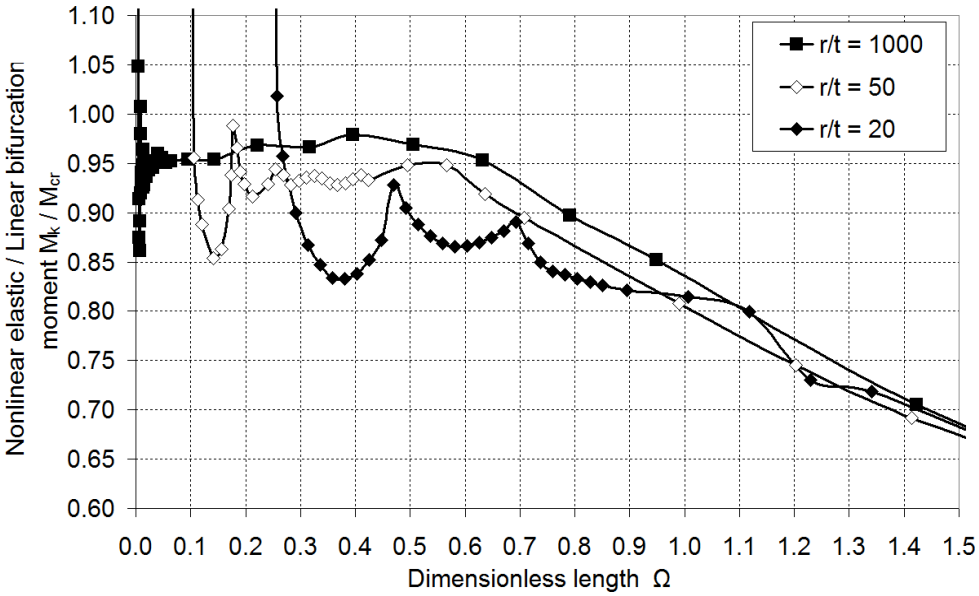

Figure 2.22: Ratio of nonlinear and linear elastic buckling moments in medium-length cylinders as a function of Ω [21]

- In transitional-length cylinders, the restraining effect of end boundaries against cross-sectional ovalisation diminishes gradually, leading to a decrease in lever arm and section modulus, and thus to a lower buckling moment. Cylinders in this domain follow more or less the same curve regardless r/t ratio when expressed as a function of Ω, as depicted in Figure 2.23. It starts as a straight

line before smoothly approaching a minimum value of approx. 0.49 at $\Omega \approx 3.5$ and gently rising to a constant at the boundary at $\Omega \approx 7$.

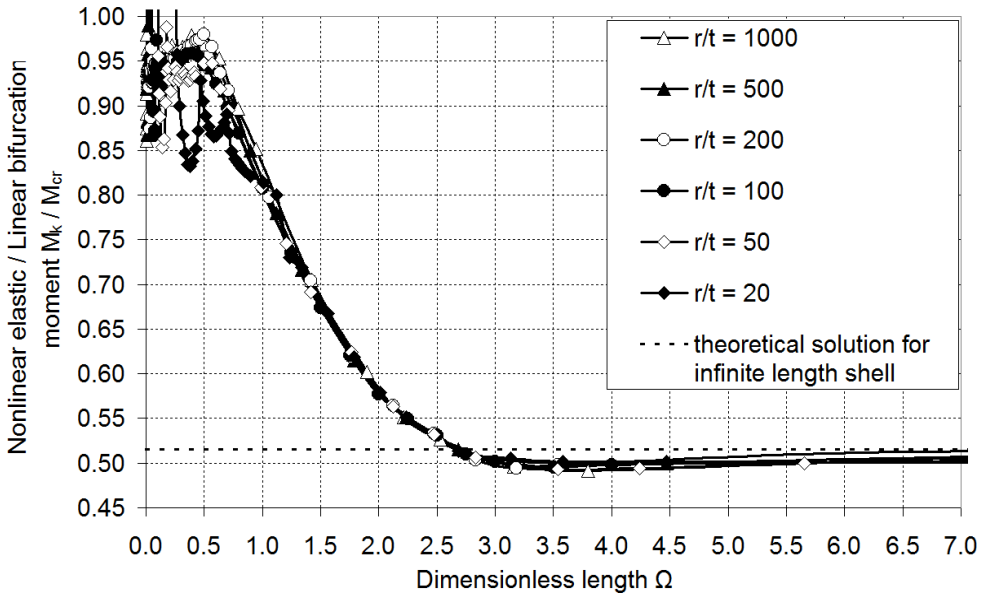

Figure 2.23: Ratio of nonlinear and linear elastic buckling moments in transitional-length cylinders [21]

- Long cylinders undergo considerable ovalisation, whose effects become stable, meaning that the length no longer affects the buckling resistance. Buckling always occurs as bifurcation at a moment approximately equal to $0.5M_{cr}$. Several theoretical solutions have been published for the asymptotic moment in infinitely long cylinders over the years. Based on their numerical results, Rotter et al. chose the value of 0.516 corresponding to the analytical solution of Tatting et al. (1997) and Li and Kettle (2002).

Based on their study, including finite element analysis of clamped cylinders with a wide range of dimensions, Rotter et al. [21] proposed the following algebraic expressions for the ratio of nonlinear and linear elastic buckling moments $\alpha_{bG} = M_k / M_{cr}$ valid for $r/t \geq 50$:

$$\alpha_{bG} = \begin{cases} 1.93 - 0.5(\omega - 3.8)^2 - 0.44(\omega - 3.8)^3 & \text{for short: } 3 \leq \omega < 4.8 \\ 0.85 + 0.029(\omega - 7.1)^2 & \text{for med.: } 4.8 \leq \omega < 8.6 \\ 0.92 & \text{for med.: } 8.6 \leq \omega < 0.5(r/t) \\ 1.07 \dfrac{1 - 0.22\Omega + 0.061\Omega^{2.94}}{1 + 0.12\Omega^{2.94}} & \text{for trans.: } 0.5 \leq \Omega < 7.0 \\ 0.516 & \text{for long: } \Omega \geq 7.0 \end{cases} \tag{2.9}$$

The analytical method in the current edition of EN 1993-1-6 [23] adopted the expressions above for α_{bG} as well as for the ratio M_{cr}/M_{cl}, which was assigned the symbol C_m. Similarly to the case of uniform axial compression, the future edition of EN 1993-1-6 [19] conservatively sets $C_m = 1$ and also simplifies the expression for α_{bG}.

2.4 Treatment of Buckling in Design Codes

The different types of buckling presented earlier can be handled using the rules and calculation methods described in design codes. In Europe, the commonly used design codes are the Structural Eurocodes. The design of steel structures shall follow the rules and methods given in EN 1993 Eurocode 3, some parts of which deal specifically with buckling. EN 1993-1-1 [8] deals with global buckling and buckling of members with standard cross-sections. As for buckling of plates, EN 1993-1-5 [11] can be applied. Design of shells against buckling is handled in EN 1993-1-6 [12], where three approaches are provided, namely an analytical, a numerical and a combined one. There are also other approaches for dealing with the buckling strength of shells, e.g. a semi-empirical approach presented in the recommended practice DNVGL-RP-C202 [24], which generally applies to shell structures with stiffeners. In this project, attention is directed towards the approaches defined in EN 1993-1-6.

At the time of writing (March 2025), the first edition of EN 1993-1-6, namely EN 1993-1-6:2007, is in effect together with corrigendum EN 1993-1-6:2007/AC:2009 and amendment EN 1993-1-6:2007/A1:2017. However, its second edition is in the last phase of preparation and is expected to be published later in 2025. The authors of this report have access to an official draft version of the second edition, prEN 1993-1-6:2023, and use it as background for the project. Furthermore, a recent research paper by Sadowski and Filippidis [25] is also employed, whose first author contributed significantly to the second edition, and in that context, it is referred to as EN 1993-1-6:2025. Where no specific year is stated, general reference is intended to EN 1993-1-6.

In the following, a summary of the different types of numerical analysis defined in the standard is presented first. Thereafter, buckling-relevant geometric tolerances are described together with the treatment of geometric imperfections in the calculation methods. Lastly, a description is provided for the three approaches in EN 1993-1-6, which include design by means of:

- a fully analytical calculation using buckling stresses or reference resistances
- a fully numerical geometrically and materially nonlinear analysis including imperfections (GMNIA)
- a linear bifurcation analysis (LBA) and a materially nonlinear analysis (MNA) combined with the analytical method

2.4.1 Types of Numerical Analysis

Numerical analyses involve calculations performed using the finite element method, among others, to describe the behaviour of a loaded structure in terms of stresses, deformations and stability. Several numerical approaches to examine steel shells are defined in EN 1993-1-6 with different aims. A short description of each approach can be found below based on ECCS No. 125 [15] and prEN 1993-1-14:2023 [26].

Linear elastic shell analysis (LA)

LA predicts the behaviour of a perfect shell structure based on the small deflection linear elastic shell bending theory. This implies that the assumed geometry remains that of the undeformed structure. An LA fulfils static and kinematic equilibrium. When stresses are in equilibrium, the static condition is fulfilled. As for the kinematic condition, it is satisfied when there is compatibility of strains.

Linear elastic bifurcation analysis (LBA)

LBA resembles LA as the analysis is based on the small deflection linear elastic shell bending theory, meaning that static and kinematic conditions are met, and the material law is also linear elastic. This analysis differs as it evaluates the linear bifurcation eigenvalue of the structure, which corresponds to the bifurcation load R_{cr}.

Geometrically nonlinear elastic analysis (GNA)

GNA meets both static equilibrium and kinematic compatibility, including when changes appear in geometry caused by loading. The analysis is performed on a perfect structure using the principles of shell bending theory and linear elastic material law, as well as including nonlinear large deflection theory. This type of analysis can be used to identify a bifurcation load reduced due to geometric nonlinearity or a possible limit load.

Materially nonlinear analysis (MNA)

MNA is based on shell bending theory applied to the perfect structure with an elastic-plastic material law and assumptions of small deflections. The result from this analysis is the plastic reference resistance, R_{pl}. Here, the effect of changes in the geometry is not considered.

Geometrically and materially nonlinear analysis (GMNA)

GMNA is a combination of GNA and MNA. It is an analysis based on shell bending theory applied to the perfect structure with an elastic-plastic material law and uses nonlinear large deflection theory. The result from this analysis is the resistance of the perfect structure.

Geometrically nonlinear elastic analysis with imperfections (GNIA)

Imperfections are explicitly included in GNIA. The analysis is based on shell bending theory applied to the imperfect structure, with assumptions of nonlinear large deflection theory. The material is treated as linear elastic, meaning that this analysis is only valid for shells that remain elastic. The analysis can be used to evaluate the internal forces, stresses or stress resultants in the imperfect structure due to the geometric nonlinearity.

Geometrically and materially nonlinear analysis with imperfections (GMNIA)

GMNIA is a combination of GMNA and GNIA. In GMNIA, imperfections are explicitly included. The analysis is based on shell bending theory applied to the imperfect structure, with assumptions of nonlinear large deflection theory with a nonlinear elastic-plastic material law. This analysis is difficult and time-consuming, as many different imperfection forms must be assessed. The result from this analysis corresponds to the characteristic buckling resistance R_k.

An overview of the different types of analysis is given in Table 2.1.

Table 2.1: Analysis types

Type of analysis	Deformations	Material law	Shell geometry	Buckling
LA	linear	linear	perfect	–
LBA	linear	linear	perfect	+
GNA	nonlinear	linear	perfect	+
MNA	linear	nonlinear	perfect	–
GMNA	nonlinear	nonlinear	perfect	+
GNIA	nonlinear	linear	imperfect	+
GMNIA	nonlinear	nonlinear	imperfect	+

An example of the expected results from the different numerical analyses is visualised in Figure 2.24. It should be noted that the load shown on the y-axis can be any load that causes deformation, such as axial compression due to an axial load or rotation due to a bending moment. The equilibrium path of the analyses containing buckling, shown in Figure 2.24, can be associated with the load-deflection curves shown in Figures 2.11 and 2.12.

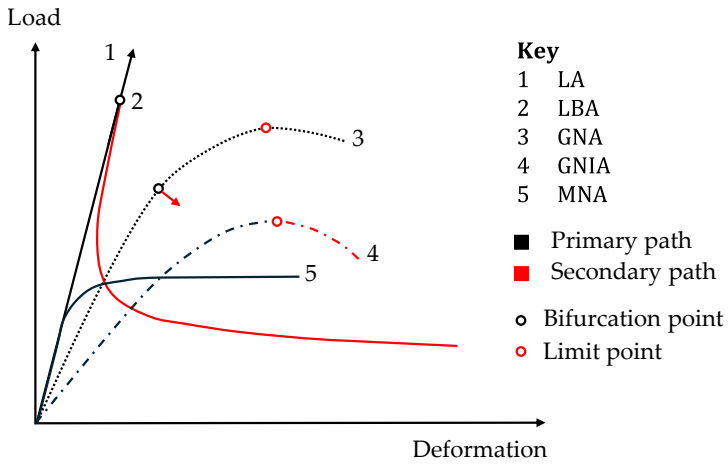

Figure 2.24: Load-deformation curves of different analysis types [12, ed.]

Starting with the curve representing an LBA, it is split into two parts: the primary and secondary path. The two parts are separated at the bifurcation point. The first part corresponds to an LA, which continues infinitely. However, an LBA sets a limit for this, which corresponds to the bifurcation point. In this example, the secondary

path for LBA has a negative stiffness, indicating an unstable behaviour. This closely resembles Figure 2.11 c) where the post-buckling response is unstable with negative stiffness. In Figure 2.11 c), the primary path is vertical because the figure is based on an axial load, and only deflection is shown on the horizontal axis.

The curve representing a GNA is nonlinear due to geometric nonlinearity. As previously mentioned, this type of analysis can be used to identify both a reduced bifurcation load or a possible limit load. If a bifurcation point is found, the secondary path branches off from the primary equilibrium path at the bifurcation point, as indicated by the arrow. In this example, the downward arrow indicates unstable behaviour as the stiffness becomes negative. Referring to the bifurcation buckling types in Figure 2.11, the post-buckling behaviour in this GNA can correspond to all types that exhibit unstable behaviour, namely Figure 2.11 c), d) and e). As for the deflection-amplification-type buckling, it can correspond to Figure 2.12 d).

The equilibrium path for GNIA is very similar to that of GNA. However, the difference is that deflection-amplification occurs due to imperfections. There is only one equilibrium path, as the configuration of the pre- and post-buckling deformations is the same. Similarly as before, the stiffness becomes negative post-buckling due to unstable behaviour corresponding to Figure 2.12 a), c) and d). In these examples, a negative post-buckling stiffness is shown in the different buckling analysis types, as shell buckling is often characterised as unstable.

Lastly, the MNA follows the LA at small deformations, but becomes nonlinear at larger deformations. What characterises the MNA is that it reaches a plateau at a value corresponding to the plastic reference resistance. It should be noted that neither an MNA nor an LA is a buckling analysis.

2.4.2 Buckling-relevant Geometric Tolerances and Imperfections

As revealed in section 2.2.2, imperfections can have a significant impact on the buckling resistance, especially in case of unstable post-buckling behaviour. According to EN 1993-1-6, imperfections should be included in the design of steel shells both in form of geometric imperfections, i.e. deviations from the nominal geometry, and of material imperfections, i.e. inhomogeneities, anisotropies and residual stresses. In this thesis, only geometric imperfections are considered.

Geometric tolerances define the limits to deviations in the constructed shell from the nominal geometry. These tolerances could theoretically easily be translated into geometric imperfections used in design calculations. However, as ECCS No. 125 [15] also points out, the fact that numerous forms of deviations can be encountered in real structures and that they can occur in various combinations, makes the choice of imperfections in design calculations very far from straightforward. Therefore, it was chosen in EN 1993-1-6 from the first edition to standardise the allowable form and magnitude of geometric tolerances, and based on them give guidance on the selection of unfavourable equivalent geometric imperfections.

Tolerance requirements are defined in terms of fabrication tolerance quality classes. Three standard classes are used in EN 1993-1-6 and in the corresponding execution standard EN 1090-2, namely, Class A (excellent), Class B (high) and Class C (normal).

Manufacturing tolerances

prEN 1993-1-6 [19] defines manufacturing tolerances of four types as described below and illustrated in Figures 2.25 to 2.28. According to ECCS No. 125 [15], other types of deviations can also affect the buckling strength of shells. However, the current state of knowledge limits the extent to which other tolerances can be accounted for.

- Out-of-roundness: deviation from circularity, see Figure 2.25
- Unintended eccentricity: deviation from a continuous middle surface normal to the shell at plate joints, see Figure 2.26
- Dimple and weld depression: local deviations from the nominal middle surface normal to the shell, see Figures 2.27 and 2.28
- Interface flatness: deviations of the shell base from full contact with the support

The importance of each tolerance type depends on the stress state of the shell. In case of axial compression, usually all four types are necessary to consider. Regarding dimple and weld depression, it should be noted that they are essentially similar as seen in Figures 2.27 and 2.28. However, in case of weld depression, an additional tolerance requirement is defined in terms of a different gauge length as shown in Figure 2.28 b).

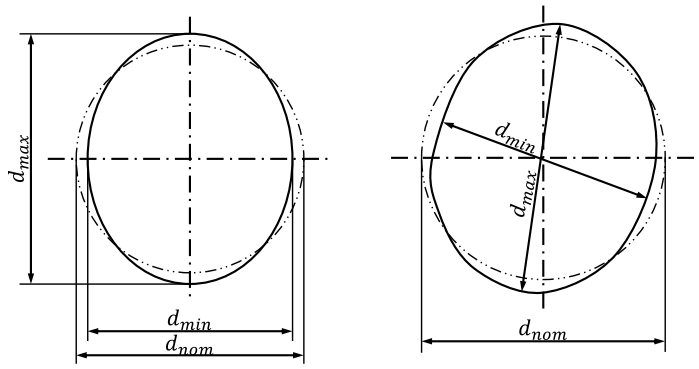

a) Flattening / elliptical b) Indeterminate / unsymmetrical

Figure 2.25: Manufacturing tolerance – Out-of-roundness [19, ed.]

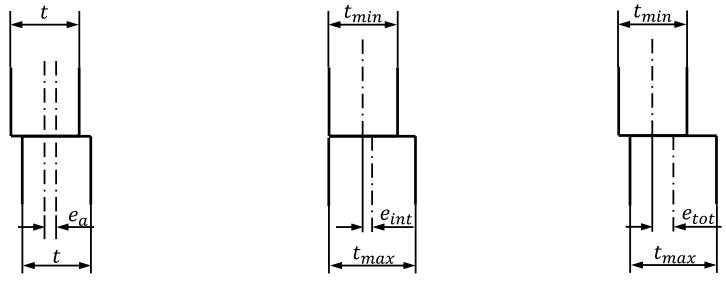

a) Unintended eccentricity, no change of plate thickness

b) Intended offset at change of plate thickness

c) Total eccentricity at change of plate thickness

Figure 2.26: Manufacturing tolerance – Unintended eccentricity [19, ed.]

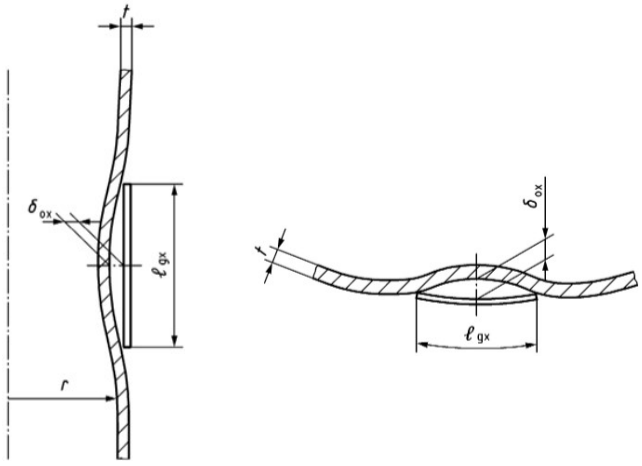

a) Measurement on the meridian

b) Measurement on the circumference

Figure 2.27: Manufacturing tolerance – Dimple [19, ed.]

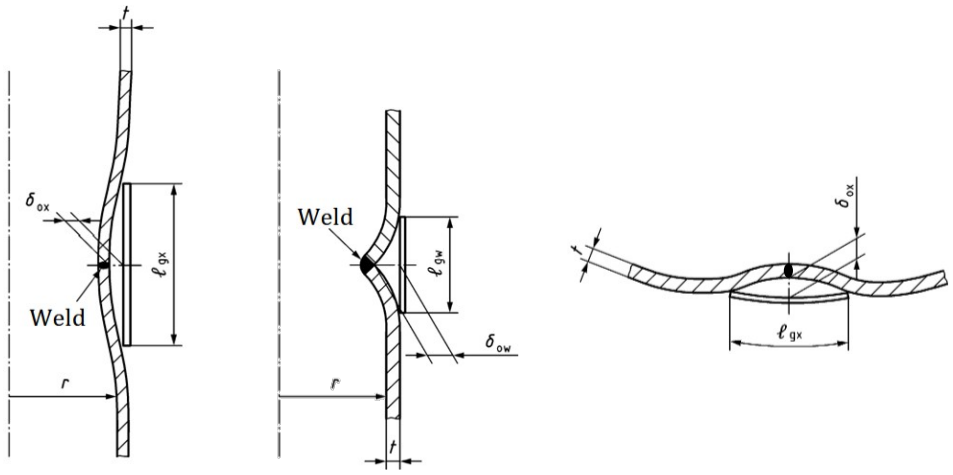

a) First measurement on the meridian

b) Second measurement on the meridian

c) Measurement on the circumference

Figure 2.28: Manufacturing tolerance – Weld depression [19, ed.]

Imperfections in design

Based on the standardised manufacturing tolerances, EN 1993-1-6 implicitly defines the form and magnitude of an equivalent geometric imperfection used in analytical calculation methods, as well as gives guidance on how an unfavourable imperfection can be selected to be used in a fully numerical design approach. Both analytical calculation methods in the standard are based on a dimple-like imperfection covering the whole circumference of the shell, typically referred to as a full-circumferential weld depression. It is also the form of imperfection that is recommended in GMNIA design unless other forms are susceptible to having a more unfavourable effect on the buckling resistance. This is expressed through the following note taken directly from prEN 1993-1-6 [15]:

> *"Only dimple imperfections are considered in the above requirements. Since a shell can have other imperfection forms in addition to the modelled dimples, this procedure is potentially unsafe. However, these calculations are based on a full circumference of an axisymmetric dimple (the worst case) which can rarely occur in practice, the full tolerance amplitude is rarely attained, and the potential for a practical load case to induce the resistance stress at the critical locations is small. For these reasons, the omission of an additional margin to allow for other imperfections is generally not serious."*

Traditionally, other forms of imperfections have been used in numerical calculations. The most frequent, probably still today, is an eigenmode-affine pattern, where a selected eigenmode is scaled and used as the imperfect geometry. However, prEN 1993-1-6 cautions the user that this might be far from the most unfavourable pattern.

2.4.3 Analytical Approach

To ensure sufficient strength and stability of steel shells, EN 1993-1-6 can be followed, which covers different limit states, such as plastic failure, cyclic plasticity, buckling and fatigue. Since this project focuses on buckling, the other failure types are not elaborated on further. The methods described in EN 1993-1-6 for determining the buckling strength apply to different loading conditions and geometries. Regarding loading conditions, the buckling strength can be determined for axial compression, global bending, circumferential compression or shear. The methods can also be applied to different geometries, such as cylinders or truncated cones. In this thesis, attention is directed towards the methods that describe cylindrical shells subjected to axial compression and global bending as presented in Annex D and Annex E, respectively.

The buckling strength of an axially compressed cylindrical shell can be determined using a stress-based design method given in EN 1993-1-6:2007 Annex D [12]. In EN 1993-1-6/A1:2017 [23], this method is refined and a resistance-based method for cylinders in uniform global bending is added in Annex E. Both methods are further refined in prEN 1993-1-6:2023 [19]. These approaches are described below, with further details in appendix A of this report.

The analytical process depicted in Figure 2.29 applies to both methods, Annexes D and E. The main purpose of this process is to determine key parameters that define the capacity curve, shown in Figure 2.30. The process and key parameters are described below, where terms that appear in Figure 2.29 are highlighted in bold within the text.

The process begins with the determination of the **plastic reference resistance** R_{pl} and the **linear elastic critical resistance** R_{cr}, which are then used to determine the **relative slenderness** $\overline{\lambda}$ as given in (2.10).

$$\overline{\lambda} = \sqrt{\frac{\kappa R_{pl}}{R_{cr}}} \tag{2.10}$$

A reduction factor κ is added to account for the influence of geometric imperfections on the plastic reference resistance R_{pl}, which is mostly relevant for cylindrical shells subjected to bending.

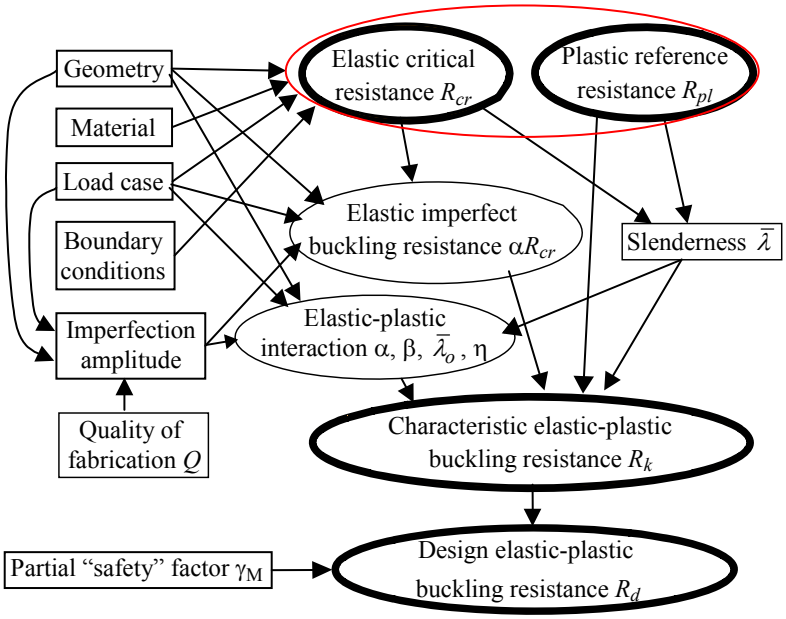

Figure 2.29: Analytical calculation process of EN 1993-1-6 [27, ed.]

Depending on their relative slenderness, structures experience one of the three types of buckling: elastic, elastic-plastic and plastic. The buckling reduction factor χ is calculated differently for each buckling type, as shown in (2.11)–(2.13). This reduction factor helps establish the characteristic buckling resistance R_k.

$$\chi = \frac{\alpha}{\overline{\lambda}^2} \qquad \text{for elastic region } \overline{\lambda}_p \leq \overline{\lambda} \tag{2.11}$$

$$\chi = 1 - \beta \left(\frac{\overline{\lambda} - \overline{\lambda}_0}{\overline{\lambda}_p - \overline{\lambda}_0} \right)^{\eta} \qquad \text{for elastic-plastic region } \overline{\lambda}_0 < \overline{\lambda} < \overline{\lambda}_p \tag{2.12}$$

$$\chi = \chi_h - \frac{\overline{\lambda}}{\overline{\lambda}_0}(\chi_h - 1) \qquad \text{for plastic region } \overline{\lambda} \leq \overline{\lambda}_0 \tag{2.13}$$

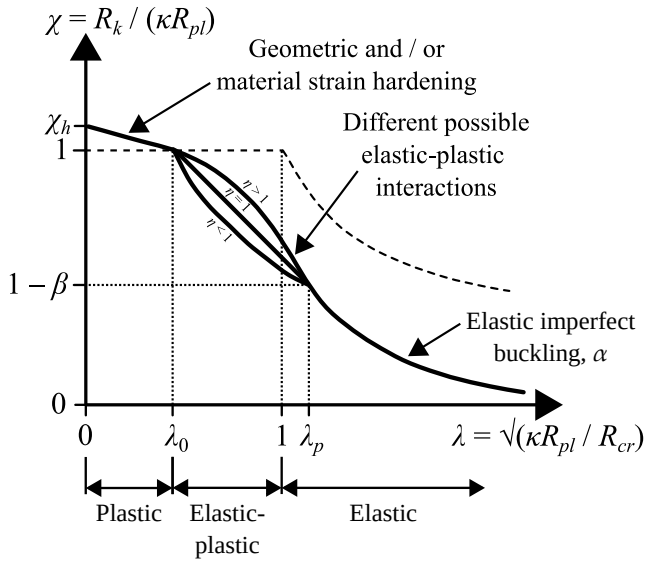

Figure 2.30: Capacity curve [25, ed.]

Very thin shells buckle in the elastic region, where equation (2.11) is valid, which is an inverse square function. This function determines the **elastic imperfect buckling resistance** governed by the elastic buckling reduction factor α. This factor consists of two contributions as shown in (2.14), α_G accounting for geometric nonlinearities and α_I for geometric imperfections. α_G and α_I are determined differently depending on the applied method. Common for both methods is that α_I depends on the **imperfection amplitude** δ_0. The reader is referred to appendix A for the specific expressions.

$$\alpha = \alpha_G \alpha_I \tag{2.14}$$

The imperfection amplitude δ_0 depends on the **quality of fabrication**, **geometry** and **load case**. The fabrication quality parameter Q depends on the specified fabrication tolerance quality class. The expression for δ_0 given in (2.15) is valid for cylindrical shells subjected to uniform axial compression or uniform global bending.

$$\frac{\delta_0}{t} = \frac{1}{Q}\sqrt{\frac{r}{t}} \tag{2.15}$$

Equation (2.13) applies to the plastic region where strain hardening occurs as thicker shells experience increased strength, which allows local stresses to surpass the yield strength before buckling occurs. The upper limit of the buckling reduction factor in the plastic region, denoted by χ_h, is called the hardening limit and is marked on the capacity curve in Figure 2.30.

Equation (2.12) is a form of interpolation between the elastic and plastic regions. Referring to Figure 2.29, the geometry, load case, imperfection amplitude and relative slenderness dictate the form of the **elastic-plastic interaction** which can be established by using certain physical capacity parameters: the elastic buckling reduction factor α, the plastic range factor β, the squash limit relative slenderness $\overline{\lambda}_0$ and the interaction exponent η.

As seen in Figure 2.30, the appearance of the curve in the elastic-plastic region is strongly dependent on the value of η, which can be determined using equation (2.16). The expression is a form of interpolation between the boundary values η_0 and η_p.

$$\eta = \frac{\overline{\lambda}(\eta_p - \eta_0) + \overline{\lambda}_p \eta_0 - \overline{\lambda}_0 \eta_p}{\overline{\lambda}_p - \overline{\lambda}_0} \tag{2.16}$$

The plastic range factor β is determined differently based on the chosen method, and reference is once again made to appendix A for further details. It should be noted that in prEN 1993-1-6, the plastic range factor depends on the imperfection amplitude, among others. The plastic limit relative slenderness $\overline{\lambda}_p$ controlled by β, see (2.17), dictates the transition between the elastic-plastic and elastic region.

$$\overline{\lambda}_p = \sqrt{\frac{\alpha}{1-\beta}} \tag{2.17}$$

The transition between the plastic and elastic-plastic buckling region is set by the squash limit relative slenderness $\overline{\lambda}_0$. In the current version of EN 1993-1-6, $\overline{\lambda}_0$ is a fixed value, while in prEN 1993-1-6 Annex E, an expression is introduced, which

depends on the imperfection amplitude, among others. However, the value of $\overline{\lambda}_0$ is still within a certain range, as shown in Figure 2.31.

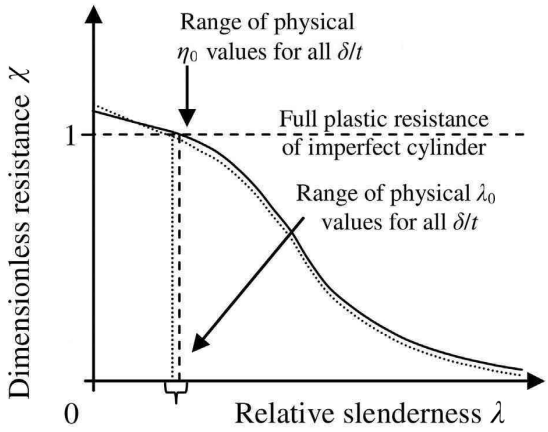

Figure 2.31: Capacity curve [28, ed.]

All of these described parameters are used to obtain the **characteristic elastic-plastic buckling resistance** R_k, which can be expressed through the buckling reduction factor χ, as shown in (2.18).

$$R_k = \chi \kappa R_{pl} \tag{2.18}$$

Lastly, a **partial safety factor** can be applied to obtain the **design buckling resistance** R_d. [15]

Assumptions behind analytical methods

The analytical methods in Annex D and E are derived based on certain assumptions that are more or less implicitly embedded in the expressions. These assumptions primarily concern three aspects:

- Support conditions
- Geometric imperfections
- Cross-sectional force distributions

The methods are derived based on a static system consisting of either pinned or fixed supports at each end. The geometric imperfection is a full-circumferential weld depression as mentioned in section 2.4.2. This type of imperfection is the most critical in terms of buckling resistance, yet it rarely occurs. When the execution standard EN 1090 is followed, this type of imperfection must be avoided. Concerning cross-sectional forces, Annex D applies to shells under uniform stress distributions, e.g. axial compression, and the method in Annex E applies to shells under uniform global bending.

It should be noted that the range of validity of the methods in EN 1993-1-6 is limited to radius-to-thickness ratios between 50 and 2000. Furthermore, a note in the standard states that Annex D is rather conservative for certain relatively thick-walled cylinders, i.e. with low r/t ratios.

Comparison and assessment of analytical methods

This section aims to compare and assess three analytical methods in EN 1993-1-6 using the study of Sadowski and Filippidis [25]. The three methods are:

- Stress-based method in EN 1993-1-6:2007 Annex D
- Stress-based method in EN 1993-1-6:2025 Annex D
- Resistance-based method in EN 1993-1-6:2025 Annex E

The method in Annex E, which applies to shells under uniform global bending, was introduced recently. Prior to that, Annex D was used, even though it was not necessarily suitable for the actual stress distribution. The reason was that no other shell system could be imagined to be more imperfection-sensitive than a cylinder under uniform axial compression. Using the method in Annex D, it is possible to consider both normal stresses from axial compression and normal stresses due to bending. However, the method was derived based on a cylindrical shell subjected to only uniform normal stresses. By using the method in Annex E, it is also possible to include both influences, although it becomes rather conservative.

Annex D: 2007 vs 2025
First, a comparison of the capacity curves for the method in Annex D from the current version of EN 1993-1-6:2007 and the soon-to-be-published EN 1993-1-6:2025 is presented. As mentioned before, EN 1993-1-6 operates with three fabrication tolerance quality classes (FTQCs), represented by the letters A, B and C. Since the capacity curves depend on FTQC, three different curves are shown for each version of Annex D in Figure 2.32. To ensure a common basis for the comparison, the capacity curve based on the German standard DIN 18800-4 is also included, representing an approximate lower bound to about 750 laboratory test results accumulated before 1990.

In EN 1993-1-6:2007, the capacity curve is established using a rather simple approach, where several of the capacity parameters are constant. This concerns the plastic limit range β, the interaction exponent η and the squash limit relative slenderness $\overline{\lambda}_0$. The elastic buckling reduction factor α is the only capacity parameter with an expression and has an explicit empirical dependency on the imperfection amplitude δ_0. According to Sadowski and Filippidis [25], it appears the capacity parameters in EN 1993-1-6:2007 for FTQC B were calibrated against roughly the same empirical test data as DIN 18800-4, which explains why the curves are closely aligned in Figure 2.32.

In EN 1993-1-6:2025, all parameters are refined compared to the version from 2007. β and η are no longer constant and both depend on the imperfection amplitude δ_0, among others. The value of $\overline{\lambda}_0$, where $\chi = 1$, is reduced, which makes the plastic region narrower, as seen by comparing the two graphs in Figure 2.32. Moreover, the separation of the elastic buckling reduction factor $\alpha = \alpha_G \alpha_I$ and the benefit of strain hardening in the plastic range are introduced. The expressions for the capacity parameters are now determined solely based on computational parametric simulations. This means that the results from the experimental dataset are no longer directly tied to the parameters, since they are no longer considered representative, as explained in section 2.3.

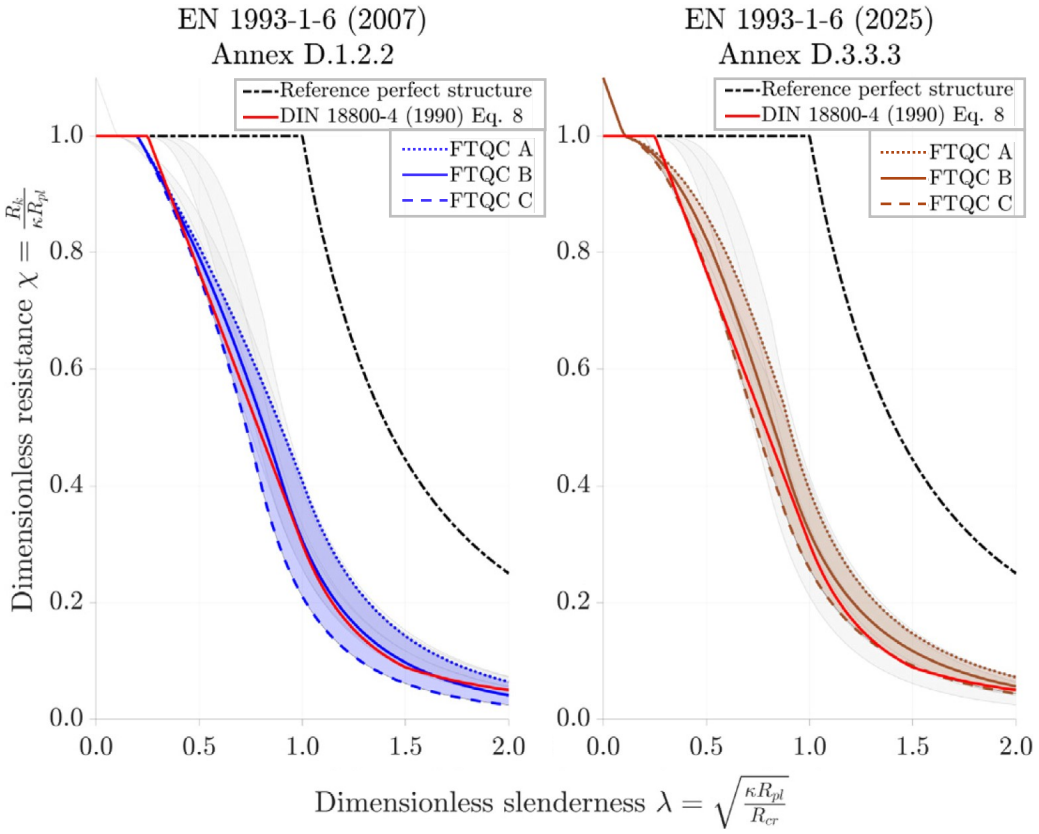

Figure 2.32: Comparison of capacity curves based on Annex D from 2007 and 2025 [25, ed.]

The significant visual difference between the capacity curves from 2007 and 2025 is that a large part of the curves has shifted upward. While in the method from 2007, the curve for FTQC B was calibrated against the previously mentioned test data, the various capacity parameters from 2025 have been adjusted so that the test data now aligns better with FTQC C. This makes the method from 2025 less conservative.

Annex D 2025 vs Annex E 2025

Annex E contains a newer design method based on reference resistances and determines the capacity curve for a cylindrical shell under uniform global bending, in contrast to the stress-based design method in Annex D, which assumes uniform axial compression in the shell wall. A large part of the framework in Annex E is the same in Annex D, i.e. the same capacity parameters are present in both methods except for κ, accounting for the effect of imperfections on the plastic moment M_{pl}. In the following, the significant differences in determining the parameters for the two methods are described. The capacity curves from the two methods are shown in Figure 2.33.

A significant difference between the two methods is that in Annex E, a length function f_Ω is introduced and included in the expressions for the plastic limit range β and the squash limit relative slenderness $\overline{\lambda}_0$. Psychically, it means that the length of the cylinder gets a slightly larger contribution in determining the buckling resistance. Furthermore, the geometric nonlinear buckling reduction factor α_G is no longer a constant value but an expression that captures the influence of cross-sectional ovalisation, which can occur pre-buckling for a cylinder subjected to uniform bending.

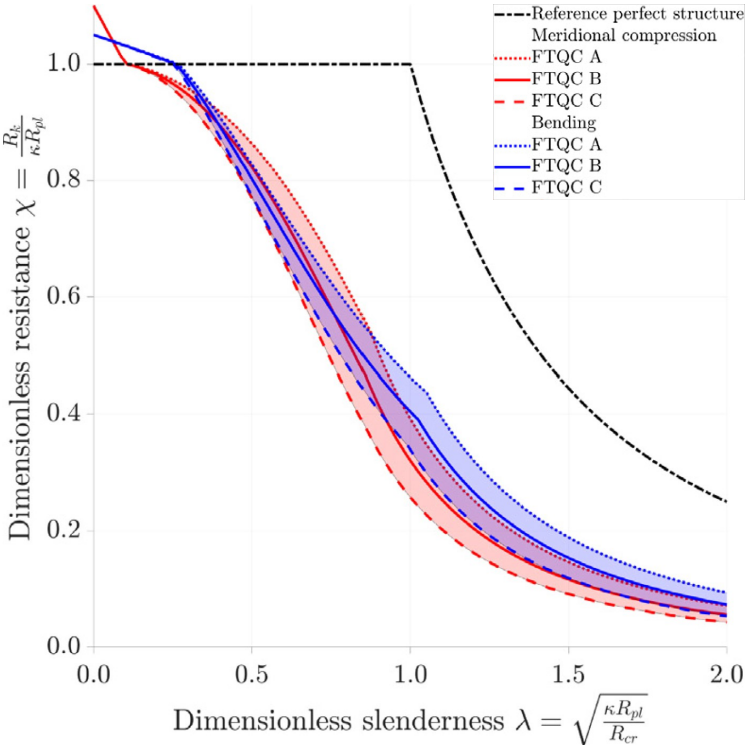

Figure 2.33: Comparison of capacity curves based on Annex D and E [25, ed.]

By considering the curves for the two methods in Figure 2.33, three primary differences can be observed. In the elastic region, the capacity curve for uniform axial compression is conservative compared to uniform bending. The plastic region is wider for the method with uniform bending, as the squash limit relative slenderness tends to be higher. Lastly, in the elastic-plastic region, the method in Annex E is generally more conservative, and it is therefore recommended to be used for cylinders with intermediate slenderness, $\overline{\lambda}_0 < \overline{\lambda} < \overline{\lambda}_p$.

2.4.4 Partially and Fully Numerical Approach

Besides the analytical approach, EN 1993-1-6 provides two other approaches to determine the buckling resistance of shells, as mentioned at the beginning. One is a partially numerical approach (LBA-MNA), where some part of the analytical calculations are replaced by results from numerical analyses for more precise assessment.

By performing global linear analyses using the LBA-MNA procedure, some parts of the analytical calculation are replaced by numerical results. A bifurcation analysis (LBA) is conducted to determine the lowest eigenvalue, which represents the elastic critical resistance R_{cr}. The plastic reference resistance R_{pl} is determined using a plastic collapse analysis (MNA). These resistances are used as input when determining the relative slenderness in the subsequent analytical calculation.

It is also possible to perform a fully nonlinear global analysis, including geometric imperfections (GMNIA). Here, the imperfections and material nonlinearity have to be included explicitly in the model. The analysis has to take full account of geometry changes due to the loads. The result from this analysis is the characteristic elastic-plastic buckling resistance R_k. [15]

This page is intentionally left blank.

3 Scope

3.1 Problem Statement

As stated in the introduction, the current analytical buckling verification methods in EN 1993-1-6 are potentially conservative when used to design monopiles for offshore wind turbines. A preliminary investigation of that conservatism and its possible reasons can be conducted by examining the differences between the assumptions behind the calculation methods and the corresponding conditions in monopiles. Based on sections 2.1 and 2.4, the differences are summarised in Table 3.1.

Table 3.1: Differences causing potential conservatism

	Assumptions in EN 1993-1-6	**Conditions in monopiles**
r/t ratio	Range of validity: 50 – 2 000	35 – 65
Static system	Supported at both ends	Cantilever
Internal forces	Uniform moment OR Axial compression	Increasing moment AND Axial compression
Imperfections	Full-circumferential dimple	Dimple of limited size

As seen in the table, the geometry of monopiles can fall outside the range where the calculation methods are valid. It should be mentioned at this point that there is a note in EN 1993-1-6 stating that the stress-based design method in Annex D can be rather conservative for some relatively thick-walled shells. Furthermore, as discussed in section 2.4.3, the resistance-based design rules in Annex E are more conservative for most shells experiencing elastic-plastic buckling, i.e. relatively thick-walled shells. That makes the method even more conservative than the one in Annex D in those cases and might explain the conservatism suspected by the wind industry, as monopiles are considered moderately thick-walled due to their low r/t ratios. The difference in static systems in terms of global boundary conditions probably only has a minor effect on local shell buckling; nevertheless, it ought to be investigated. Internal force distributions that differ from the ones assumed in the calculation methods are currently not possible to consider analytically without introducing an additional layer of conservatism. And lastly, the fact that the methods assume a full-circumferential dimple as the form of imperfection, even though that is not permissible according to the rules about geometric tolerances, can also give the impression of conservatism. In light of the foregoing, the present project aims to address the issue by seeking answer to the following question:

> How well do the analytical methods in EN 1993-1-6 fit to a typical monopile, and how can the expressions for the capacity curve parameters be optimised with respect to geometry, boundary conditions and geometric imperfections observed in monopiles?

3.2 Research Strategy

The purpose of this section is to describe how the objective of the project is planned to be achieved using specific methods and models. The objective is primarily pursued using a series of finite element analyses. The ideal situation would be to compare the analytical results with experimental ones. Unfortunately, the existing experiments on steel cylindrical shells subjected to uniform axial compression are insufficient, as a large scatter is observed in the test results and important information about the specimens was not recorded to explain its reason properly [25]. However, with carefully built advanced numerical models, it is possible to achieve results that closely reflect reality.

3.2.1 Choice of Models

A series of numerical calculations is performed using three sets of different models, as described below and summarised in Table 3.2. All three sets are based on the same geometries and static system but differ in terms of internal force distributions and geometric imperfections, following Table 3.1. Note that the investigation of increasing bending moment distributions in the project is limited to analyses without imperfections.

Table 3.2: Sets of numerical models in the project

Model set	Static system	Internal forces	Imperfection form
Set 1	Cantilever	Uniform bending	Full-circumferential dimple
Set 2	Cantilever	Increasing bending	None
Set 3	Cantilever	Uniform bending	Dimple of limited size

Geometries

Various geometries are used for the models in order to map a significant portion of the capacity curve. Even though typical monopiles are mostly located in the upper part of the elastic-plastic region, it is necessary to map parts of both the elastic and the plastic regions, so that the borders and the curve itself can be established as accurately as possible. Therefore, it is decided to investigate cylindrical shells with 39 different r/t ratios: from 8 to 12 with an increment of 1, from 15 to 75 with an increment of 5, from 100 to 350 with an increment of 25 and from 355 to 400 with an increment of 5. Finer increments are chosen around the borders and within the range typical for monopiles.

$$r/t = \{8, 9, ..., 12, 15, 20, ..., 75, 100, ..., 350, 355, ..., 400\}$$

Assuming that the results are independent of the absolute value of radius and thickness, the radius is chosen as a fixed value of 4.0 m, typical for monopiles. Note that this is the radius of the cylinder's middle surface, and whenever radius is mentioned in the present thesis, it refers to the radius of the cylinder's middle surface unless explicitly stated otherwise.

$$r = 4.0 \text{ m}$$

The effect of length is investigated using models with different lengths that can occur for monopiles. These are chosen based on section 2.1 as the interval from 10 m to 60 m with an increment of 5 m.

$$L = \{10, 15, ..., 60\} \text{ m}$$

The chosen geometries result in first relative lengths ω between 7 and 300, and second relative lengths Ω between 0.12 and 5.30, corresponding to medium-length and long (formally transitional-length) cylinders.

$$7 \leq \omega \leq 300 \qquad \text{and} \qquad 0.12 \leq \Omega \leq 5.30$$

Static system

All three sets of numerical models are established with global boundary conditions corresponding to a cantilever beam-column. Even though the support of a monopile at the seabed has finite stiffness in reality, as a simplification, it is modelled as infinitely stiff in the project. Local boundary conditions, i.e. rigid links, are applied as described in the next chapter. Additionally, a few similar models with fixed ends are used for model validation, which is also discussed in the next chapter.

Internal forces

The actual distribution of internal forces in monopiles is complex due to the various, mainly environmental loads acting on them, as briefly described in section 2.1. Different internal forces are present in monopiles, however, the one that presumably governs their resistance is the bending moment. Besides the moment directly transferred from the transition piece to the monopile, the shear force at the connection and the distributed load on the monopile itself also generate bending. As a simplification in the project, only the effect of the shear force and bending moment on top of the monopile is considered, leading to the internal force distributions illustrated in Figure 3.1.

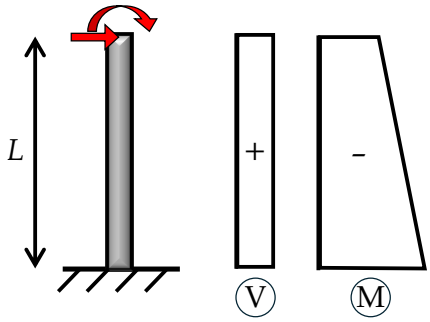

Figure 3.1: Simplified static system and internal forces in monopiles

In two of the three sets of models, a uniformly distributed bending moment is applied to the cylinders, conforming to EN 1993-1-6. The effect of a more realistic internal force distribution is investigated in set 2 with a linearly increasing bending moment. Other internal forces are considered of secondary importance in terms of buckling in typical monopiles and are therefore outside the scope of the project.

Imperfections

A full-circumferential dimple in accordance with EN 1993-1-6 is included in the first set of models, and the effect of a more frequently occurring and permissible imperfection form, namely a dimple of limited size, is investigated using the third set. The limited dimple is selected, since it is presumed to be the most deleterious to buckling amongst the three forms of imperfections manufacturing tolerances are prescribed for in EN 1993-1-6, especially if placed at a critical position in relation to the structure's buckling mode. This presumption is supported by a recent master's thesis [29] and a report cited in the thesis.

The size of imperfections in the models is chosen based on the three standard fabrication tolerance quality classes, A, B and C, corresponding to fabrication tolerance quality parameters $Q = \{40, 25, 16\}$.

3.2.2 Choice of Methods

In the following, a specific analytical method from EN 1993-1-6 is selected. Three methods were presented and compared in section 2.4.3. These are also illustrated in the flow chart in Figure 3.2. The method provided in Annex D in EN 1993-1-6:2007 is excluded, as it has already been optimised in prEN 1993-1-6:2023. The two methods in prEN 1993-1-6:2023 are based on two different loading conditions, namely uniform axial compression in Annex D and uniform global bending in Annex E. As discussed previously, a monopile is subjected to both an axial load and a bending moment. However, the bending moment is more significant compared to the axial load, and it is therefore more accurate to perceive a monopile as a member in bending. Furthermore, according to Sadowski and Filippidis [25], the capacity curve determined using Annex E is more conservative compared to Annex D in the elastic-plastic region, which corresponds to the conditions encountered in the typical monopiles. Based on the above, the method in prEN 1993-1-6:2023 Annex E is selected for further assessment and potential reformulation of expressions in the calculation process.

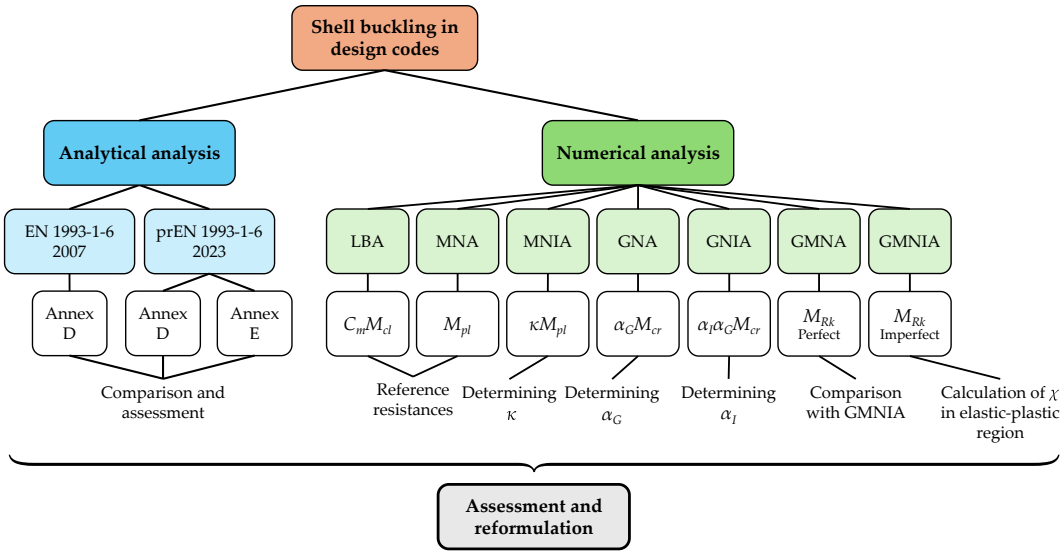

Figure 3.2: Choice of methods — overview

Various types of numerical analysis are used to achieve the project objective, each of which provides an important output that can be used for subsequent assessment. The output of each analysis is presented below, along with an explanation of the optimisation approach for the selected method.

Numerical analysis of the types shown in Figure 3.2 is conducted with different aims using the 3D FEA software Ansys Mechanical. LBA and MNA are used to determine the reference resistances M_{cr} and M_{pl}, respectively. The reduction factor κ for M_{pl} can be estimated using MNIA, an analysis similar to MNA, but accounting for imperfections within the model. GNA assists with determining the geometric reduction factor α_G. GNIA is performed with the aim of determining the elastic buckling reduction factor α, which contains both the imperfection reduction factor α_I and the geometric reduction factor α_G. GMNIA is conducted to determine the characteristic buckling resistance M_{Rk}, based on which the buckling reduction factor χ can be calculated. To evaluate the effect of imperfections on the buckling resistance, GMNA are performed, as the result from this analysis is the characteristic buckling resistance for a perfect structure. Each type of analysis contributes to mapping the capacity curve visualised in Figure 3.3. It should be noted that hardening in the plastic region is not considered in this project, which means that the maximum value of the buckling reduction factor is $\chi = 1$.

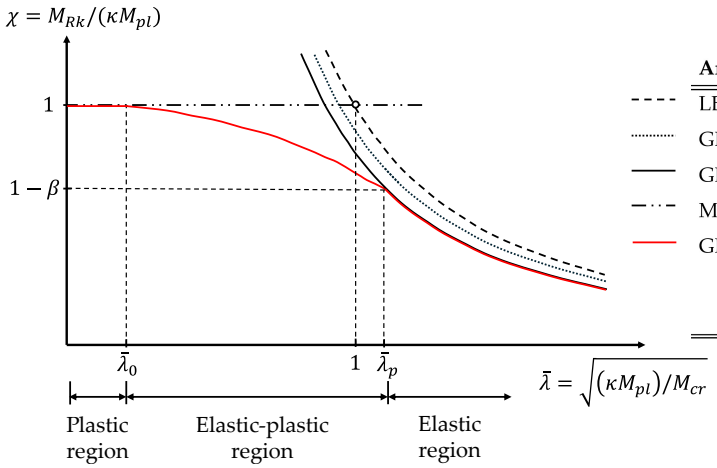

Analysis	χ	M_{Rk}
LBA	$1/\bar{\lambda}^2$	$M_{cr} = C_m M_{cl}$
GNA	$\alpha_G/\bar{\lambda}^2$	$\alpha_G M_{cr}$
GNIA	$\alpha_G \alpha_I/\bar{\lambda}^2$	$\alpha_G \alpha_I M_{cr}$
MNIA	1	κM_{pl}
GMNIA		
Elastic	$\alpha_G \alpha_I/\bar{\lambda}^2$	$\alpha_G \alpha_I M_{cr}$
Plastic	1	κM_{pl}

Figure 3.3: Capacity curve defined by the different numerical analyses

The area of interest in the capacity curve regarding monopiles is the elastic-plastic region. However, to assess and potentially optimise this region, it is necessary to consider the whole capacity curve, i.e. the elastic and plastic regions as well.

Elastic region

The parameters that can be considered in the elastic region are α_G, α_I, and C_m, where C_m is a factor that accounts for the end boundary conditions in a cylindrical shell, as described in section 2.3. In (3.1), expressions are given for determining these parameters through numerical analyses.

$$\begin{aligned}
&\text{LBA:} && M_{R,LBA} = M_{cr} = C_m M_{cl} && \Rightarrow && C_m = \frac{M_{R,LBA}}{M_{cl}} \\
&\text{GNA:} && M_{R,GNA} = \alpha_G M_{R,LBA} = \alpha_G M_{cr} && \Rightarrow && \alpha_G = \frac{M_{R,GNA}}{M_{cr}} \\
&\text{GNIA:} && M_{R,GNIA} = \alpha_I M_{R,GNA} = \alpha_I \alpha_G M_{cr} && \Rightarrow && \alpha_I = \frac{M_{R,GNIA}}{\alpha_G M_{cr}}
\end{aligned} \tag{3.1}$$

The elastic critical moment resistance M_{cr} is found in an LBA, as $M_{R,LBA} = M_{cr}$. Analytically, M_{cr} consists of two contributions: one is the classical elastic critical moment M_{cl} and the other is the factor C_m. The purpose of this analysis is to optimise the factor C_m.

The geometric reduction factor α_G is found as the ratio between the moment resistance of the model $M_{R,GNA}$ and the analytical elastic critical moment resistance M_{cr}. In general, previously obtained numerical results, such as M_{cr} from an LBA, are avoided in other analyses to ensure a consistent basis for all expressions.

The imperfection reduction factor α_I is determined using a GNIA as the ratio between the moment resistance of the model $M_{R,GNIA}$ and the analytical expressions for α_G and M_{cr}.

Plastic region

In regard to plasticity, the plastic moment resistance M_{pl} is determined using an MNA. No optimisation of the analytical expression for M_{pl} is planned to be performed, as it is already well established. Instead, a comparison is made between the analytical and numerical results. As for the reduction factor κ, it will be evaluated and potentially optimised. It can be found as the ratio between the plastic moment resistance of the imperfect structure $M_{R,MNIA}$ and M_{pl}, as shown in (3.2).

$$\begin{aligned}
&\text{MNA:} && M_{R,MNA} = M_{pl} \\
&\text{MNIA:} && M_{R,MNIA} = \kappa M_{pl} \Rightarrow \kappa = \frac{M_{R,MNIA}}{M_{pl}}
\end{aligned} \tag{3.2}$$

Elastic-plastic region and boundaries

The capacity curve in the elastic-plastic region is controlled by the interaction exponent η, which defines the appearance of the curve and can be calculated as shown in (3.3).

$$\eta = \eta_0 \frac{\overline{\lambda}_p - \overline{\lambda}}{\overline{\lambda}_p - \overline{\lambda}_0} + \eta_p \frac{\overline{\lambda} - \overline{\lambda}_0}{\overline{\lambda}_p - \overline{\lambda}_0} \tag{3.3}$$

This analytical expression is a form of interpolation between the values at the boundaries η_0 and η_p. These boundary values can be found in different ways. In this project, the methodology in [25] is followed, where η_0 and η_p are chosen such that the capacity curve is a lower bound to all GMNIA results in the elastic-plastic region.

The parameters that govern the boundaries between the plastic, elastic-plastic and elastic regions are the squash limit relative slenderness $\overline{\lambda}_0$, plastic limit relative slenderness $\overline{\lambda}_p$, and the plastic range factor β. Determining the mentioned parameters

is not straightforward, as there are no specific analysis types to identify them, in contrast to the other parameters in the elastic and plastic regions. Therefore, GMNIAs must be performed to define the capacity curve, as shown in Figure 3.3. Note that the results from GMNIAs consist of a series of points to which a curve is fitted.

β corresponds to the χ value where the curves for GNIA and GMNIA begin to deviate from each other. In other words, it is necessary to look for the maximum χ where GNIA and GMNIA are equal.

As for $\overline{\lambda}_0$, it corresponds to the point where $M_{R,MNIA}$ and $M_{R,GMNIA}$ deviate from each other, as shown in Figure 3.3. In other words, it is the maximum value of $\overline{\lambda}$ where the curves from MNIA and GMNIA are equal.

$\overline{\lambda}_p$ can be calculated analytically, as shown in (3.4), using the optimised expressions for α and β.

$$\overline{\lambda}_p = \sqrt{\frac{\alpha}{1-\beta}} \tag{3.4}$$

3.2.3 Research Plan

A plan for achieving the project objective is provided below, where the individual sets of models described in section 3.2.1 are connected to the types of numerical analysis and their overall goal, as discussed in section 3.2.2.

The main goal of set 1 is to assess how suitable the analytical method is for a cantilever beam and to reformulate the expressions for the different capacity curve parameters to optimise the fit. Consequently, all seven analysis types are employed with model set 1. The aim of set 2 is to propose a way to include the effect of a linear bending moment distribution in a part of the analytical method through a potential new factor. This investigation is initially limited in the project to analysis type LBA. The influence of a different, frequently occurring and permissible imperfection form is investigated using set 3, and thus only the four analysis types that include imperfections incorporate models from that set. Sets 2 and 3 are defined so that only one condition is changed in them compared to set 1; therefore, the moment distribution in set 3 is kept as uniform.

Based on the chosen collection of r/t ratios, lengths L and fabrication tolerance quality parameters Q, the number of simulations for each model set and analysis type is selected as shown in Table 3.3, resulting in 7 200 simulations in total. Note that since the plastic moment resistances are presumed to be independent of the length, only three different lengths are investigated in MNAs and MNIAs. Furthermore, since the existing expressions for M_{pl} and κ are supposedly accurate, the number of r/t ratios is also reduced for MNAs and MNIAs. The selected r/t ratios and lengths in these analysis types are as shown below.

$$r/t = \{8, 9, ..., 12, 15, 25, ..., 75, 100, 200, 300, 400\}$$

$$L = \{10, 30, 50\} \text{ m}$$

Table 3.3: Overview of research plan

Set	Analysis type	Number of r/t	Number of L	Number of Q	Total no. of simulations	Goal
1	LBA	39	11	–	429	Assess & rewrite C_m
	MNA	16	3	–	48	Assess M_{pl}
	MNIA	16	3	3	144	Assess & rewrite κ
	GNA	39	11	–	429	Assess & rewrite α_G
	GNIA	39	11	3	1 287	Assess & rewrite α_I
	GMNA	39	11	–	429	Comparison with GMNIA
	GMNIA	39	11	3	1 287	Assess & rewrite η, β and $\overline{\lambda}_0$
2	LBA	39	11	–	429	New factor for moment distribution
3	MNIA	16	3	3	144	Assess & rewrite κ
	GNIA	39	11	3	1 287	Assess & rewrite α_I
	GMNIA	39	11	3	1 287	Assess & rewrite η, β and $\overline{\lambda}_0$

4 Numerical Analysis

This chapter contains a detailed description of the numerical models used in the project, the input and output of the different analysis types, and the validation and verification, ensuring that the model and other input parameters are appropriate.

All numerical analyses in the project are performed using the finite element method and the general 3D FE software Ansys Mechanical 2024 [30, 31]. Both modelling and analysis are primarily executed in Mechanical APDL through scripting in Ansys Parametric Design Language (APDL), as well as in Python, utilising the PyMAPDL library [32]. A few analyses are also performed through the graphical user interface of Ansys Mechanical, and the results are compared with those from MAPDL to ensure the correctness of the scripts. The master script prepared as part of the project can be found in appendix B. Based on that, batch scripts are constructed for each analysis type and run in batch mode in UCloud [33], an interactive high-performance computing platform provided for the project by Aalborg University in collaboration with the University of Southern Denmark.

4.1 Finite Element Models

4.1.1 Geometry

The geometry of the FE models in the project consists of a simple cylindrical shell with three parametric dimensions: the radius r, the wall thickness t and the length L, as shown in Figure 4.1. The range of dimensions investigated in the project is described in section 3.2.1. The cylinder is placed in a 3D Cartesian coordinate system with its cross-section in the centre of the XY-plane and its length along the Z-axis between $Z = 0$ and $Z = L$.

Due to the axisymmetric nature of the cylinder and the fact that loading and boundary conditions in case of a cantilever in uniaxial bending are symmetrical across a single axial plane, a half-cylinder model can be adopted to reduce computational demands and increase efficiency. According to Teng and Song [34] and Rotter et al. [21], finite element models of half and quarter cylinders are generally acceptable, where loading and boundary conditions with either one or two symmetry planes exist and no torsional deformations are present, assuming that the required results are identical with those from a full-cylinder model. Thus, the majority of numerical calculations in the project are performed using half-cylinder models as shown in Figure 4.1, while initial analyses are carried out with full cylinders, ensuring that the two models yield the same fundamental outcome.

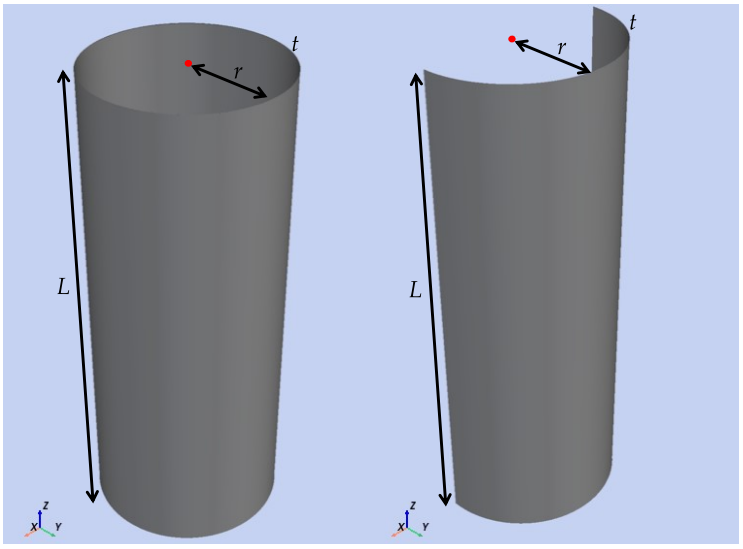

a) Full-cylinder model b) Half-cylinder model

Figure 4.1: Geometry of FE models

Imperfections

As discussed in section 3.2.1, two different imperfection forms are considered in the analysis: a full-circumferential dimple and a dimple of limited size. A single instance of either the one or the other is included in the models for the analysis types with geometric imperfections. To produce the most deleterious effect, both imperfections are placed at midspan, and the limited dimple is also placed in the middle of the compressed circumference. The two imperfection forms in a full-cylinder model are shown in Figure 4.2, where the size of the full-circumferential dimple corresponds to FTQC C with $Q = 16$ and the limited dimple to $Q = 4$ for better visibility.

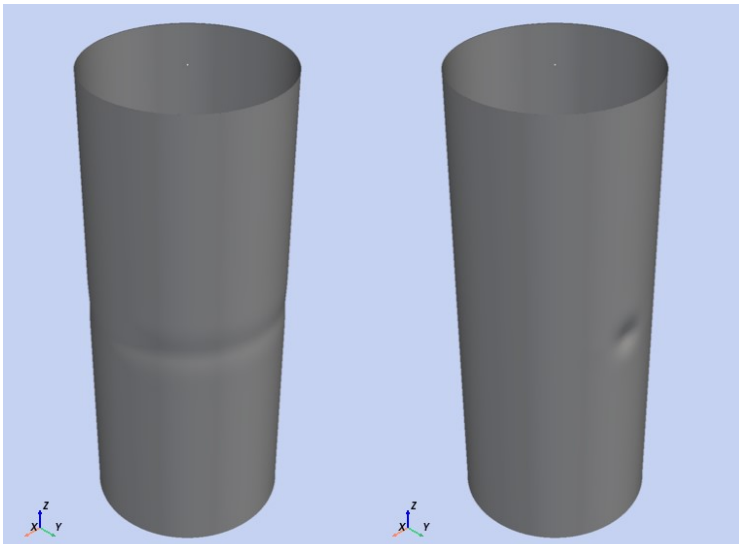

a) Cylinder with full circumferential dimple b) Cylinder with limited dimple

Figure 4.2: Imperfections in FE models

The Type A full-circumferential weld depression of Rotter and Teng [35] is adopted as the shape of the full-circumferential dimple. According to Wang et al. [28], it has been shown to be a realistic representation of a weld depression and has widely been applied over the last 35 years. Furthermore, the current analytical buckling verification methods in EN 1993-1-6 are also based on this imperfection shape [28]. A Type A weld depression at midspan, i.e. axial coordinate $Z = L/2$, can be defined algebraically as shown in (4.1) as per [28], where δ_0 is the algebraic imperfection amplitude and Λ is the linear meridional bending half-wavelength. Both parameters depend on the radius and the wall thickness, and δ_0 is also a function of the quality parameter Q. Λ is explained in more detail in section 4.1.4. The expression is visualised in Figure 4.3 for a cylinder with $L = 20$ m, $r = 4$ m, $t = 0.08$ m and 0.04 m, manufactured in normal fabrication tolerance quality class (FTQC C) with $Q = 16$.

$$\delta_Z(Z) = \delta_0 e^{-\frac{\pi}{\Lambda}\left|Z-\frac{L}{2}\right|}\left[\cos\left(\frac{\pi}{\Lambda}\left|Z-\frac{L}{2}\right|\right)+\sin\left(\frac{\pi}{\Lambda}\left|Z-\frac{L}{2}\right|\right)\right] \tag{4.1}$$

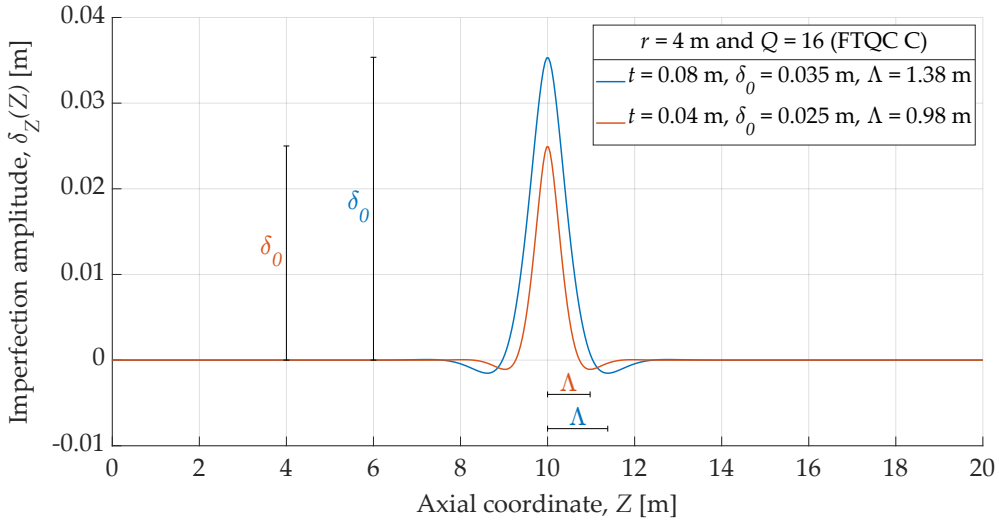

Figure 4.3: Visualisation of expression for full-circumferential weld depression

Rotter and Teng [35] proposed algebraic expressions for two types of weld depressions, Type A and Type B, which differ in the assumed rigidity of the weld and thereby the extent of the imperfection as illustrated in Figure 4.4. Type A idealises the weld as rotationally stiff, whereas Type B assumes it to be rotationally flexible. Geometric tolerances for weld depressions in EN 1993-1-6 correspond to these two fundamental types, as seen in Figure 4.5. Since both the imperfection depth and the measuring gauge length in the standard are the same for a rotationally stiff weld depression (first measurement) as for a dimple, the same algebraic expression can be used to describe the shape of the limited dimple along the meridian. Furthermore, since the length of the gauges used for meridional and circumferential measuring is equal, expression (4.1) can be adjusted and used to describe the shape of the limited dimple along the circumference. The adjusted expression is shown in (4.2), where θ is the angular coordinate in radians, and it is assumed that loading is defined so that the middle of the compressed circumference has an angular coordinate $\theta = 0$. In a

Cartesian coordinate system with the X-axis at $\theta = 0$, this requires a positive bending moment around the Y-axis.

$$\delta_\theta(\theta) = \delta_0 \mathrm{e}^{-\frac{\pi}{\Lambda}|r\theta|} \left[\cos\left(\frac{\pi}{\Lambda}|r\theta|\right) + \sin\left(\frac{\pi}{\Lambda}|r\theta|\right)\right] \tag{4.2}$$

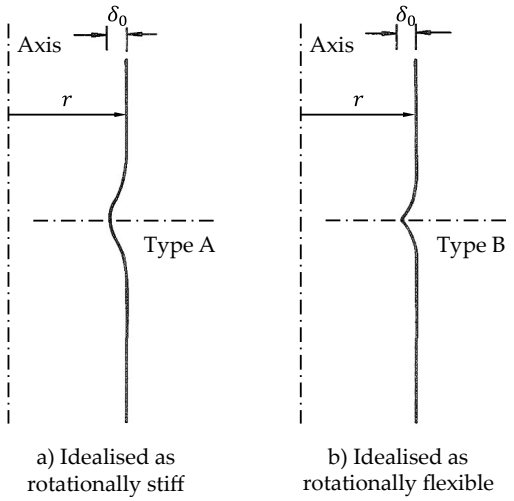

a) Idealised as rotationally stiff

b) Idealised as rotationally flexible

Figure 4.4: Two types of weld depression [35, ed.]

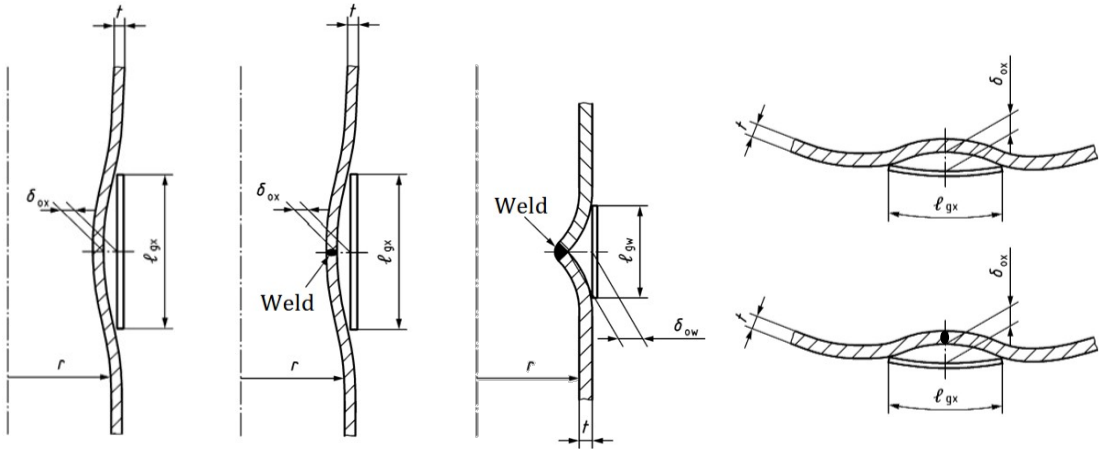

a) Dimple measurement

b) Weld depression first measurement

c) Weld depression second measurement

d) Measurements on the circumference

Figure 4.5: Manufacturing tolerances in EN 1993-1-6 [19, ed.]

Inspired by Yadav and Gerasimidis [36], the shape of the limited dimple complying with EN 1993-1-6 can be fully described as shown in (4.3) by combining expressions (4.1) and (4.2) defining the shape along the meridian and the circumference, respectively. Using the combined expression, it is possible to determine the radial coordinate of any point on the imperfect cylinder's middle surface, given its perfect radius.

$$\begin{aligned}\delta(\theta, Z) = \delta_0 \frac{\delta_\theta(\theta)}{\delta_0} \frac{\delta_Z(Z)}{\delta_0} &= \delta_0 \mathrm{e}^{-\frac{\pi}{\Lambda}|r\theta|} \left[\cos\left(\frac{\pi}{\Lambda}|r\theta|\right) + \sin\left(\frac{\pi}{\Lambda}|r\theta|\right)\right] \\ &\cdot \mathrm{e}^{-\frac{\pi}{\Lambda}\left|Z-\frac{L}{2}\right|} \left[\cos\left(\frac{\pi}{\Lambda}\left|Z-\frac{L}{2}\right|\right) + \sin\left(\frac{\pi}{\Lambda}\left|Z-\frac{L}{2}\right|\right)\right]\end{aligned} \tag{4.3}$$

It is worth noting at this point that there is a distinction between the algebraic amplitude δ_a and the measured depth δ_m of the dimple or weld depression, as illustrated in Figure 4.6. However, according to prEN 1993-1-6 [19], the difference is insignificant when using the expressions above and the tolerance requirements defined in the standard.

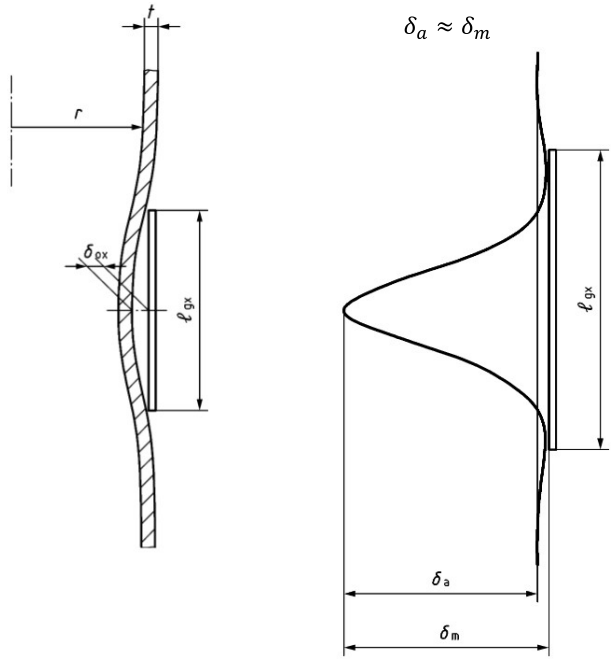

a) Tolerance measurement

b) Imperfection amplitudes

Figure 4.6: Consistent choice of imperfection amplitude [19, ed.]

4.1.2 Boundary Conditions

This section describes the constraints and applied loads on the models. In line with today's common modelling practice as revealed by Sadowski et al. [37] and inspired by recent research papers about similar topics, two reference points are created on the cylinder axis at the top and bottom and connected via rigid body kinematic coupling to the nodes along the top and bottom edges of the cylinder, respectively, as illustrated in Figure 4.7. In that way, point loads and global constraints can be easily applied in the reference points, and reaction forces can also be extracted with ease. Furthermore, due to the rigid body coupling, the initial circular shape of the cross-sections at the top and bottom edges is preserved, eliminating the need for physical modelling of a ring stiffener on top.

Global constraints

Global constraints are defined directly in the reference points. As described in section 3.2.1, the majority of the models are to act as cantilevers, while a few cylinders with clamped edge nodes are used for model validation. In case of cantilever models, all six degrees of freedom (DOF) are constrained in the bottom reference point, and

all six DOF are free in the top reference point. In case of fixed models, rotation around the Y-axis is kept free, while other DOF are constrained in both reference points, corresponding to the boundary conditions prescribed in EN 1993-1-6 Annex E. In case of half-cylinder models, symmetry boundary conditions are applied to all nodes on the circumferential symmetry plane, including the reference points. Since the symmetry plane coincides with the XZ-plane, displacement along the Y-axis and rotation around the X and Z-axes are constrained in those nodes. Global boundary conditions are visualised in Figure 4.7.

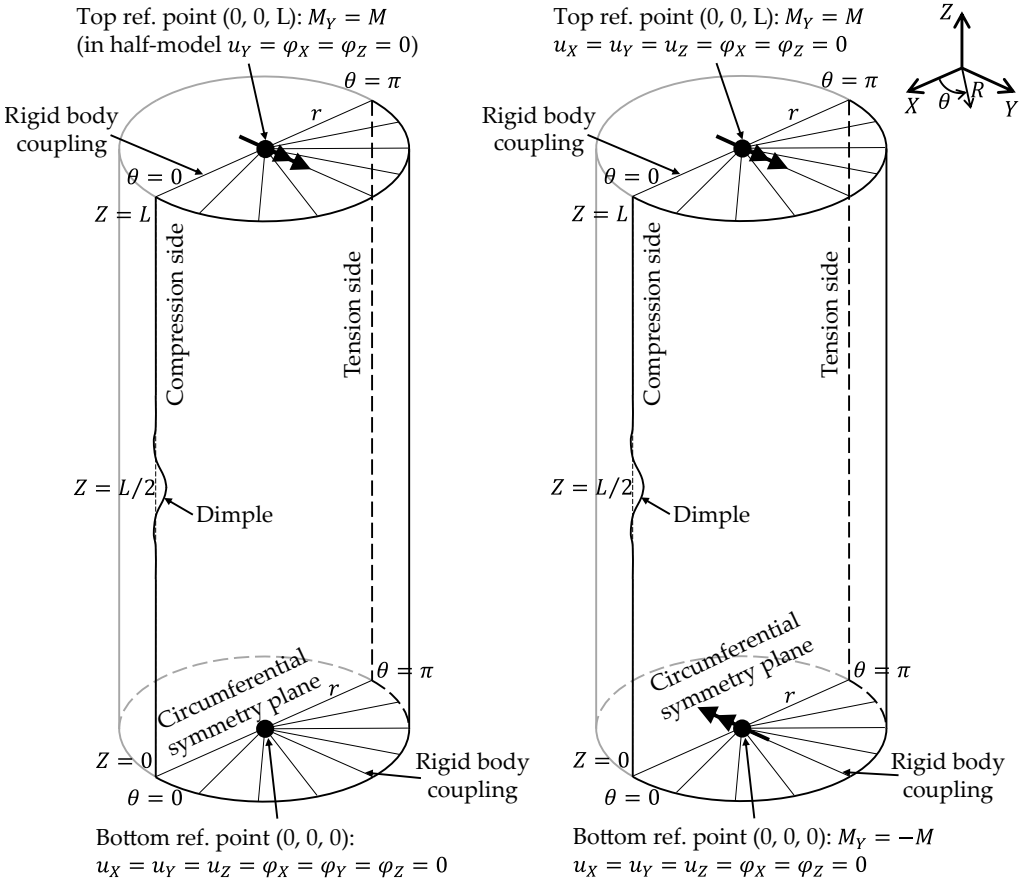

Figure 4.7: Boundary conditions in the models

Local constraints

Constraints locally within the model are established between the reference points and the edge nodes at the top and bottom of the cylinder via rigid body kinematic coupling. Coupling in general means forcing certain DOF in one node to be dependent on the DOF in another node. The latter is usually called the primary or master node, where DOF are retained, whereas in the other, called the secondary or slave node, DOF are removed from the matrix equations and are determined in another way, depending on the type of the chosen coupling. In case of simple coupling constraints, DOF in the slave node are forced to have the same solution as the corresponding ones in the master node. In case of rigid surface constraints, also referred to as rigid-body

kinematic coupling, DOF solutions are calculated using constraint equations ensuring that certain deformations in the slave node are controlled by the rigid-body motion of the master node. [38]

There are several different methods in Ansys Mechanical to create coupling. However, only one of them is able to account for large rotations in the model. It is called the internal multipoint constraint (MPC) approach, which builds MPC equations internally based on the contact kinematics and can be used to model different types of coupling, including the two mentioned above. [38]

The desired rigid body kinematic coupling in the project is modelled as rigid surface-based constraints with the MPC formulation. All nodal DOF on the top and bottom edges of the cylinder, in the software referred to as the contact surfaces, are coupled to the rigid body motion of the corresponding reference point, in Ansys called the pilot node or the target surface. The contact surfaces are generated using CONTA177 elements placed on the edges of the shell elements between their nodes. The target surfaces are created with TARGE170 elements consisting of a single pilot node at the reference points. The nodes of the contact elements are then automatically connected to the single node of the target element as shown in Figure 4.8, where the lines represent rigid constraints. Since all six DOF are constrained, these connections are equivalent to MPC184 rigid beam elements in Ansys. Due to these constraints, the contact surfaces remain rigid, and thus the top and bottom edges of the cylinder retain their original shape, i.e. remain circular.

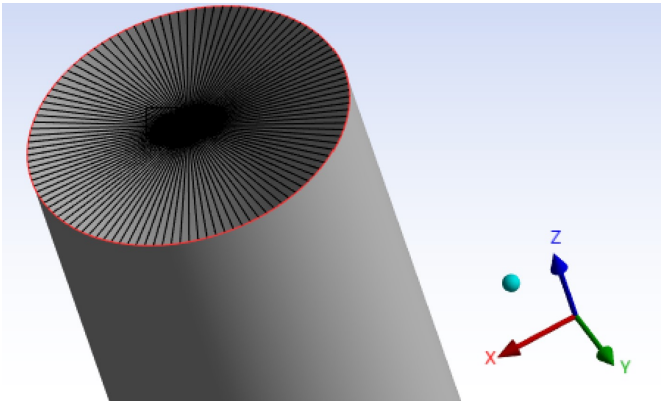

Figure 4.8: MPC

Loading

As described in section 3.2.1, a set of models is subjected to uniform bending moment around the Y-axis. The load can be applied either as a force or as a prescribed deformation at the pilot node located at the top of the cylinder, as illustrated in Figure 4.9 a). By prescribing a force or deformation at the pilot node, the program automatically computes the corresponding values in all DOF at the edge nodes using the MPC formulation, which ensures consistent deformation or load distribution.

Another set of models, experiencing a linearly increasing moment, is generated by applying a shear force along the X-axis together with a bending moment around the Y-axis at the pilot node, or a lateral deformation together with a rotation, depending on whether force or displacement control is chosen.

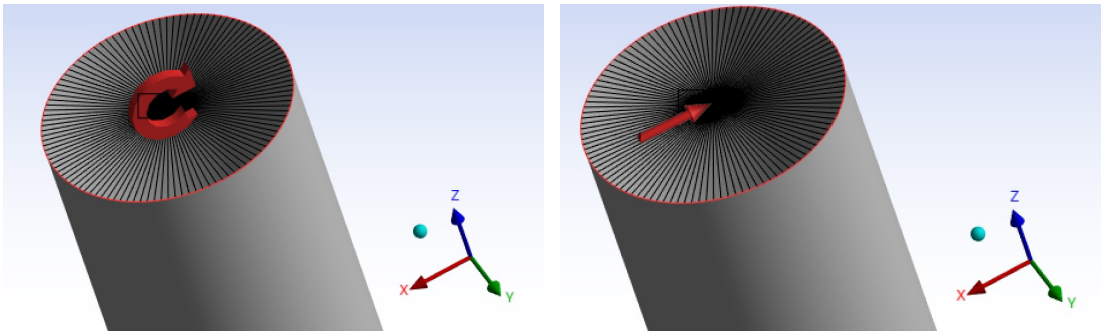

a) Bending moment or rotation b) Shear force or lateral displacement

Figure 4.9: Loads at pilot node

In this project, loads are applied in the form of forces. For each analysis, an appropriately large bending moment is applied compared to the expected resistance of the model. The magnitude of the applied moment is determined using the existing analytical expressions and may be slightly increased to avoid underestimating the load. If the load is underestimated, the model will not reach failure, thus, the actual resistance of the model will not be captured, and the results will be unusable. Applying a load close to the actual resistance improves the accuracy of the results, and since it is quite difficult to determine the value of the deformation at which the model is expected to fail in nonlinear analyses, force control is preferred to deformation control. Since the applied load varies between the analyses, the procedure for determining it is further elaborated in section 4.2. Note that in the case of the half-cylinder, half of the load applied to a full cylinder is used.

4.1.3 Material Model

The material used in the FE models is non-alloy structural steel conforming to EN 1993-1-1 [8] and EN 10025-2 [39], which is considered an isotropic material. Some of the analysis types in the project assume linear elastic material behaviour, while others include plasticity. In the latter cases, a bilinear material model is used as illustrated in Figure 4.10. The linear elastic behaviour of the material is described by the modulus of elasticity E and the Poisson's ratio ν. The plastic region of the chosen material model is defined by the yield strength f_y and the tangent modulus E_t. The value of all four material properties selected for the FE models is specified in the following.

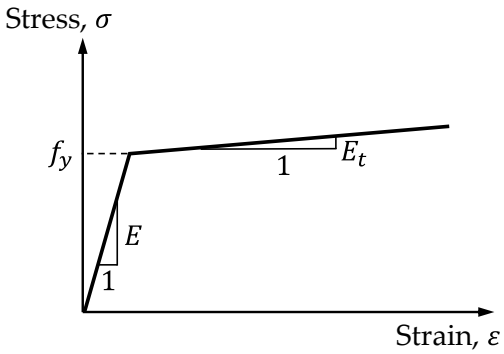

Figure 4.10: Bilinear material model

Modulus of elasticity

Given that most analysis types in the project focus on instability, the modulus of elasticity for carbon steel is taken as $E = 200$ GPa in accordance with prEN 1993-1-6 [19] and prEN 1993-1-14 [26].

Poisson's ratio

The Poisson's ratio of the material in the elastic range is taken as $\nu = 0.3$ in accordance with EN 1993-1-1 [8] and prEN 1993-1-6 [19].

Yield strength

The yield strength of carbon steel is selected based on a steel grade in accordance with material standard EN 10025-2 [39]. Monopiles are usually made of structural steel S355 [40], where 355 in the grade designation indicates the nominal yield strength in MPa for thickness 16 mm and below. The nominal yield strength for other thickness ranges is shown in Table 4.1. Different thicknesses within the interval $[10\text{ mm}, 500\text{ mm}]$ are used in the project. However, since the relative slenderness in the analytical buckling verification method is also dependent on f_y, it would be impracticable to vary both the yield strength and the thickness. Therefore, it is decided to set $f_y = 315$ MPa in all models corresponding to the nominal yield strength of the mean thickness in the project.

Table 4.1: Nominal yield strength of S355 [39]

Thickness, t (nom) [mm]	$\leq$16	>16 $\leq$40	>40 $\leq$63	>63 $\leq$80	>**80** $\leq$**100**	>100 $\leq$150	>150 $\leq$200	>200 $\leq$250	>250 $\leq$400
Yield strength, f_y (nom) [MPa]	355	345	335	325	**315**	295	285	275	265

Tangent modulus

Since the project focuses on monopiles and they typically experience elastic-plastic buckling, strain hardening is not considered, meaning that $E_t = 0$. Thus, the material model used in materially nonlinear analyses simplifies to linear elastic – perfectly plastic as depicted in Figure 4.11.

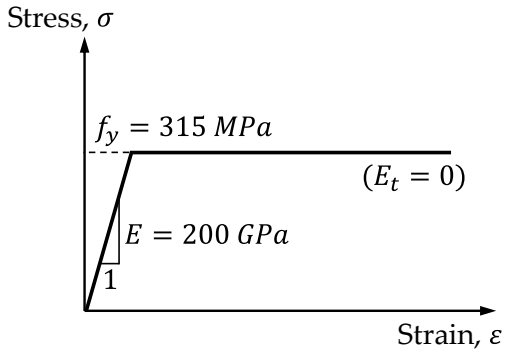

Figure 4.11: Material model used in the project

4.1.4 Mesh

As part of the FEA, the static model is discretised into an FE mesh. It is crucial that the mesh is robust when conducting numerical analyses, particularly when evaluating instability. A robust mesh implies the use of a proper element type, sufficient mesh density, no irregularities in the mesh, etc. This can be achieved by conducting a convergence analysis for mesh sensitivity, among others.

Since FEM is an approximation method, it is necessary to conduct a convergence analysis of the FE mesh to assess the accuracy of the obtained results. Convergence analysis is an iterative procedure where a given mesh is refined several times. After each iteration, selected quantities, e.g. the capacity or a deformation, are extracted for each model. After several iterations, the calculated results will not change significantly compared to the previous ones, which means that they have converged to or reached the exact value that can be obtained with the given mesh arrangement. It should be noted that different mesh arrangements and meshes of different element types converge at different paces, but theoretically, as the total number of degrees of freedom in the system goes towards infinity, the exact solution of the static model should be reached. [41]

In the following, candidate element types are presented, a parameter for defining element sizes is introduced, and a mesh sensitivity analysis is conducted to determine the appropriate element type and size.

Element types

There are different types of finite elements that can be utilised, including both solid and shell elements. Shell elements are based on shell theory, which allows efficient analysis of shell structures by reducing the 3D problem to a 2D one [42]. Shell elements can be classified as either thin or thick. For thick structures, solid continuum elements can also be used, resulting in a fully 3D analysis that is more computationally demanding. According to Sadowski and Rotter [42], both thick and thin shell elements provide reasonable results for cylindrical structures with radius-to-thickness ratios as low as $r/t = 10$. This forms the basis for the use of shell elements in this project for all radius-to-thickness ratios.

The commonly used element type for numerical calculations of cylindrical shells is quadrilateral elements according to Sadowski et al. [37]. Two specific types of quadrilateral shell elements are considered in this project and shown in Figure 4.12. These elements have six DOF in each node; three for translations in the X-, Y- and Z-directions and three for rotations about the X-, Y- and Z-axes.

In Ansys, the 4-noded quadrilateral shell element is called SHELL181, see Figure 4.12 a). This element has linear shape functions, which may lead to less accurate results due to the limited flexibility. SHELL281, in Figure 4.12 b), is a quadrilateral shell element with midside nodes, giving a total of 8 nodes, and has quadratic shape functions. This makes the element more flexible, and it also fits the curved geometry of the structure better. These elements are applicable for thin and moderately thick shells [38].

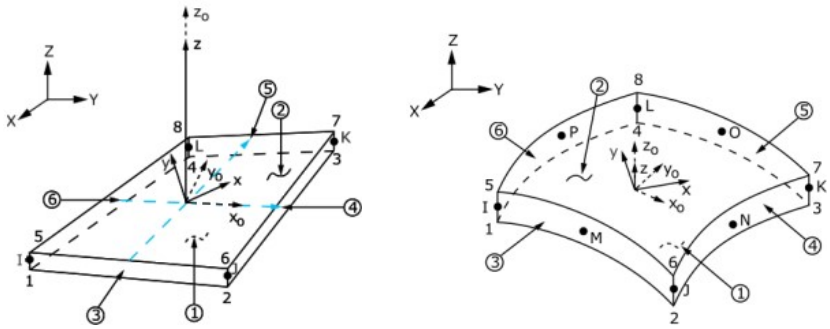

a) SHELL181 b) SHELL281

Figure 4.12: Shell elements in Ansys [38]

Comparing a mesh using SHELL181 and SHELL281, with the same number of elements, the calculation with SHELL281 will have increased computation time due to the higher number of DOF, see Table 4.2. However, convergence is often reached earlier for SHELL281, which means that a lower number of elements is enough to achieve appropriate accuracy.

Table 4.2: DOF for SHELL181 and SHELL281

Element type	Number of nodes	Number of DOF
SHELL181	4	24
SHELL281	8	48

Element size

For numerical analyses with cylindrical shells involving instability, the element sizes can depend on a parameter called the linear meridional bending half-wavelength Λ. Every buckle has a meridional and circumferential wavelength which depends on the loading type, Poisson's ratio and the geometry. The linear bending half-wavelength determines how deep the boundary layer goes, which is the region where the shell wall has to bend in order to match the conditions at the ends of the cylinder. In the case of very short cylinders, this boundary layer covers the whole length of the cylinder. Because of that, it's expected that buckling would be greatly limited. For cylinders subjected to bending, the half-wavelength is given in (4.4). [21]

$$\Lambda = \frac{\pi}{\left(3\left(1-\nu^2\right)\right)^{0.25}}\sqrt{rt} \approx 2.444\sqrt{rt} \tag{4.4}$$

There are various recommendations in the literature regarding the number of elements per Λ, which is used to determine the mesh refinement in areas of interest, such as around an imperfection. Sadowski and Filippidis [25], describing the background of the reference resistance design method in EN 1993-1-6 Annex E, state that at least 10 elements per Λ are used. However, in that study, the mesh consists of 4-noded elements. In DNVGL-RP-C208 for nonlinear shell analysis [43], it is mentioned that as few as 3 elements per Λ can be sufficient, depending on the chosen element type. In the following convergence analysis, the number of elements per Λ is varied to determine an appropriate value.

It is decided to use a uniform mesh for the models, and the meridional and circumferential element sizes are chosen in a way that the elements become squares. However, the final side lengths are slightly adjusted due to rounding.

Mesh sensitivity

A convergence analysis of the mesh sensitivity is carried out to select an appropriate element type and number of elements per Λ, thereby also the element size itself. Since Λ depends on the radius and thickness, different r/t ratios result in different element sizes. The analysis is conducted with the two presented element types and contains six different element sizes for each type. The element sizes used in the analysis are shown in Table 4.4. Additionally, convergence analysis is also performed for three different radius-to-thickness ratios: 10, 50 and 400. The geometry used for the different models is given in Table 4.3. Since the project focuses on cantilever cylinders in uniform global bending, the sensitivity analysis is performed with those boundary conditions.

Table 4.3: Geometry of cylindrical shells used in convergence analysis

r/t [-]	r [m]	t [m]	L [m]
10	4.0	0.40	30.0
50		0.08	
400		0.01	

Table 4.4: Element sizes for SHELL181 and SHELL281 [m]

SHELL181				**SHELL281**			
Elem. per Λ \ r/t	10	50	400	Elem. per Λ \ r/t	10	50	400
5	0.62	0.28	0.10	3	1.03	0.46	0.16
6	0.52	0.23	0.08	4	0.77	0.35	0.12
7	0.44	0.20	0.07	5	0.62	0.28	0.10
8	0.39	0.17	0.06	6	0.52	0.23	0.08
10	0.31	0.14	0.05	7	0.44	0.20	0.07
15	0.21	0.09	0.03	10	0.31	0.14	0.05

Two examples of the mesh are shown in Figure 4.13, namely a coarse and a fine.

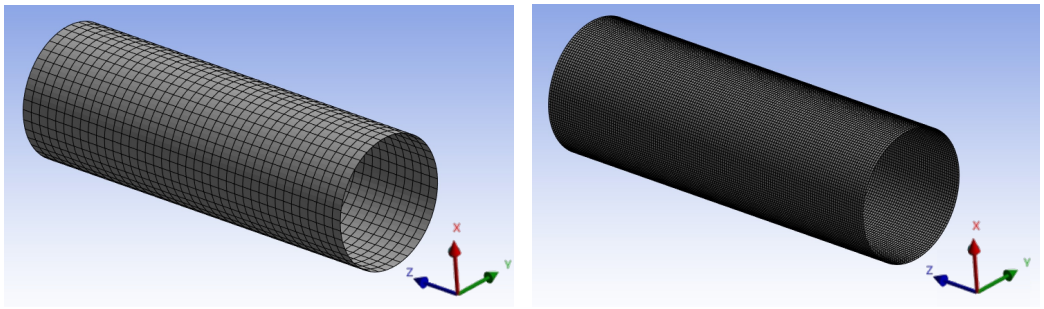

a) Element size 0.77 m b) Element size 0.20 m

Figure 4.13: Example of a coarse and a fine mesh

As mentioned, stability analyses are particularly sensitive to the mesh arrangement. Therefore, the sensitivity analysis is performed using LBA. In Figure 4.14, the elastic critical moment M_{cr} for each model is plotted together with the corresponding number of DOF.

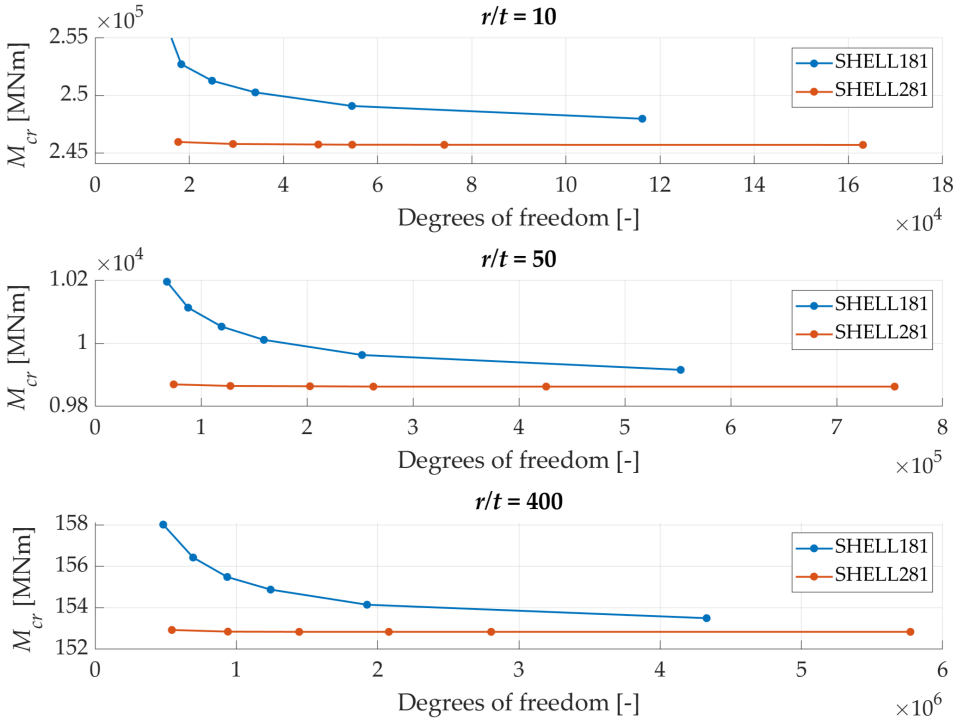

Figure 4.14: Convergence analysis

As seen in Figure 4.14, SHELL281 converges significantly faster than SHELL181 due to the quadratic shape functions. Even with 15 elements per Λ, SHELL181 does not converge completely. It is favourable to continue with SHELL281, as it allows for larger element sizes and requires fewer DOF, while still providing a converged result.

Convergence is achieved for the models using SHELL281 at element sizes equivalent to around 5 elements per Λ, and this will serve as the basis for the subsequent models in the project. However, in models with small r/t ratios where instability is no longer dominating, Λ can not be used as an appropriate measure for choosing element sizes. Therefore, an upper limit of 0.25 m is selected as the maximum element size.

4.2 Finite Element Analysis

The numerical analysis types presented in chapters 2 and 3 are described in the following regarding input parameters, together with examples of results and how they should be interpreted. The results are from single analyses of a cantilever cylinder in uniform global bending with a geometry of $r = 4.0$ m, $r/t = 50$ and $L = 30$ m, unless otherwise stated.

4.2.1 Linear Elastic Analysis

Linear Analysis – LA

The purpose of an LA is to perform a basic sanity check to ensure the model's correctness. A load is applied, and the six reactions at the bottom of the cylinder are examined, corresponding to three forces in the X-, Y-, and Z-directions, as well as three moments around the X-, Y-, and Z-axes. The reactions are checked to ensure that they match the expected values based on the applied load. Furthermore, it is checked whether the deformations are realistic under the applied load. In the following, an example is presented where a bending moment of 1.0 MNm acting around the Y-axis is applied at the pilot node at the top of the cylinder.

At the bottom, where the fixed support is located, the three force reactions should be zero. The moment reaction around the Y-axis should equal the negative value of the applied moment, and around the other two axes, the moment reactions should be zero. The base reactions from an LA are summarised in Table 4.5 and they are as predicted.

Table 4.5: Reactions at bottom pilot node

F_X	F_Y	F_Z	M_X	M_Y	M_Z
~ 0	~ 0	~ 0	~ 0	-1.0 MNm	~ 0

As expected, the applied load causes displacement in the X-direction and rotation around the Y-axis at the top pilot node, as shown in Table 4.6 and Figure 4.15.

Table 4.6: Deformations at top pilot node

u_X	u_Y	u_Z	r_X	r_Y	r_Z
0.14 mm	~ 0	~ 0	~ 0	$9.3 \cdot 10^{-6}$ rad	~ 0

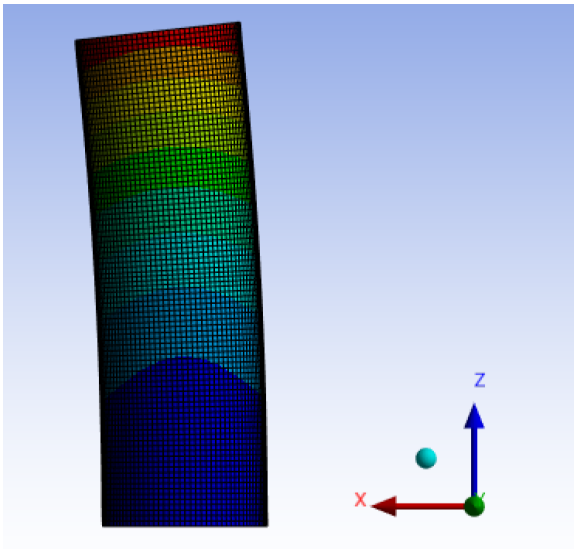

Figure 4.15: Deformation of cylinder

The values in Table 4.6 can also be compared to results from linear elastic analytical expressions, which can be determined based on the Bernoulli-Euler beam theory. The rotation at the top of the cylinder is calculated using the expression in (4.5), where I is the moment of inertia.

$$r_Y = \frac{M_Y L}{EI} = \frac{1 \text{ MNm} \cdot 30 \text{ m}}{200 \text{ GPa} \cdot 16.1 \text{ m}^4} = 9.3 \cdot 10^{-6} \text{ rad} \tag{4.5}$$

The horizontal displacement in the x-direction is calculated in (4.6).

$$u_X = \frac{M_Y L^2}{2EI} = 0.14 \text{ mm} \tag{4.6}$$

The values from the numerical model and the analytical expressions are identical, and it is therefore concluded that the model behaves as expected and follows the laws of mathematics and physics.

Linear Bifurcation Analysis – LBA

An LBA is a matrix eigenvalue calculation that automatically stops once the desired number of eigenvalues is extracted. LBA does not require further monitoring if a robust meshing scheme is applied, which implies the use of a proper element type, sufficient mesh density, etc. [44]

Ansys Mechanical offers two methods for buckling mode extraction: the Block Lanczos method and the subspace iteration method. According to the Ansys Mechanical APDL Product Help [38], the Block Lanczos solver performs well with models consisting of shell elements, and it is therefore used for LBAs in the project.

With an LBA, eigenmodes are extracted along with the corresponding buckling load multipliers required to reach that shape. In other words, a value is determined for the load needed for a perfect structure to lose its stability. The shape of the eigenmodes themselves indicates which areas become unstable first, i.e. where the shell bulges out, as seen in Figure 4.16.

In Figure 4.16, the first four eigenmodes of a cylindrical shell under uniform bending moment are shown. The bulges appear on the side of the cylinder where compressive stresses are present. The shape of the eigenmode appears differently depending on the applied load. This section only presents the eigenmodes for cylinders under a uniform moment. For cylinders experiencing a linearly increasing moment distribution, refer to section 6.1.1.

The linear elastic critical moment resistance M_{cr} is determined as the product of the applied load and the buckling load multiplier, which is the output extracted from the program. The first two eigenmodes are very similar, which explains why the values of the critical loads are almost identical, as shown in Table 4.7. The same applies to eigenmodes 3 and 4 — they look similar, and their critical loads are close in value.

Table 4.7: Critical load for first four eigenmodes

Eigenmode	M_{cr} [MNm]
1	8149.4
2	8149.5
3	8184.9
4	8185.3

The first eigenmode always corresponds to the lowest critical load that the structure can experience and is also the most likely to occur. Therefore, only the results for the first eigenmode are used throughout the project, even though infinitely many eigenmodes exist.

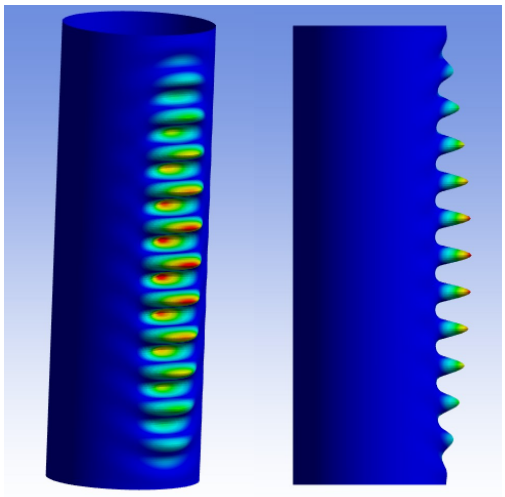

a) Eigenmode 1

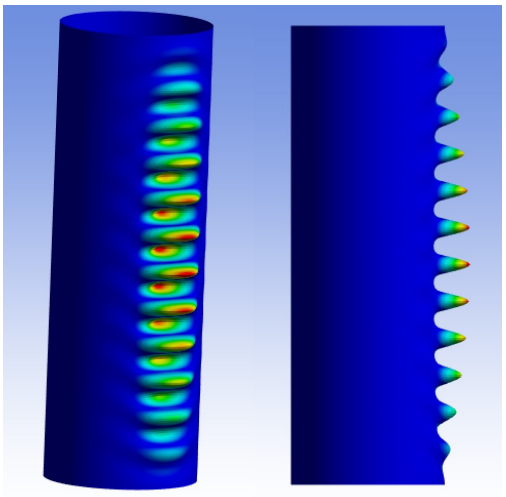

b) Eigenmode 2

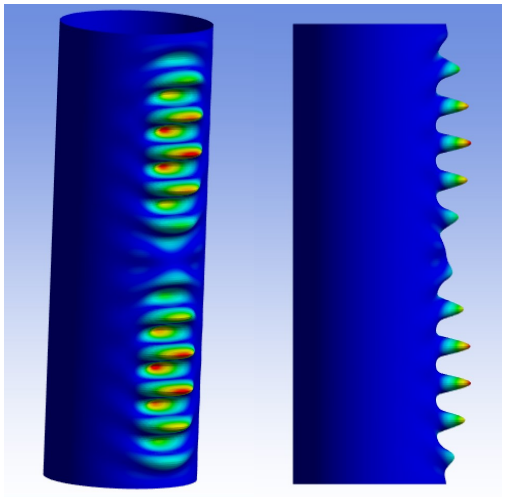

c) Eigenmode 3

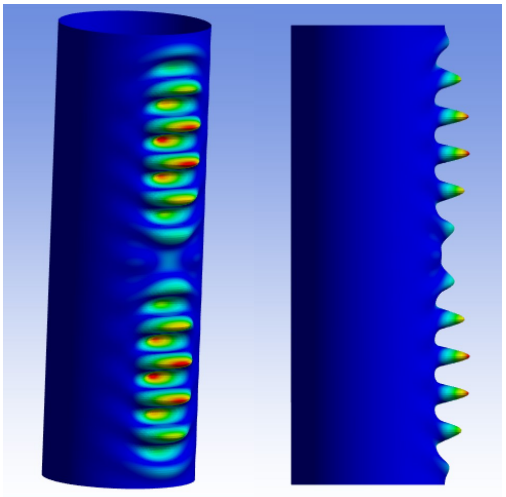

d) Eigenmode 4

Figure 4.16: First four eigenmodes in cantilever cylinder under uniform global bending

4.2.2 Nonlinear Analysis

Load step procedure

For nonlinear analyses, the equilibrium path can be determined by either using a force-controlled procedure or by combining the arc-length method with a force-controlled procedure, as illustrated in Figure 4.17. Although the arc-length method can also be applied with a displacement-controlled procedure, this approach is not used in the project.

In both procedures, the load is divided into increments and applied in several steps. In the force-controlled procedure, the increment in each step is positive. The disadvantage is that it is difficult to control, especially for highly nonlinear behaviour, and it cannot detect potential post-buckling behaviour with negative stiffness. In contrast, the arc-length method is a powerful tool to track the equilibrium path for nonlinear behaviour. This method allows for the tracking of the load-displacement path by enforcing a constraint which ensures that the solution remains on the equilibrium path, even when there are sudden changes in behaviour, such as buckling. The disadvantage of this method is that it is more time-consuming and computationally demanding. [45]

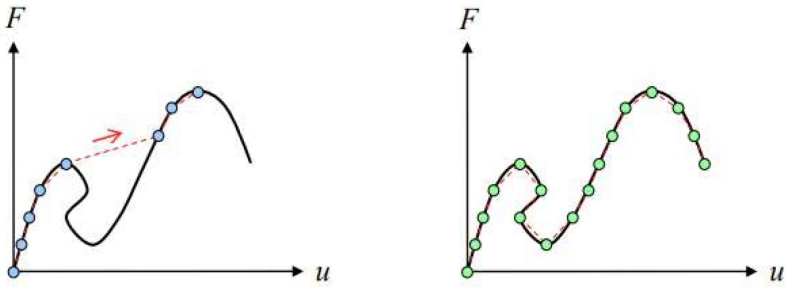

a) Force-controlled procedure b) Arc-length method

Figure 4.17: Load step procedures [45, ed.]

Both of the aforementioned methods, make use of the Newton-Rapson procedure, which is an iterative process of solving nonlinear equations, and is illustrated in Figure 4.18. The method relies on the fundamental equation of the finite element method, which is shown in (4.7), where $[K]$ is the global stiffness matrix, $\{u\}$ is the displacement vector, and $\{F\}$ is the load vector.

$$[K]\{u\} = \{F\} \tag{4.7}$$

The iteration proces in Figure 4.18 a) starts with calculating the internal forces $\{F_i^{nr}\}$ at a displacement $\{u_i\}$ by using a linearized stiffness matrix $[K_i]$, which is also evaluated at $\{u_i\}$. Next, a residual load $\{R_i\}$ is calculated as the difference between the applied load $\{F^a\}$ and the calculated internal loads. The residual is used to adjust the initial guess of the displacement with $\{\Delta u\}$. The new guess will be $\{u_{i+1}\}$ and the corresponding internal forces $\{F_{i+1}^{nr}\}$ are calculated using the updated stiffness matrix $[K_{i+1}]$. This process is repeated, and the residual is gradually reduced with each iteration as shown in Figure 4.18 b). In theory, reaching a residual of exactly zero

would require an infinite number of iterations. In practice, a tolerance is defined to determine how much the sum of the internal forces is allowed to deviate from the applied load. Once this tolerance is met, the solution is considered to have converged. [38]

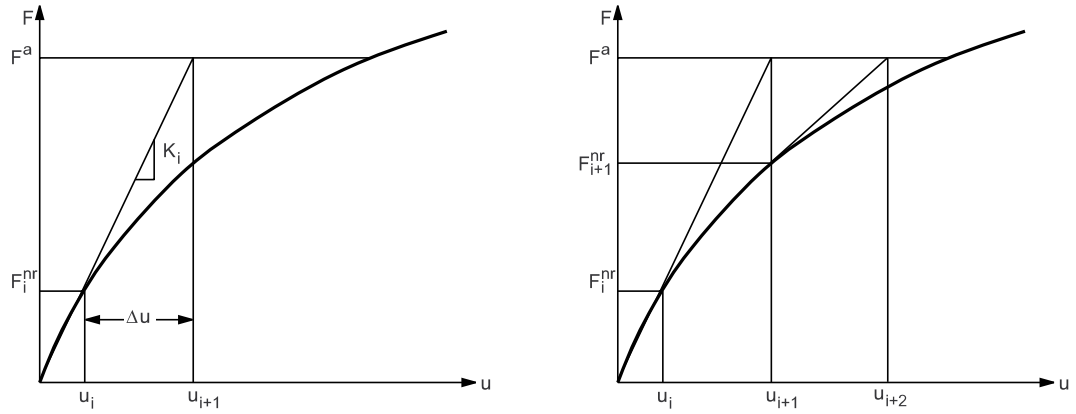

a) Iteration i b) Iteration i+1

Figure 4.18: Newton-Raphson method [38]

In the arc-length method, the load is not directly increased as in the Newton-Raphson procedure. Instead, a scalar parameter λ is introduced, which acts as a load proportionality factor (LPF). The method prevents fluctuations in step size during the iterations by keeping the solution within a fixed distance — a specified arc length, as shown in Figure 4.19.

For problems involving sharp changes in the load-displacement curve or materials with path-dependent behavior, it is important to control both the initial arc-length radius and how much it is allowed to change during the solution. In the arc-length method, the radius is automatically adjusted at each substep based on the degree of nonlinearity present. To ensure stability and avoid excessively large or small steps, this variation is constrained by predefined maximum and minimum multipliers. [38]

The initial arc-length radius is adjusted automatically but it is propotional to the initial load factor. The initial load factor is given in (4.8), where Time is set to 1, corresponding to the full application of the load.

$$\text{Intital load factor} = \frac{\text{Time}}{\text{Initial number of substeps}} \tag{4.8}$$

The initial number of substeps defines how the load is incrementally applied in the initial stages of the analysis, affecting the convergence behaviour and the stability of the solution. A higher number of substeps results in smaller load increments, which can improve accuracy but at the cost of increased computational time. Conversely, a lower number of substeps may reduce computational time but can potentially lead to convergence issues, especially for highly nonlinear problems.

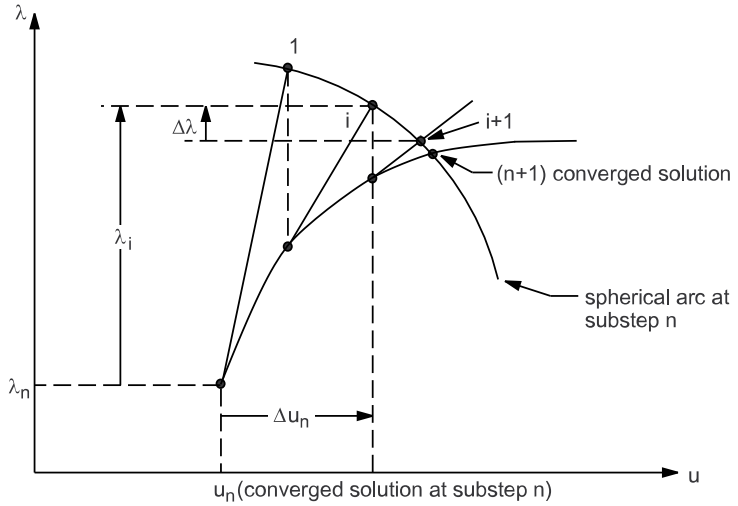

Figure 4.19: Arc-length approach with Newton-Raphson method [38, ed.]

An optimal choice of the *initial number of substeps, maximum* and *minimum multipliers* is crucial for obtaining an accurate and not too computationally consuming solution. The maximum and minimum multipliers remain the same throughout all analyses with values of 1 and 1/1 000 respectivaly. The initial number of substeps is different for each analysis, and an appropriate value is found using sensitivity analysis for each analysis type below.

Termination

Modern FE solvers can track nonlinear equilibrium paths far into the post-buckling domain. However, in this project, only the first critical point is of interest, as it represents the resistance of the structure, and the load on the structure should not go beyond that point. Therefore, it is chosen to terminate the analysis at the critical point.

There are several failure criteria for shells, and they differ depending on the analysis type. The failure criterion in a materially nonlinear analysis is typically based on the start of yielding, which occurs when the material stress state reaches the yield surface defined by the chosen criterion, e.g. the von Mises criterion. As for geometrically nonlinear analyses, EN 1993-1-6 defines four criteria that represent a state of failure for a GMNIA, as visualised in Figure 4.20. These criteria can also be applied to the other geometrically nonlinear analyses, i.e. GNA, GNIA and GMNA.

The most common manifestations of unstable post-buckling behaviour are represented by criteria C1 and C2, where buckling occurs either at a limit point or a bifurcation point. C1 covers limit load buckling, whereas C2 covers bifurcation buckling. Criteria C3 and C4 represent cases with complex behaviour, as the equilibrium path continues to rise after buckling, although there may be a 'kink' where the curve changes slope. Criteria C3 and C4 are conservatively set as a reliable way to manage cases with stable post-buckling behaviour. C3 corresponds to termination of the analysis when the largest tolerable deformation is reached, and C4 corresponds to the point at which the highest equivalent stress in the system reaches the yield limit. [44]

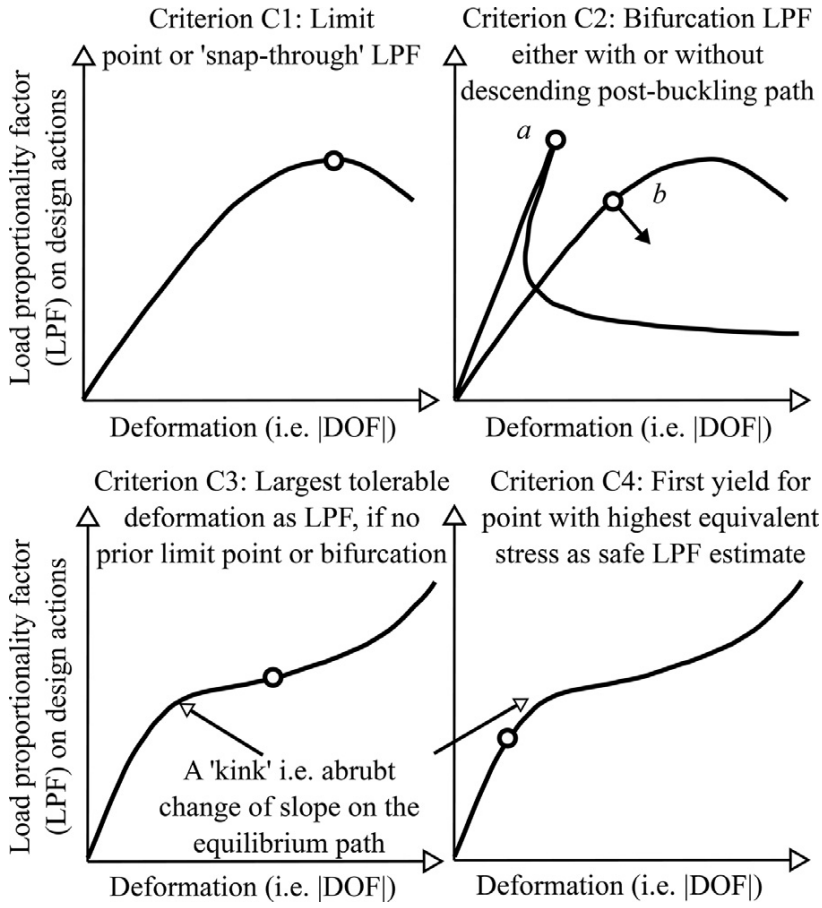

Figure 4.20: Definition of buckling resistance from GMNIA according to the four failure criteria [44]

In Ansys, a command is issued for the materially and geometrically nonlinear analyses to terminate when the first limit point has been reached. The first limit point is the point in the response history when the tangent stiffness matrix becomes singular, i.e. the point at which the stiffness becomes nonpositive. In a materially nonlinear analysis, this means the analysis is terminated at the point of material failure, while in a geometrically nonlinear analysis, it is terminated at the occurrence of buckling. [38] With the termination command used in Ansys, it is not possible to automatically terminate the analysis if a 'kink' occurs. However, this is not an issue, as these cases are most likely not relevant for cylindrical shells, where buckling is usually characterised as unstable and the stiffness decreases rather than increases.

Materially Nonlinear Analysis – MNA & MNIA

The purpose of an MNA and MNIA is to determine the plastic resistance of the perfect and imperfect structure, respectively, which is found as the point where the analysis stops due to material failure, i.e. $M_{R,MNA} = M_{pl}$ and $M_{R,MNIA} = \kappa M_{pl}$. A materially nonlinear analysis is based on the small deformation theory to determine the plastic collapse mechanism, which manifests as a plateau on the equilibrium path as shown in Figure 2.24. However, the results for MNA shown in Figure 4.21 do not display this

plateau, as the analysis is terminated as soon as M_{pl} is reached.

As for the equilibrium path of MNIA, the resistance of the model is reached slowly, which requires more load increments and thus increases the computational time to obtain a final result. This behaviour can occur for shells dominated by local bending, where a clear horizontal plateau may not appear [44]. For this particular cylinder, such a case occurred due to the effect of the imperfection.

The load applied to the cylinder in both types of analyses corresponds to the analytically calculated M_{pl}. This serves as a good estimate, as the analytical values of M_{pl} are found to be slightly higher than the numerical ones. This is further discussed in section 5.5. While it is expected that $M_{pl,I}$ is smaller than M_{pl}, the difference is small for certain geometries, and therefore the same load is applied for MNIA.

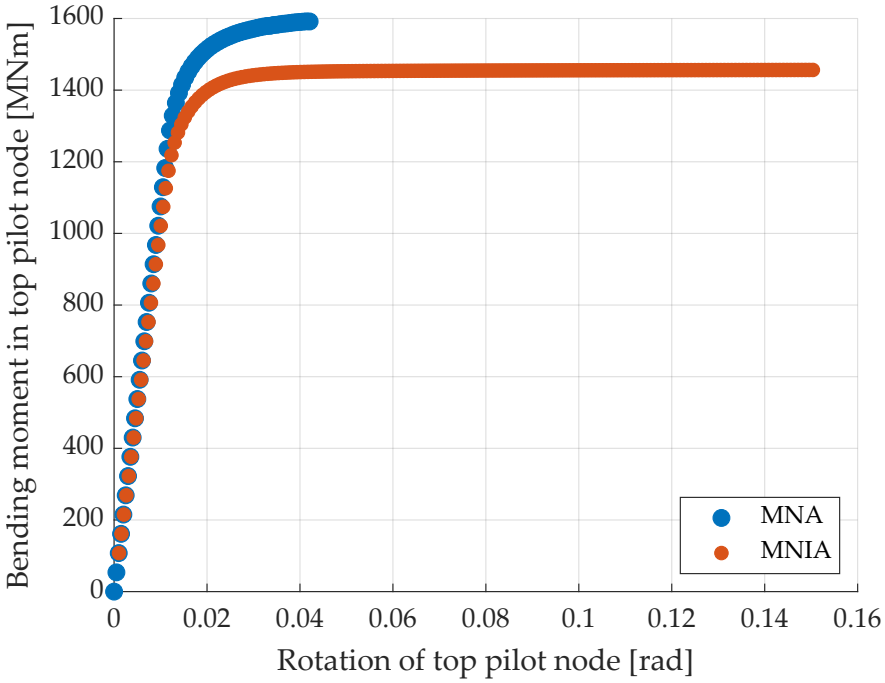

Figure 4.21: Equilibrium path for MNA and MNIA

A sensitivity analysis is performed based on MNA to determine a suitable initial number of substeps. The convergence of the LPF is investigated for $r/t = 50$ using the geometry provided in Table 4.3. The results are shown in Table 4.8, where it can be seen that the solution has converged at an initial number of substeps of 30, which is therefore adopted in subsequent MNAs and MNIAs.

Table 4.8: Sensitivity analysis of initial number of substeps for MNA

Initial number of substeps	LPF
20	0.976
30	0.979
40	0.979

Geometrically Nonlinear Analysis – GNA & GNIA

With the GNA and GNIA, the elastic buckling reduction factors α_G and α_I can be determined as shown in (4.9).

$$\alpha_G = \frac{M_{R,GNA}}{M_{cr}} \quad \& \quad \alpha_I = \frac{M_{R,GNIA}}{\alpha_G M_{cr}} \tag{4.9}$$

where $M_{R,GNA}$ and $M_{R,GNIA}$ are the values at buckling.

The GNA and GNIA terminate when buckling occurs, i.e. a bifurcation or limit point is reached. In Figure 4.22, an example of an equilibrium path for the chosen geometry is shown. The equilibrium path for GNA is linear, indicating that a bifurcation point is reached. As for GNIA, the equilibrium path is almost linear, making it difficult to clearly identify a limit point. Therefore, it is most likely bifurcation-type buckling as well.

For GNA, a load of $M_{applied} = 2Ert^2$ is applied, corresponding to M_{cl} multiplied by the largest possible C_m for the investigated geometries. This ensures that the applied load is greater than $M_{R,GNA}$ in all cases. For GNIA, the applied load must be lower than that for GNA. It is therefore chosen that $M_{applied} = M_{R,GNA}$.

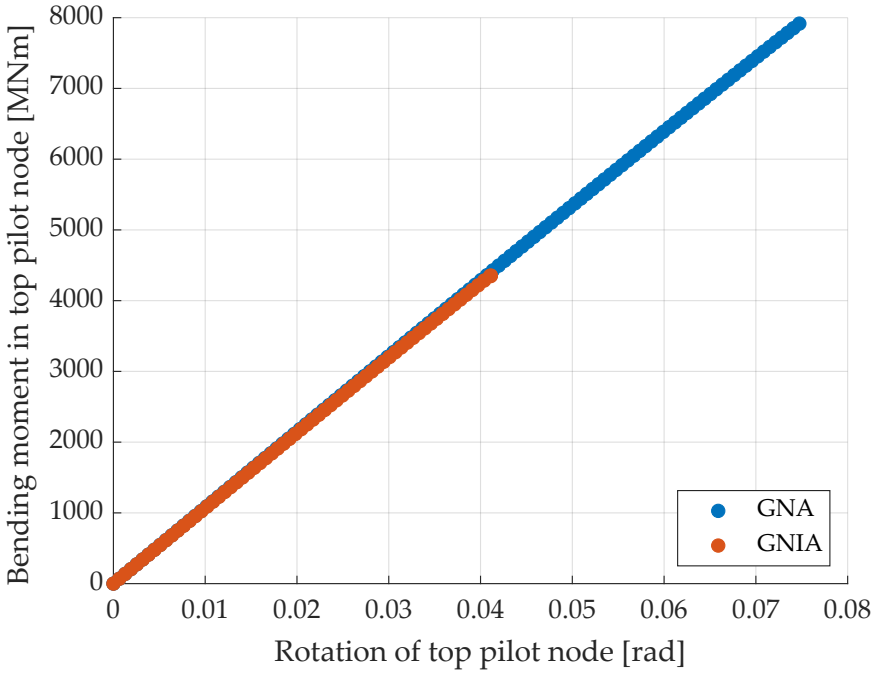

Figure 4.22: Equilibrium path for GNA and GNIA

Similarly to MNA, a sensitivity analysis is carried out for GNA for $r/t = 50$ and $r/t = 400$ with the geometries specified in Table 4.3. According to Sadowski and Filippidis [25], a higher value of the initial number of substeps is required for higher r/t ratios, which is also demonstrated in Table 4.9. For $r/t = 50$, an initial number of substeps of 50 is sufficient to obtain an accurate result. Unfortunately, the same cannot be said for $r/t = 400$, where convergence is not achieved even with an initial number of substeps of 200.

In the study presented by Sadowski and Filippidis [25], capacity curves were computed using different load increments, such as 0.005 and 0.001, corresponding to

initial numbers of substeps of 200 and 1000, respectively. In the elastic region, nearly identical results were obtained for both 200 and 1000 substeps, which is why an initial number of 200 substeps was adopted in the study [25]. Accordingly, the same value is adopted in this project to avoid overly computationally demanding solutions.

Table 4.9: Sensitivity analysis of initial number of substeps for GNA

Initial number of substeps	LPF	
	$r/t = 50$	$r/t = 400$
50	0.847	0.997
100	0.847	0.968
200	0.847	0.963

Geometrically and Materially Nonlinear Analysis – GMNA & GMNIA

GMNA and GMNIA analyses terminate at the limit point when either buckling or material failure occurs. In Figure 4.23, it can be seen that a limit point has been reached for both analyses. The GMNA provides the resistance of the perfect structure, which is found by multiplying the LPF at termination by the applied load. The same is done with the result of the GMNIA to determine the characteristic resistance of the structure with imperfections.

The load applied on the models in GMNA is chosen as the smallest of M_{pl} or $M = 2Ert^2$. This ensures that the load is neither too large nor too small. In GMNIA, an appropriate value of the applied load is the resistance determined in GMNA, i.e. $M_{applied} = M_{R,GMNA}$.

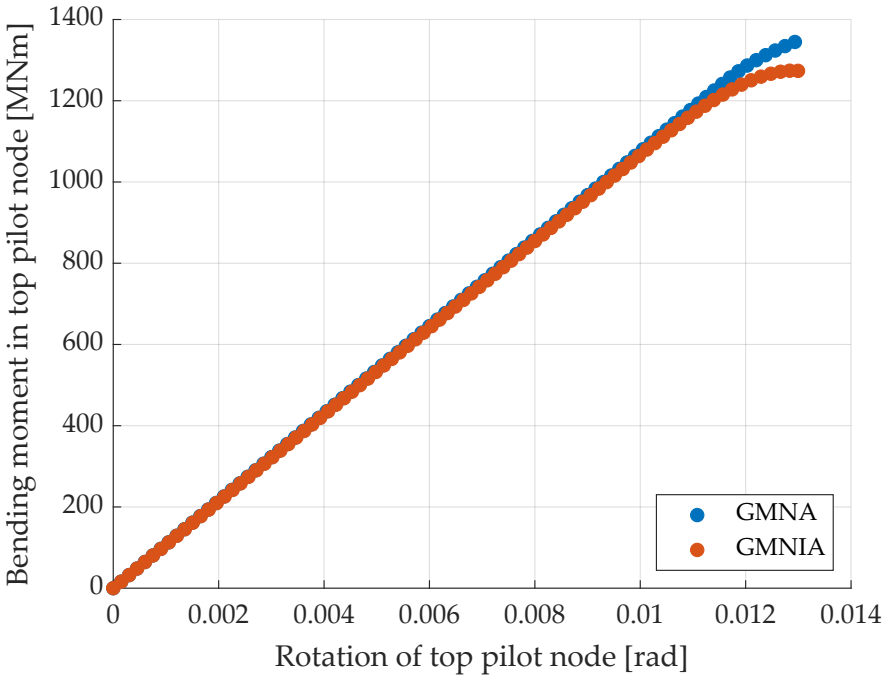

Figure 4.23: Equilibrium path for GMNA and GMNIA

A sensitivity analysis is performed for GMNA with four different r/t ratios, with

the results shown in Table 4.10. For r/t ratios up to 200, convergence is achieved using 100 as the initial number of substeps, which is also chosen for the subsequent analyses. For r/t ratios of 300 and 400, convergence is unfortunately not achieved. Therefore, following the same reasoning as described in the sensitivity analysis for GNA, an initial number of substeps of 200 is selected for r/t ratios above 200

Table 4.10: Sensitivity analysis of initial number of substeps for GMNA

Initial number of substeps	LPF			
	$r/t = 50$	$r/t = 200$	$r/t = 300$	$r/t = 400$
50	0.841	0.771	0.737	0.894
100	0.911	0.770	0.723	0.882
200	0.911	0.770	0.719	0.877

4.2.3 Comparison of analysis types

As expected, all analysis types with imperfections exhibit a lower resistance than the corresponding ones without imperfections, as seen in Figure 4.24. Note that all curves follow each other closely initially, indicating that the influence of nonlinearity is minimal in that region.

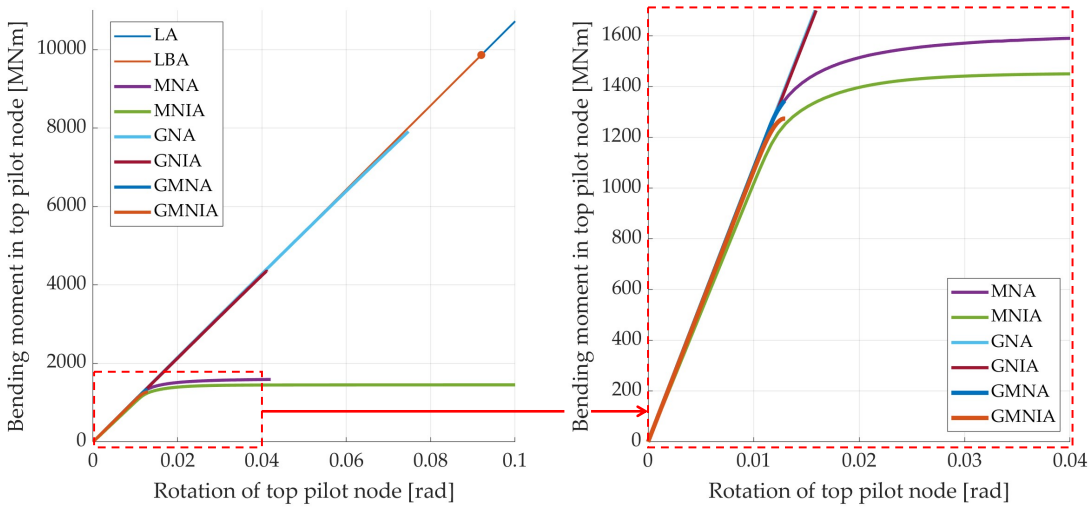

Figure 4.24: Equilibrium path for all analysis types

4.3 Model Validation

A numerical model has to be verified and validated to ensure that the results are realistic and reliable. Verification includes checking the sensitivity of results to discretisation, as done in section 4.1.4, and other input parameters such as the initial number of substeps, as demonstrated in section 4.2, as well as examining the calculated results in qualitative and quantitative ways using engineering judgement. Validation is performed by comparison with known accurate analytical or experimental results to prove that the numerical model adequately represents the real world. [26] Since no reliable experimental data exist for cylindrical shells subjected to global bending,

validation can only be performed using known analytical results. It is not possible to validate a cantilever model corresponding to a monopile, as there is no corresponding analytical method for comparison. Instead, the validation is based on a model that is fixed in both ends and subjected to uniform bending moment, as described in section 4.1.2, which aligns with the assumptions behind the method in EN 1993-1-6 Annex E. Two distinct geometries are examined, given in Table 4.11, one exhibiting elastic-plastic behaviour and the other purely elastic behaviour.

Table 4.11: Dimensions of cylindrical shells for model validation

Behaviour	r [m]	t [m]	r/t	L [m]
Elastic-plastic	4.0	0.08	50	15.0
Elastic	4.0	0.01	400	15.0

Various types of numerical analysis are performed to determine certain capacity curve parameters as well as different types of resistances. The results and the corresponding deviations between the analytical and numerical values are given in Table 4.12 and 4.13. It should be noted that for $r/t = 400$, only analyses without imperfections are conducted.

Table 4.12: Comparison of analytical and numerical results for $r/t = 50$ and FTQC C

Parameter	Analytical result	Numerical result	Analysis type	Deviation
M_{cr} [MNm]	9 790	9 912	LBA	1.2%
M_{pl} [MNm]	1 613	1 590	MNA	-1.4%
κ [-]	0.97	0.95	MNIA	-2.2%
α_G [-]	0.89	0.96	GNA	8.2%
α_I [-]	0.51	0.55	GNIA	7.0%
$M_{Rk,per}$ [MNm]	1 555	1 468	GMNA	-5.6%
M_{Rk} [MNm]	1 342	1 339	GMNIA	-0.2%

Table 4.13: Comparison of analytical and numerical results for $r/t = 400$

Parameter	Analytical result	Numerical result	Analysis type	Deviation
M_{cr} [MNm]	152.2	152.9	LBA	0.4%
M_{pl} [MNm]	201.6	196.2	MNA	-2.7%
α_G [-]	0.90	0.96	GNA	6.8%
$M_{Rk,per}$ [MNm]	136.2	140.2	GMNA	2.9 %

LBA

The elastic critical moment resistance M_{cr} is determined as the classical elastic critical moment M_{cl} multiplied by a parameter C_m, as shown in (4.10) and earlier described in section 2.3.2.

$$M_{cr} = C_m M_{cl} \tag{4.10}$$

As seen in Table 4.12 and 4.13, the deviation between the analytical and numerical values of M_{cr} is minor, with the numerical results being slightly higher than the analytical ones.

MNA

In EN 1993-1-6, the plastic moment resistance is calculated simply by multiplying the plastic section modulus W_{pl} by the characteristic yield strength f_{yk}, as seen in (4.11). The plastic section modulus W_{pl} for a shell is an approximate lower-bound expression, as the term containing only the thickness is disregarded. It is common practice to calculate the plastic resistance by considering full utilisation of a cross-section's capacity. However, somehow, the numerical results are still lower than the analytical ones. This is addressed later in the next chapter.

$$M_{pl} = W_{pl} f_{yk} = \left(4r^2 t + \frac{1}{\cancel{3}}\cancel{t^3}\right) f_{yk} \simeq 4r^2 t f_{yk} \tag{4.11}$$

MNIA

The expression for κ in prEN 1993-1-6:2023, given in (4.12), is a simplified form of the expression that applies to thin cylinders with $r/t \geq 100$. The equation below is used to determine the value of $\kappa = 0.97$, which is given in Table 4.12.

$$\kappa_{\text{EC}} = 0.2 + \frac{0.8}{1 + 0.23(\delta_0/t)^2} \tag{4.12}$$

Wang et al. [28], who provided the background of the method in EN 1993-1-6 Annex E, proposed the full expression and it is shown in (4.13). In addition, an expression is also given for thick cylinders with $r/t = 10$. If the r/t ratio lies between 10 and 100, interpolation can be performed as shown below in (4.15).

$$\kappa_{\text{thin}} = 0.2 + \frac{0.8}{1 + 0.014(\delta_0/t)^{0.2} + 0.23(\delta_0/t)^2} \qquad \text{for } r/t \geq 100 \tag{4.13}$$

$$\kappa_{\text{thick}} = \frac{1}{1 + 0.093(\delta_0/t)^{1.3} + 0.222(\delta_0/t)^{1.9}} \qquad \text{for } r/t = 10 \tag{4.14}$$

$$\kappa_{\text{interp}} = \kappa_{\text{thick}} + (\kappa_{\text{thin}} - \kappa_{\text{thick}}) \left(\frac{r/t - 10}{90}\right)^{0.35 - 0.05\delta_0/t} \qquad \text{for } 10 < r/t < 100 \tag{4.15}$$

Calculating κ_{interp} for the geometry with $r/t = 50$, there is no deviation between κ_{interp} and the numerical result: $\kappa_{\text{interp}} = \kappa_{\text{numerical}} = 0.95$. This shows a strong agreement between the numerical model and the expression for κ_{interp}. This is expected, as the expression is based on numerical analyses, which confirms that the constructed numerical model is reliable.

GNA

A higher value of α_G is favourable, as the reduction of the buckling resistance becomes smaller. Based on the results in Table 4.12, it can be seen that the value of α_G is higher when determined numerically. As seen in equation (4.16), α_G is either equal to 0.9

when $\Omega < 0.5$ or a lower value when $\Omega \geq 0.5$. For the geometry with $r/t = 50$, $\Omega = 0.5$ and for $r/t = 400$, $\Omega = 0.2$. A limit of $\alpha_G = 0.9$ is imposed for $\Omega < 0.5$, which explains why the analytical and numerical results are not the same.

$$\begin{aligned} \alpha_G &= 0.9 && \text{for } \Omega < 0.5 \\ \alpha_G &= 0.5 + (0.38 \sin(0.85\Omega) + 0.48 \cos(0.85\Omega))\, e^{-0.8\Omega} && \text{for } \Omega \geq 0.5 \end{aligned} \tag{4.16}$$

GNIA

The imperfection reduction factor α_I, given in (4.17), depends on the imperfection amplitude δ_0 and Ω, which depends on the geometry. The expression is determined based on a fit of numerical results. The deviation between the value obtained from the expression and the result determined directly from the numerical model is likely due to the fitted expression not accurately capturing all data points, or being intentionally formulated to be slightly conservative.

$$\alpha_I = \frac{1}{1 + \left(0.7 + \frac{1.05}{1 + 0.42\Omega^{2.8}}\right)\left(\frac{\delta_0}{t}\right)^{0.7}} \tag{4.17}$$

GMNA and GMNIA

The analytical and numerical results for both GMNA and GMNIA show only minor deviations. This is observed for geometries in both the elastic-plastic region, $r/t = 50$, and the elastic region, $r/t = 400$. However, it appears that the geometries with higher r/t ratios may be slightly underestimated analytically. This will be investigated further in chapter 5 for cantilever cylindrical shells.

The model validation may be concluded by stating that, overall, there is a good correlation between the analytical and numerical results, particularly when comparing the characteristic resistance. This confirms that the numerical model has been set up correctly and behaves as intended.

This page is intentionally left blank.

5 Assessment of Analytical Method

This chapter presents the assessment and potential reformulation of the expressions for the capacity curve parameters from prEN 1993-1-6:2023 [19] Annex E, based on a series of numerical analyses of seven different types. FE analyses are performed as described in chapter 4 using models of set 1 as per section 3.2.1, i.e. cantilever cylinders in uniform global bending with a full-circumferential dimple, where applicable. The only difference between those models and the assumptions behind the method in EN 1993-1-6 is the static system. While EN 1993-1-6 uses cylinders supported at both ends, the FE models in the project are constructed as cantilever cylinders. Furthermore, the validity of the analytical method is formally limited to radius-to-thickness ratios of at least 50, but the assessment includes cylinders with r/t ratios as low as 8.

5.1 Preliminary Assessment

Prior to a detailed evaluation of the current analytical method, a brief preliminary assessment is conducted, comparing the main results, which forms the basis and determines the extent of further assessments and reformulations. The main result of the analytical method is the characteristic buckling moment resistance, calculated as the product of the buckling reduction factor and the reduced reference plastic moment, $M_{Rk} = \chi M_{pl,I}$. Numerically, this resistance can be obtained from a geometrically and materially nonlinear analysis on the imperfect structure, GMNIA. The analytical and numerical resistances are visualised in Figure 5.1 as a function of thickness and length for the normal fabrication tolerance quality class, FTQC C.

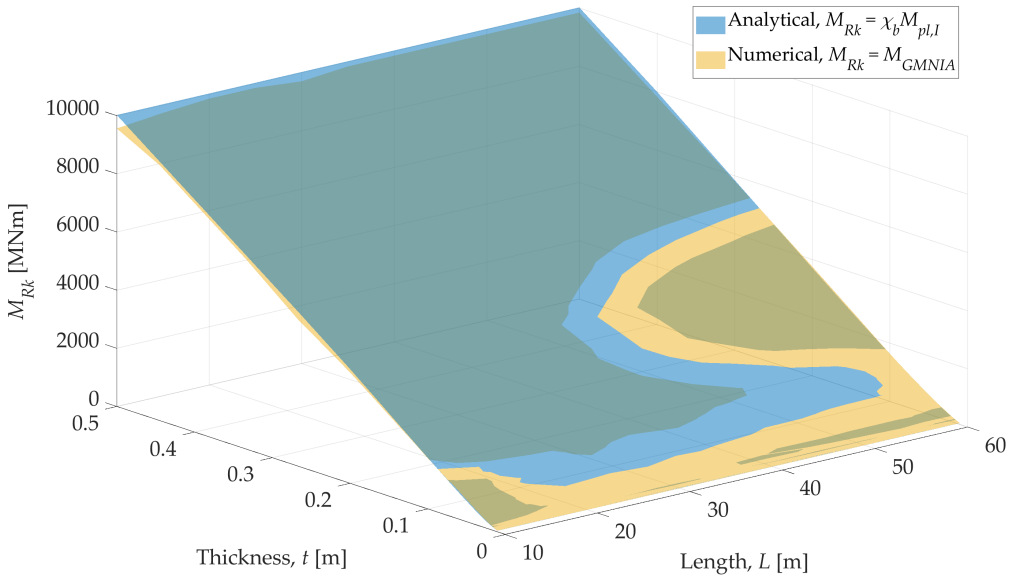

Figure 5.1: Comparison of characteristic buckling moment resistances for FTQC C

As seen in the figure, there is a good overall agreement between the results. The analytical method provides a lower resistance at low thicknesses, i.e. high r/t ratios, but becomes progressively unconservative with increasing thickness. The extent of the conservative region increases in general with the length in an irregular pattern. Note that light colours in the plot indicate minor differences between the values. The results for FTQC A and B look similar to those for C, and they are therefore not shown here.

Since the project focuses on buckling in monopiles, and they are typically constructed of cylinders with an r/t ratio between 35 and 65, the error in the analytical method relative to the numerical results is visualised in Figure 5.2 across those ratios for all lengths investigated in the project and for all three standard fabrication tolerance quality classes. The relative error here and later in this chapter is calculated as shown in (5.1). The variation of the relative error is rather irregular. The lowest value is -4.9% observed at $L = 10$ m and $r/t = 65$. The highest value is 6.6% at $L = 15$ m and $r/t = 50$. For lengths between 20 and 35 m, the analytical method provides unconservative results for monopiles regardless of r/t ratio and quality class.

$$\text{Relative error} = \frac{\text{analytical value} - \text{numerical value}}{\text{numerical value}} \tag{5.1}$$

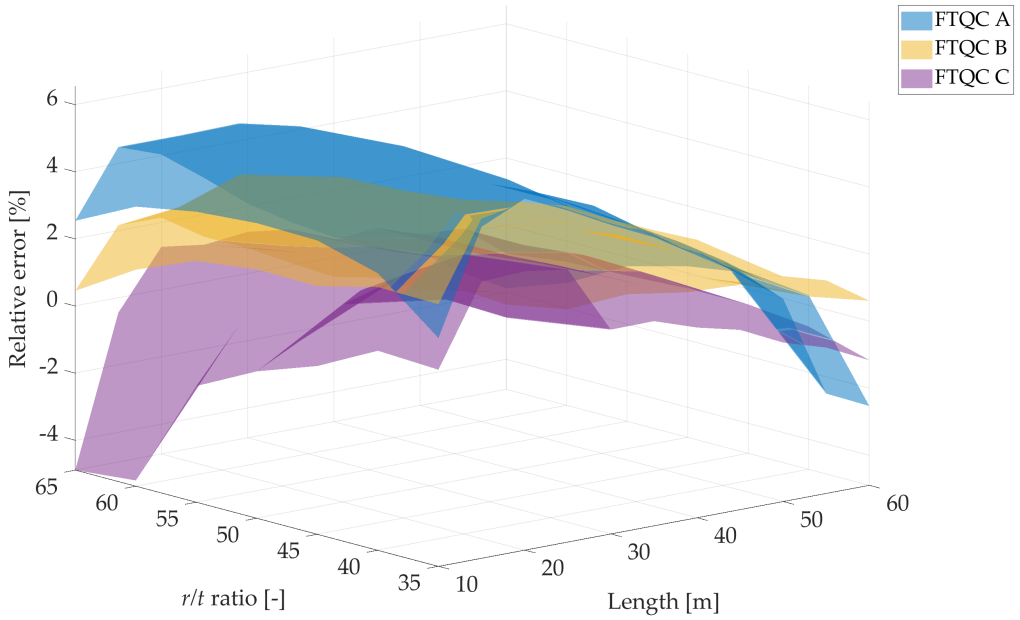

Figure 5.2: Relative error in analytical method for typical monopiles

Based on the presented comparison of characteristic buckling moment resistances, it can be concluded that the analytical method in prEN 1993-1-6:2023 [19] Annex E fits considerably well to typical monopile geometries. In fact, it predicts slightly unconservative resistances for the most common dimensions, although that is presumably accounted for by the applied partial factor. Consequently, it is deemed unnecessary to reformulate most of the expressions for the capacity curve parameters. Focus is directed instead towards the parameters independent of the form of geometric imperfection, i.e. C_m and α_G, as those can be utilised later when investigating cylinders with a limited dimple.

5.2 Linear Elastic Critical Moment

This section provides an assessment and reformulation of the analytically calculated elastic critical moment M_{cr} and includes a brief analysis to investigate whether there are differences between the results for a clamped and a cantilever cylinder.

As mentioned in section 4.3, the analytical expression for the elastic critical moment M_{cr} consists of two contributions, namely the classical elastic critical moment M_{cl} and the parameter C_m which accounts for the restraining effect of the end boundaries. The relation between these parameters is shown in (5.2) as per [21]. It should be noted that in prEN 1993-1-6, $M_{cr} = M_{cl}$, i.e. a conservative choice is made by setting $C_m = 1$. It is in EN 1993-1-6/A1:2017 [23] given that the expression for M_{cr} corresponds to $M_{cr} = C_m M_{cl}$. In the following, the expression from EN 1993-1-6/A1:2017 [23] is used as a basis for better evaluation and reformulation.

$$\begin{aligned} M_{cr} &= C_m M_{cl} \\ M_{cl} &= \frac{\pi}{\sqrt{3(1-\nu^2)}} E r t^2 \\ C_m &= 1 + \frac{4}{\omega^2} \end{aligned} \tag{5.2}$$

Numerically, M_{cr} is determined using an LBA, and the values of M_{cr} for each model are shown in Figure 5.3 as a function of the two input parameters varied in the analyses, namely the length and thickness, along with the corresponding analytical values.

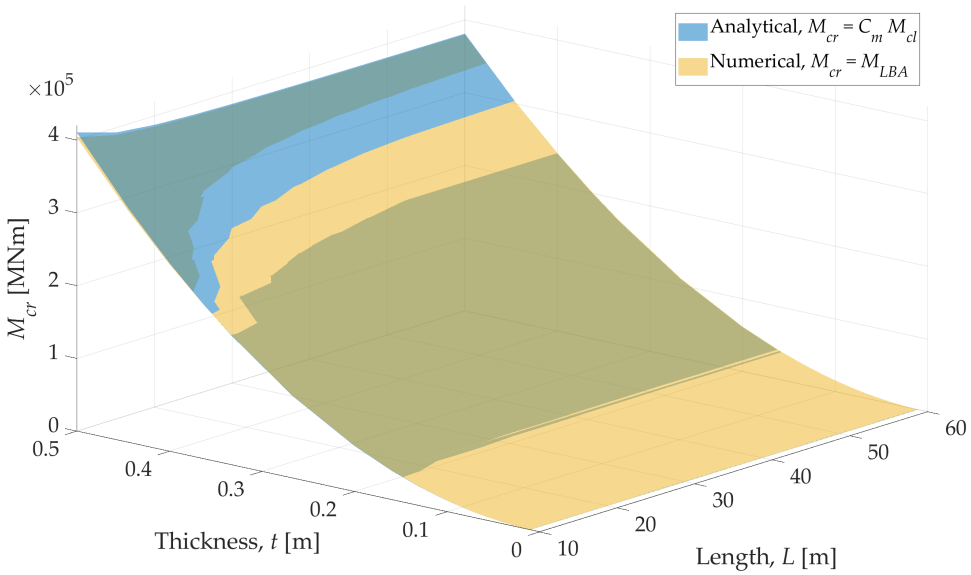

Figure 5.3: Comparison of elastic critical moments

It is observed that the analytical results for M_{cr} are higher than the numerical ones for large thicknesses, i.e. smaller r/t ratios, specifically between 8 and 10. The greatest deviation between the results also occurs at the smaller r/t ratios, as illustrated in Figure 5.4. This is not surprising, as the method in EN 1993-1-6/A1:2017 [23] is valid for $25 \leq r/t \leq 3000$, meaning it cannot be expected to be accurate outside this range.

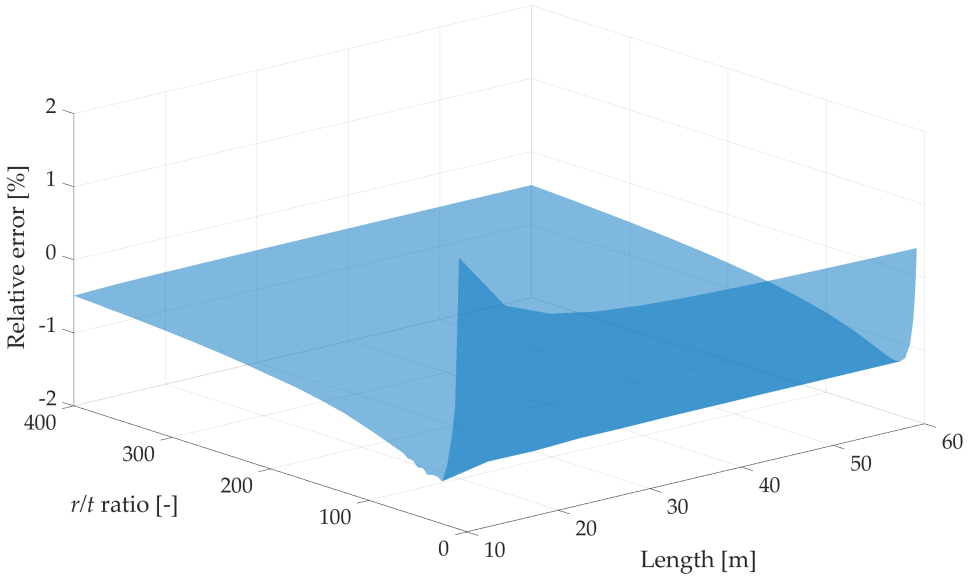

Figure 5.4: Relative error in the analytically calculated elastic critical moments

For $r/t > 10$ the numerical results are slightly higher than the analytical ones, which indicates that the expression for M_{cr} is not precise and may require reformulation to better align with the numerical results. The expression for M_{cl} has a theoretical and historical background, and is assumed to have been determined quite accurately. Instead, attention is directed towards the parameter C_m.

In Figure 5.5, the numerical results are normalised with M_{cl}, i.e. the parameter C_m is shown instead of M_{cr}. The plot clearly shows that there is a deviation between the analytical and numerical values of the parameter C_m, with the numerical values being higher than the analytical ones for $r/t > 10$.

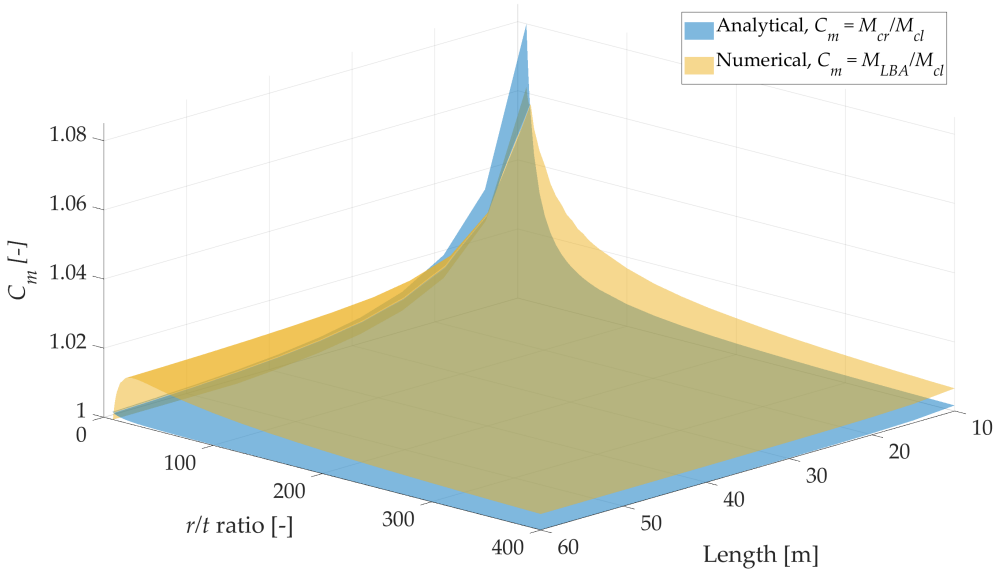

Figure 5.5: Comparison of the parameter C_m

In Figure 5.6, scattered numerical values of the parameter C_m are shown together with the curve from the analytical expression as a function of ω. Note again that for low r/t ratios, the analytical expression does not fit well, and that it is conservative for the higher r/t ratios. Therefore, the upcoming reformulation of the expression for the parameter C_m is carried out by disregarding the low r/t ratios, as they are not realistic geometries for an offshore monopile. The different behaviour that is observed for low r/t ratios are explained in section 2.3.2.

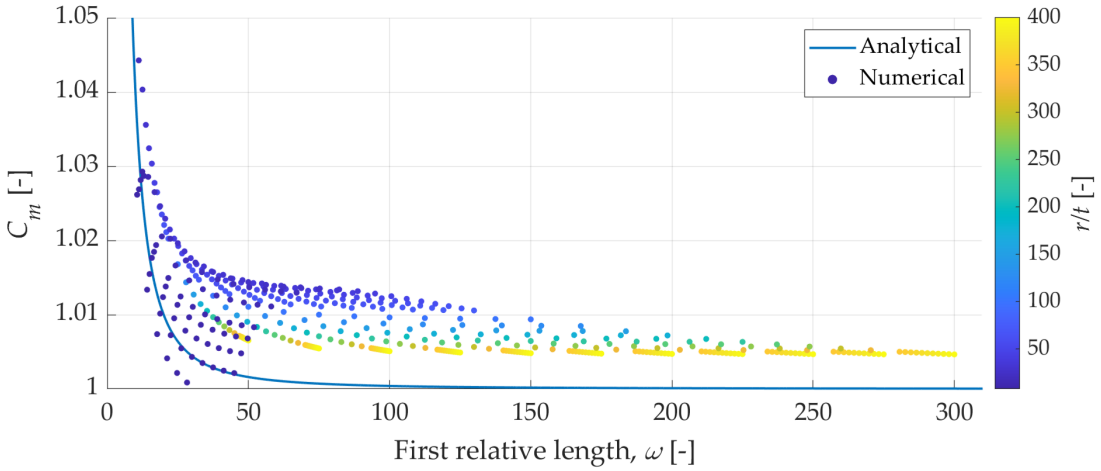

Figure 5.6: C_m for all numerical results with the r/t ratio indicated for each point

The figure above shows that the results are not scattered randomly, but exhibit a clear dependence on both the thickness, i.e. the r/t ratio, and the length. The variation with respect to the length is illustrated in Figure 5.7.

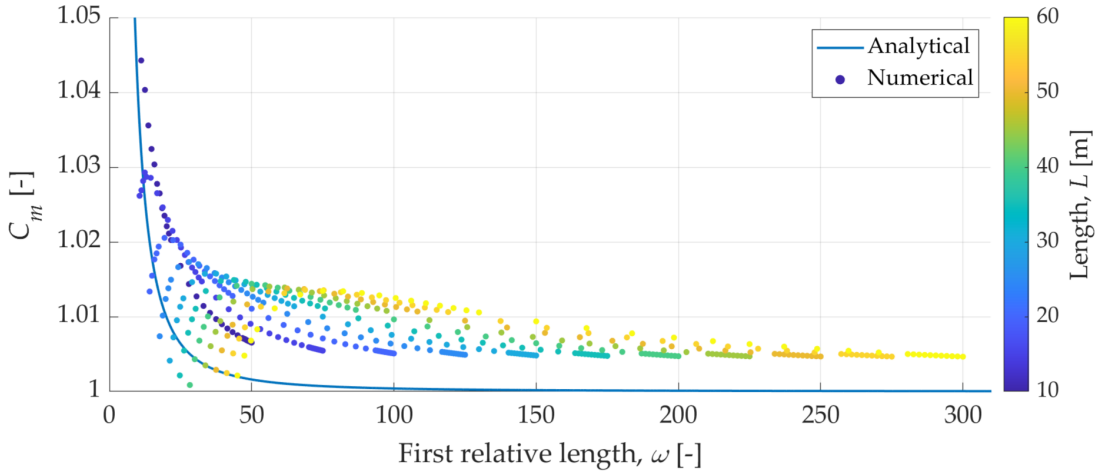

Figure 5.7: C_m for all numerical results with the length indicated for each point

It is decided to reformulate the first term in the expression for C_m so that it explicitly depends on the r/t ratio. In this way, a separate curve can be fitted for each r/t ratio, in contrast to the current expression by Rotter et al. [21], where a single curve is used to fit all the data. The rewritten expression is given in (5.3), where the first term is a power function and the second term remains unchanged.

$$C_m = 1.025 \left(\frac{r}{t}\right)^{-0.0035} + \frac{4}{\omega^2} \qquad \text{for} \quad 35 \leq r/t \leq 400 \tag{5.3}$$

In Figure 5.8, numerical values are presented alongside the curves based on the rewritten expression for selected r/t ratios. The rewritten expression is valid for $r/t \geq 35$. If the expression were to be made valid for $r/t < 35$, it would become too conservative for $r/t \geq 35$, which is undesirable due to the area of interest regarding the realistic geometry of an offshore monopile.

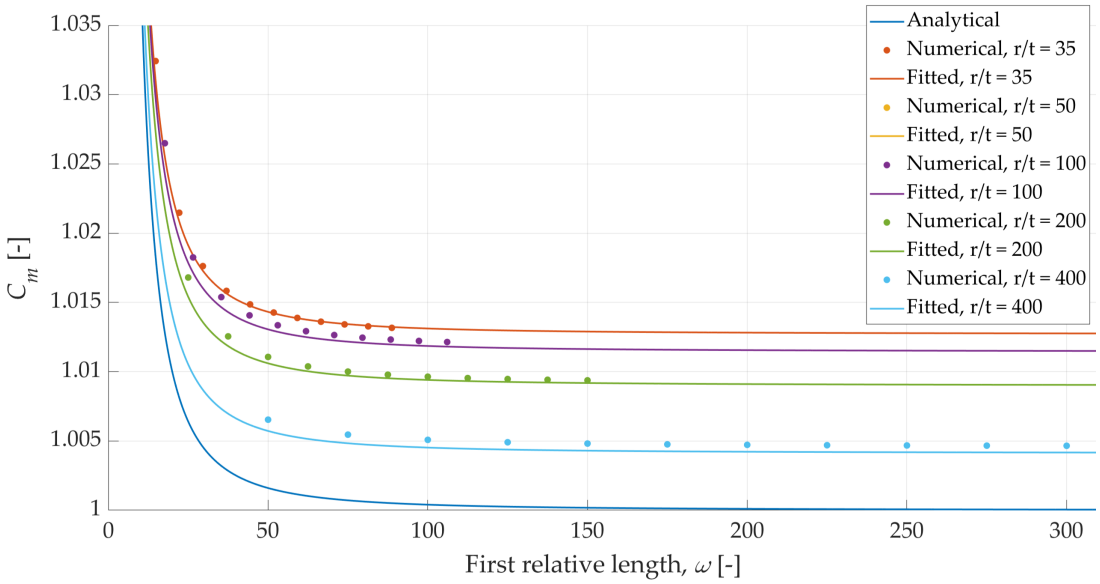

Figure 5.8: Fitted C_m curves for selected r/t ratios

Lastly, a fitted surface is shown together with the numerical results in Figure 5.9. It can be seen that the new expression for C_m provides a much better fit.

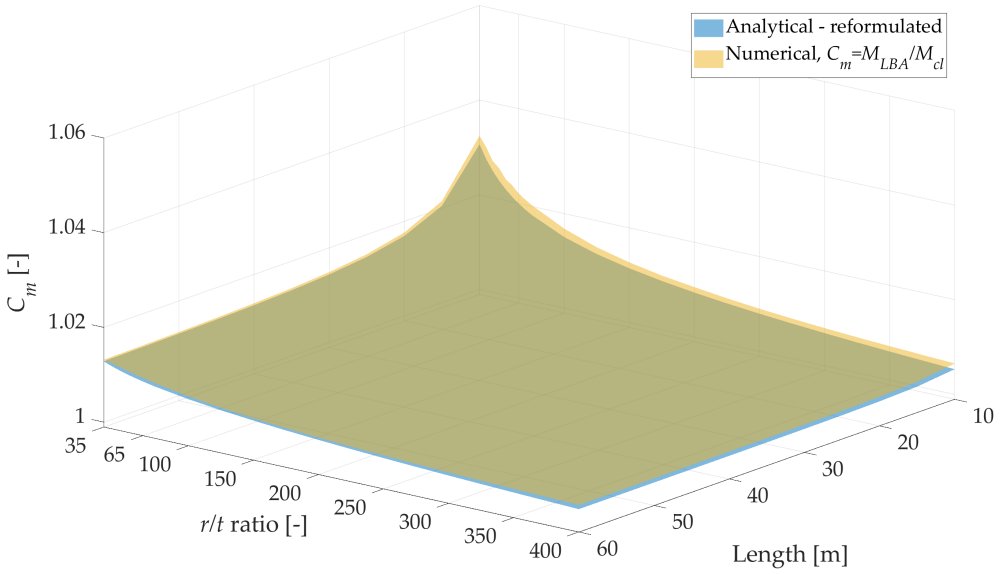

Figure 5.9: Comparison of the paramter C_m

The section concludes with an investigation into whether there are differences between the results for a clamped and a cantilever cylinder. Different geometries are investigated as given in Table 5.1. No difference is observed in the numerical results for M_{cr} regardless of the cylinder's global boundary conditions. Fajuyitan et al. [22] also investigated the effect of global boundary conditions in a cylinder. Specifically, a clamped and a simply-supported cylinder were compared. They found that for around $\omega < 10$, larger differences can be observed in the results. Such differences are not detected in this investigation, probably because the lowest relative length considered is $\omega = 14.7$, corresponding to $L = 10$ m and $r/t = 35$.

Table 5.1: Comparison of results for clamped and cantilever cylinder

Length L [m]	r/t [-]	Global boundary conditions	Analytical M_{cl} [MNm]	Analytical M_{cr} [MNm]	Numerical M_{cr} [MNm]
10	35	Clamped	19 872	20 236	20 517
		Cantilever	–	–	20 517
	400	Clamped	152.1	152.4	153.1
		Cantilever	–	–	153.1
30	35	Clamped	19 872	19 913	20 168
		Cantilever	–	–	20 168
	400	Clamped	152.1	152.1	152.8
		Cantilever	–	–	152.8
60	35	Clamped	19 872	19 883	20 134
		Cantilever	–	–	20 134
	400	Clamped	152.1	152.1	152.8
		Cantilever	–	–	152.8

This means that M_{cr} is not affected by the type of support condition, unless the cylinder is short or thick-walled. It also implies that the parameter C_m is defined independently of any specific support condition. Instead, it accounts for the influence of support conditions on local buckling. When the distance between the supports is small, they provide additional resistance against buckling, hence increasing the critical moment and the value of C_m. As the distance between the supports increases, their influence on local buckling diminishes. In other words, the longer the cylinder, the larger ω becomes, and the smaller the value of C_m, as can be seen from both expression (5.2) and Table 5.1.

5.3 Nonlinear Elastic Critical Moment

The nonlinear elastic critical moment $\alpha_G M_{cr}$ and the corresponding geometric reduction factor α_G can be determined numerically using geometrically nonlinear analysis, GNA. Results from 429 GNAs are presented in Figure 5.10 together with the analytically calculated moment resistances. As seen in the figure, the results are closely aligned for most geometries. The smallest differences are observed at low thicknesses (i.e. high r/t ratios), where the numerical values only slightly exceed the analytical ones, resulting in the visibility of only the light yellow surface in the plot. As thickness

increases or r/t ratio decreases, the difference between the two approaches becomes more pronounced. While numerical results generally remain higher than the analytical ones, an exception occurs at shorter lengths (10 and 15 m), where the discrepancy diminishes beyond a certain thickness, and the analytical values eventually exceed the numerical ones. A similar pattern can be observed when comparing the analytically calculated geometric reduction factor with the normalised numerical results, as shown in Figure 5.11.

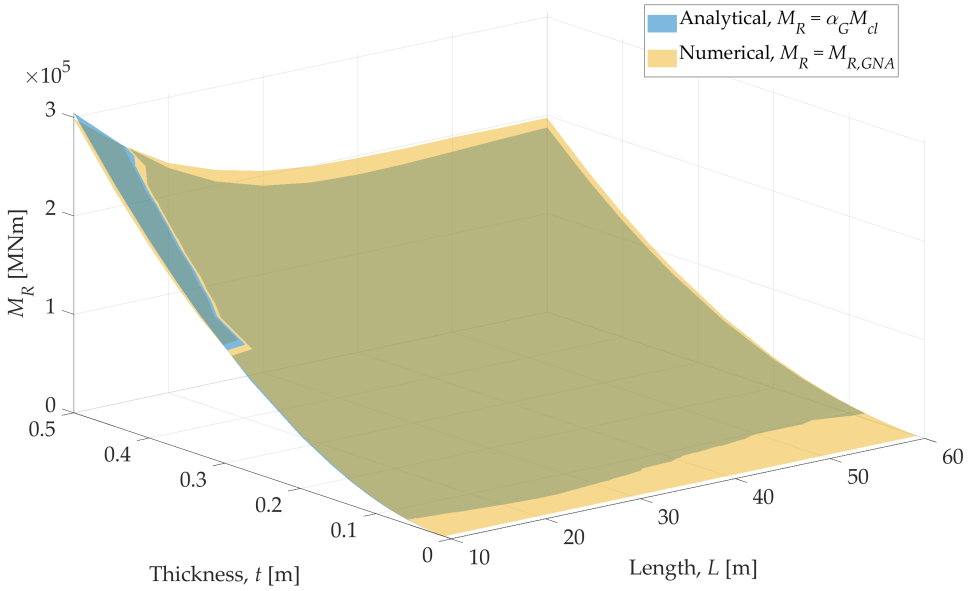

Figure 5.10: Comparison of nonlinear elastic critical moments

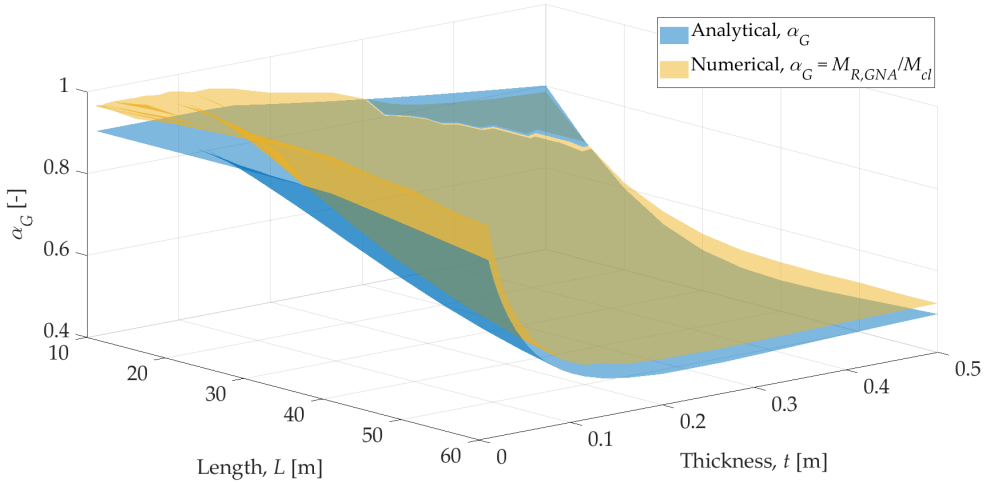

Figure 5.11: Comparison of geometric reduction factors

It should be noted that the analytical moment resistance in Figure 5.10 and the numerical geometric reduction factor in Figure 5.11 are calculated using M_{cl}, since prEN 1993-1-6:2023 [19] applies the simplification of $M_{cr} = M_{cl}$ assuming $C_m = 1.0$. That is a conservative assumption as the actual value of C_m can be higher than unity, as demonstrated previously. By using a more precise value of C_m, the absolute value

of the deviation between the analytical and numerical results decreases, as shown in Figure 5.12. The plot uses analytical values calculated with the current expression for C_m from (5.2) as well as the reformulated one from (5.3). Since the validity of (5.3) is limited to $r/t \geq 35$, lower ratios are excluded from the plot.

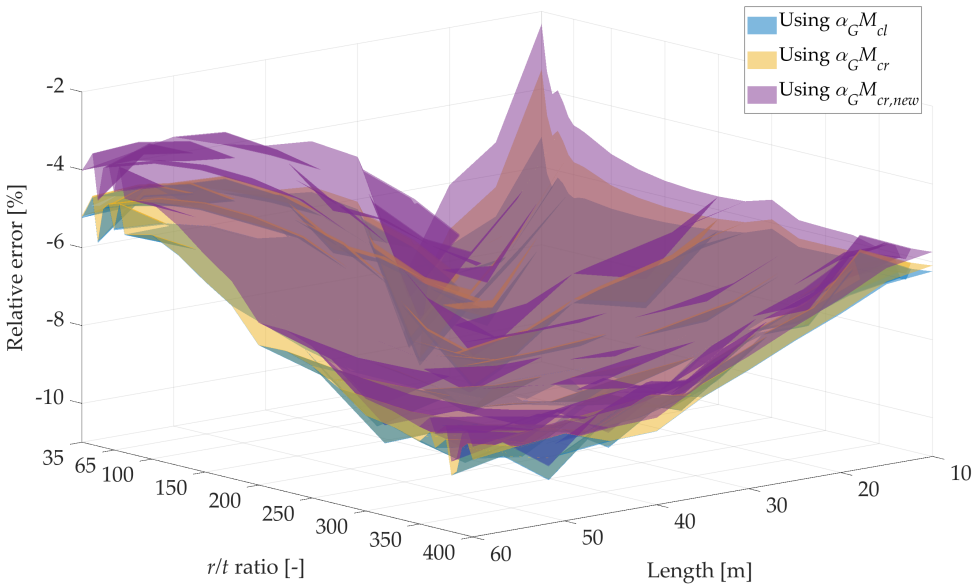

Figure 5.12: Relative error in the analytically calculated nonlinear elastic critical moments

In order to reduce the observed deviations, the analytical expression for the geometric reduction factor α_G needs to be optimised. The current expression from prEN 1993-1-6:2023 [19] is defined as a function of a single variable, the second relative length Ω, as presented in (5.4), and contains a smooth transition to an upper limit of 0.9 at $\Omega = 0.5$. That point marks the boundary between medium-length and long cylinders under uniform global bending as defined in prEN 1993-1-6, or the medium and transitional domains as more formally identified by Rotter et al. [21] and Wang et al. [28], among others.

$$\alpha_G = \begin{cases} 0.9 & \text{for} \quad \Omega < 0.5 \\ 0.5 + (0.38 \sin(0.85\Omega) + 0.48 \cos(0.85\Omega)) e^{-0.8\Omega} & \text{for} \quad \Omega \geq 0.5 \end{cases} \tag{5.4}$$

Another set of analytical expressions for α_G was previously presented by Rotter et al. [21], setting the upper limit in the medium domain slightly higher and explicitly defining a lower limit in the long domain, since the expression does not settle on that value.

$$\alpha_G = \begin{cases} 0.92 & \text{for} \quad 8.6 \leq \omega \text{ and } \Omega < 0.5 \\ 1.07 \dfrac{1 - 0.22\Omega + 0.061\Omega^{2.94}}{1 + 0.12\Omega^{2.94}} & \text{for} \quad 0.5 \leq \Omega < 7.0 \\ 0.516 & \text{for} \quad \Omega \geq 7.0 \end{cases} \tag{5.5}$$

Both sets of expressions are visualised in Figure 5.13 together with the numerical results from GNA normalised with results from LBA. As seen in the figure, the

numerical values are located within two of the four formal domains: the medium and the transitional. It should be noted that the range of validity of both analytical expressions is limited to r/t ratios of at least 50, which can be justified by the scatter of the dark blue data points corresponding to lower ratios.

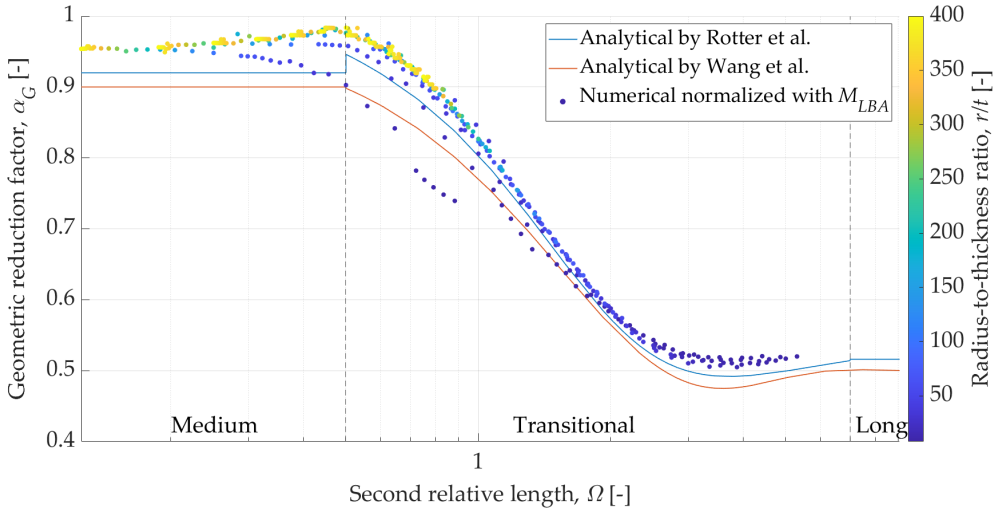

Figure 5.13: Geometric reduction factor as a function of Ω

In the medium domain, the data points are supposed to lie on a wavy curve with a shape of connected festoons as first identified by Seide and Weingarten [46], and later also demonstrated by Rotter et al. [21]. However, due to the limited number of combinations of lengths and thicknesses investigated in the project, only a few flattened festoons are visible in Figure 5.14, primarily for the lower r/t ratios. It can also be seen in the figure that the boundary between the medium and transitional domains defined in the current analytical expressions at $\Omega = 0.5$ is appropriate to r/t ratios of at least 50, but it shifts to higher Ω values as r/t decreases. Based on Figure 5.14, it can be placed at $\Omega \approx 1.2$ for $r/t = 35$ and at $\Omega \approx 1.4$ for $r/t = 25$, although the density of the data is insufficient for more accurate predictions.

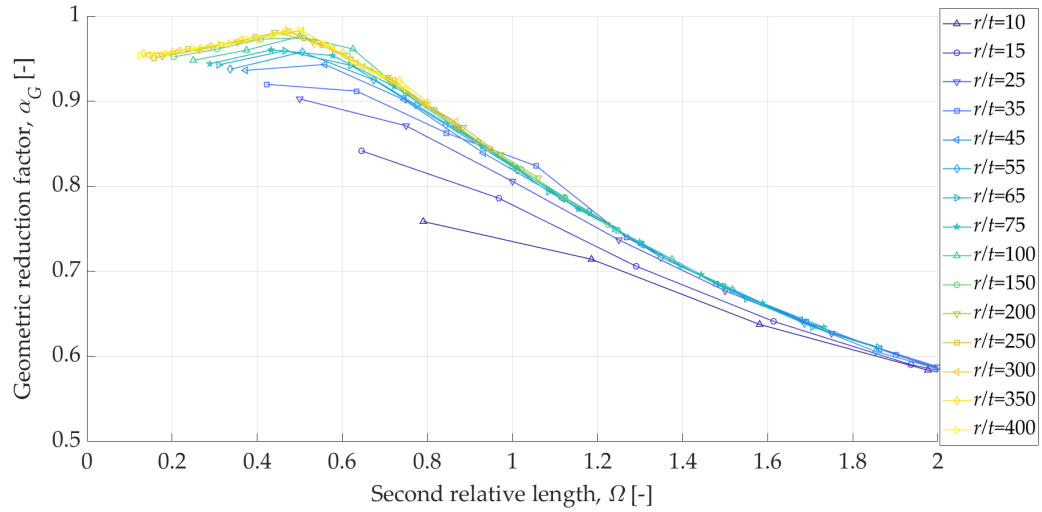

Figure 5.14: Numerically calculated geometric reduction factor in the medium domain

In the transitional domain, the data points are expected to lie on a single line according to Rotter et al. [21]. When considering the above statement about the location of the domain's lower boundary, it becomes apparent that the numerical values in Figure 5.13 do more or less lie on a single line.

Based on the generated numerical data and utilising the Curve Fitting Toolbox [47] in the software MATLAB [48], an attempt is made to optimise the current analytical expression, focusing on typical monopile geometries, i.e. $35 \leq r/t \leq 65$. The optimisation results in a reformulation as shown in (5.6), inspired by the expression of Wang et al. [28], which is also used in prEN 1993-1-6. Similarly to the reformulated expression of C_m, the validity of (5.6) is limited to $r/t \geq 35$. The goodness of fit of the new expression is visualised in Figure 5.15.

$$\alpha_G = \begin{cases} 0.91 & \text{for } \Omega \leq 0.75 \\ 0.507 + (1.52\sin(0.85\Omega) + 0.39\cos(0.85\Omega))e^{-1.47\Omega} & \text{for } \Omega > 0.75 \end{cases} \tag{5.6}$$

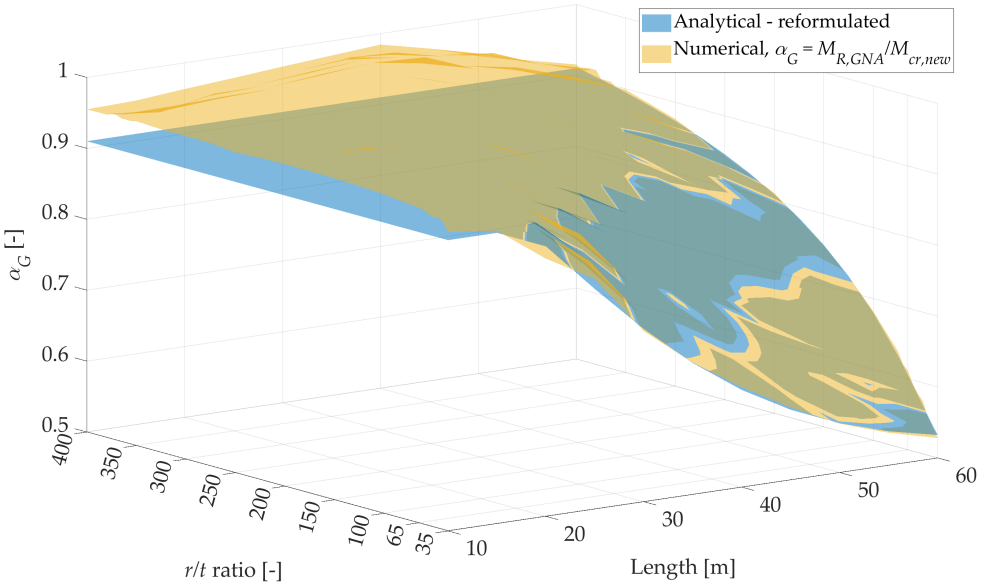

Figure 5.15: Comparison of geometric reduction factors

In contrast to the existing ones, the reformulated expression is not fully conservative as it slightly overestimates the geometric reduction factor for certain cylinders by approximately 2% at most. On the other hand, it also reduces the overall conservatism, changing the minimum value of the relative error from ca. -10% to ca. -5% for typical monopile geometries. The reformulated expression is visualised together with the current ones and the numerical results in Figure 5.16.

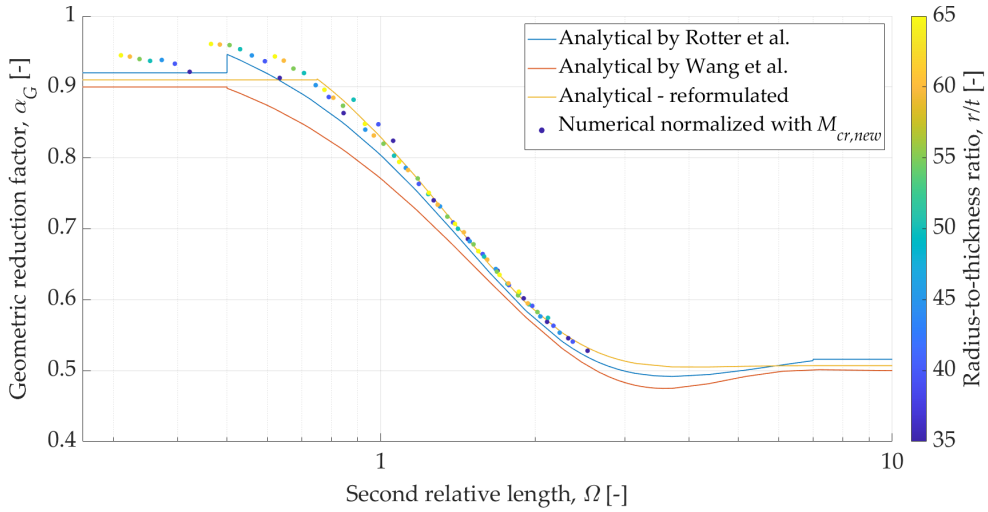

Figure 5.16: Geometric reduction factor for typical monopiles

5.4 Nonlinear Elastic Imperfect Critical Moment

The nonlinear elastic imperfect critical moment corresponds to αM_{cr}, where $\alpha = \alpha_G \alpha_I$. By introducing imperfections into the geometry, αM_{cr} can be determined in a GNIA. From there, α_I can be determined numerically by dividing αM_{cr} with the nonlinear elastic critical moment $\alpha_G M_{cr}$ extracted from a GNA for the same geometry. The imperfection reduction factor is thus determined numerically as $\alpha_I = M_{R,GNIA}/M_{R,GNA}$. Analytically, the expression shown in (5.7) is used.

$$\alpha_I = \frac{1}{1 + \left(0.7 + \frac{1.05}{0.4\Omega^{2.8}}\right)\left(\frac{\delta_0}{t}\right)^{0.7}} \tag{5.7}$$

The analytical and numerical values of $M_R = \alpha M_{cr}$ are shown in Figure 5.17 for FTQC C. The numerical values are higher than the analytical ones for all investigated geometries, which indicates that the analytical estimation of αM_{cr} is conservative.

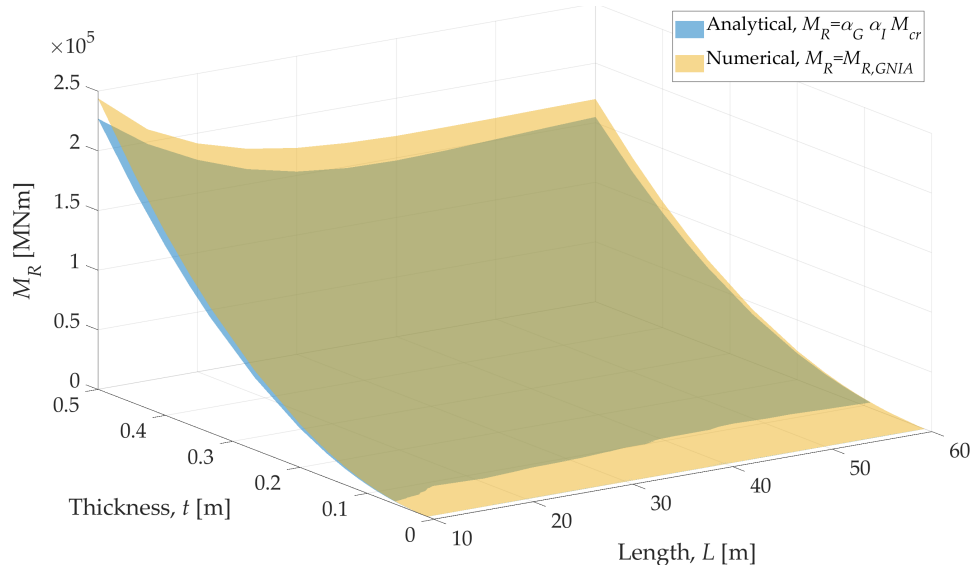

Figure 5.17: Comparison of nonlinear elastic imperfect critical moments for FTQC C

However, the parameter α_I is not estimated conservatively for all the geometries studied, as shown in Figure 5.18 for FTQC C. It can be seen that for thicknesses less than approximately 0.1 m, the analytical values of α_I become higher than the numerical ones. In the method given in prEN 1993-1-6, the value of α_G is underestimated, as described in section 5.3, which can lead to higher α_I values. This can easily be seen by considering the relationship shown in (5.8).

$$\alpha_I = \frac{\alpha M_{cr}}{\alpha_G M_{cr}} \tag{5.8}$$

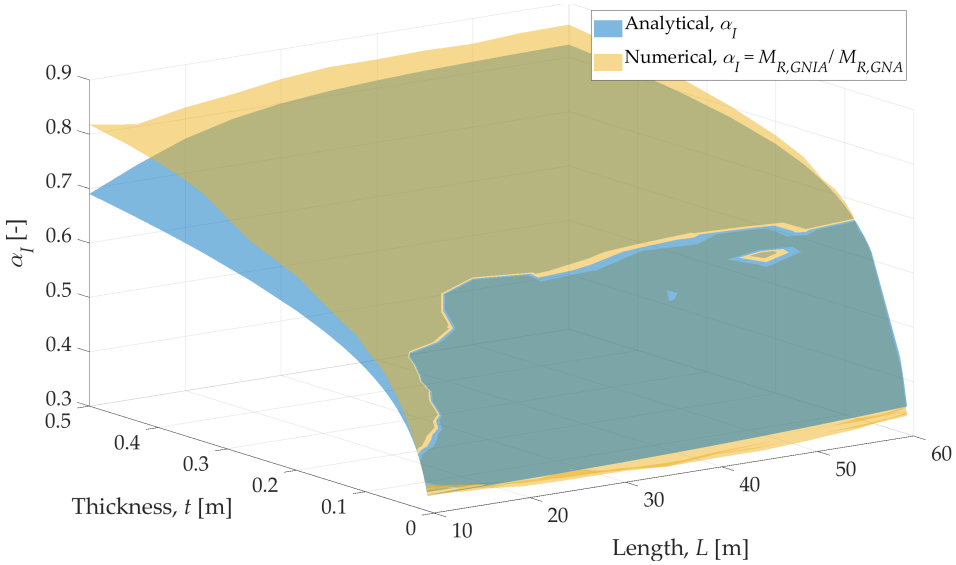

Figure 5.18: Comparison of imperfection reduction factors for FTQC C

It is observed that the relative error between the analytical and numerical results decreases as the imperfection amplitude δ_0 is reduced. The largest absolute relative error is 13.0% for FTQC A and 15.7% for FTQC C. The relative error for all geometries are shown in Figure 5.19.

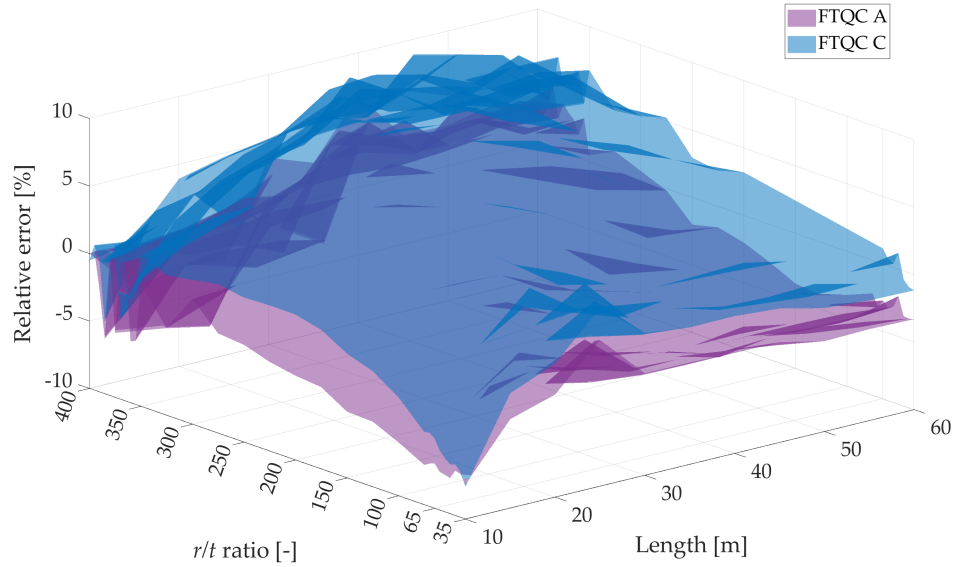

Figure 5.19: Relative error of the analytically calculated imperfection reduction factors

There are considerable deviations between the analytical and numerical values of α_I. The deviation can be reduced by reformulating the expression for α_I. However, reducing the conservatism of the nonlinear elastic imperfect critical moment αM_{cr} is not appropriate, given that the method is already unconservative for typical offshore monopile geometries, as described in section 5.1.

5.5 Plastic Moment Resistance

The plastic moment resistance M_{pl} is determined numerically using MNA and analytically using the expression in (5.9) valid for shells.

$$M_{pl} = 4r^2 t f_{yk} \tag{5.9}$$

The numerical results for the 48 different geometries, which are presented in section 3.2.3, together with the corresponding analytical values are shown in Figure 5.20.

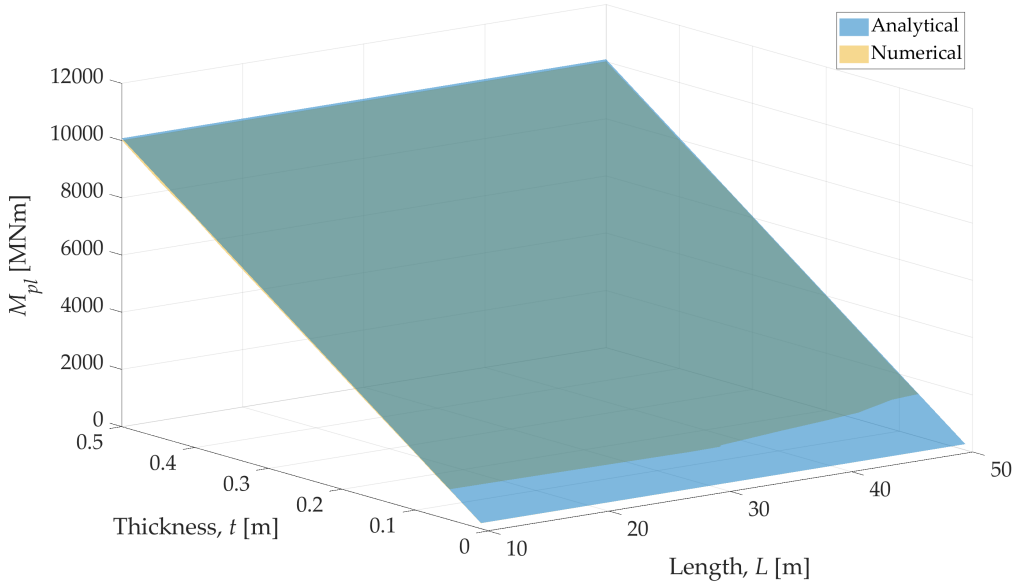

Figure 5.20: Comparison of plastic moment resistances

All numerical results are slightly below the analytical values. The relative error between the analytical and numerical values is shown in Figure 5.21. The maximum absolute relative error reaches a value of 3.0%.

A possible explanation for the deviation might be the use of shell elements, as their implementation may not allow the full plastic cross-sectional capacity to be reached. Since the analytical expression for M_{pl} is well established, there is no need to reformulate it.

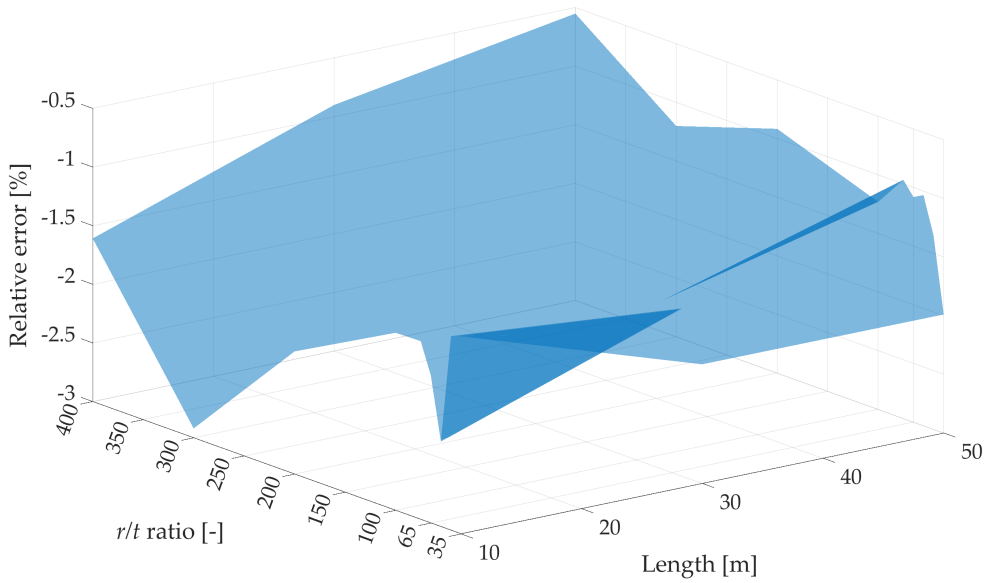

Figure 5.21: Relative error in the analytically calculated plastic moment resistances

According to the expression in (5.9), the plastic moment resistance M_{pl} depends on the cross-sectional parameters and is independent of the cylinder length. To verify that this also holds for the numerical results, Figure 5.22 can be considered. In Figure 5.22, it can be seen that M_{pl} has the same value for each thickness across all lengths.

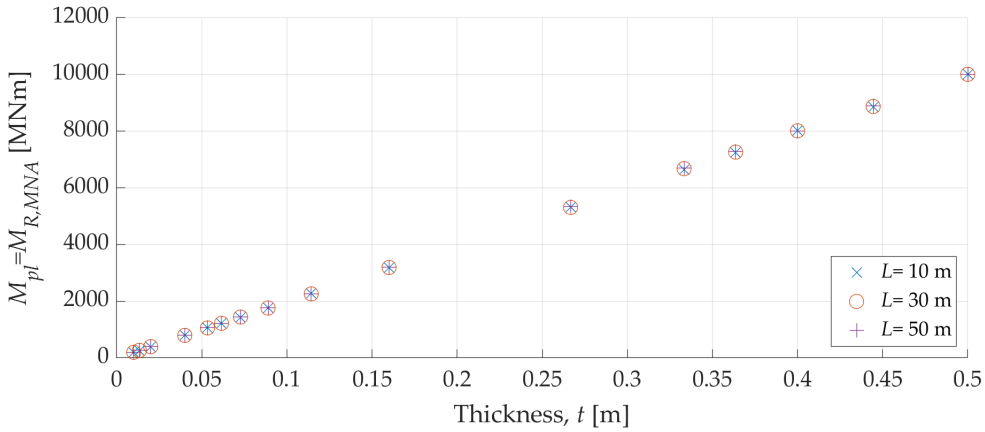

Figure 5.22: Plastic moment resistances for different lengths

5.6 Reduced Plastic Moment Resistance

The plastic moment resistance M_{pl} is used as a normalising parameter and serves to determine the relative slenderness of the structure; recall that $\overline{\lambda} = \sqrt{M_{pl}/M_{cr}}$. As described earlier in section 2.4.3, imperfections can negatively affect the plastic moment resistance of cylinders subjected to global bending. This leads to the use of a reduced plastic moment resistance $M_{pl,I}$ as the normalising parameter instead. It is defined in (5.10), where M_{pl} is reduced by the parameter κ.

$$M_{pl,I} = \kappa M_{pl}$$
$$\kappa = 0.2 + \frac{0.8}{1 + 0.23\,(\delta_0/t)^2} \tag{5.10}$$

Figure 5.23 shows numerical results corresponding to the reduced plastic moment resistance for all three fabrication tolerance quality classes. It is observed that the surfaces follow the expected order corresponding to each FTQC, with FTQC A having the highest resistances and FTQC C the lowest.

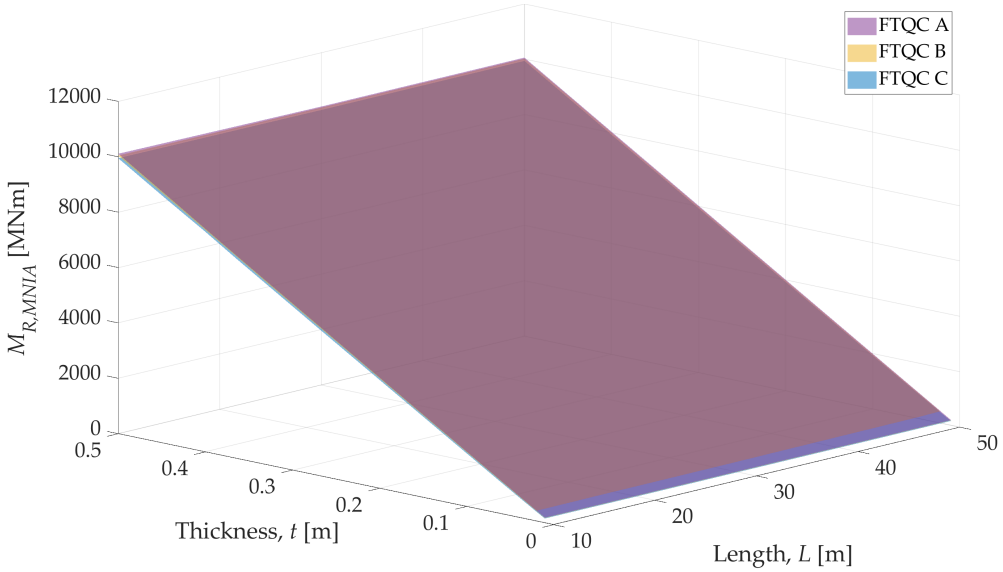

Figure 5.23: Comparison of numerical results for all FTQC

Figure 5.24 shows the numerical results alongside the corresponding analytical results for FTQC C. A slight discrepancy can be observed between the results, with the analytical values being higher than the numerical ones.

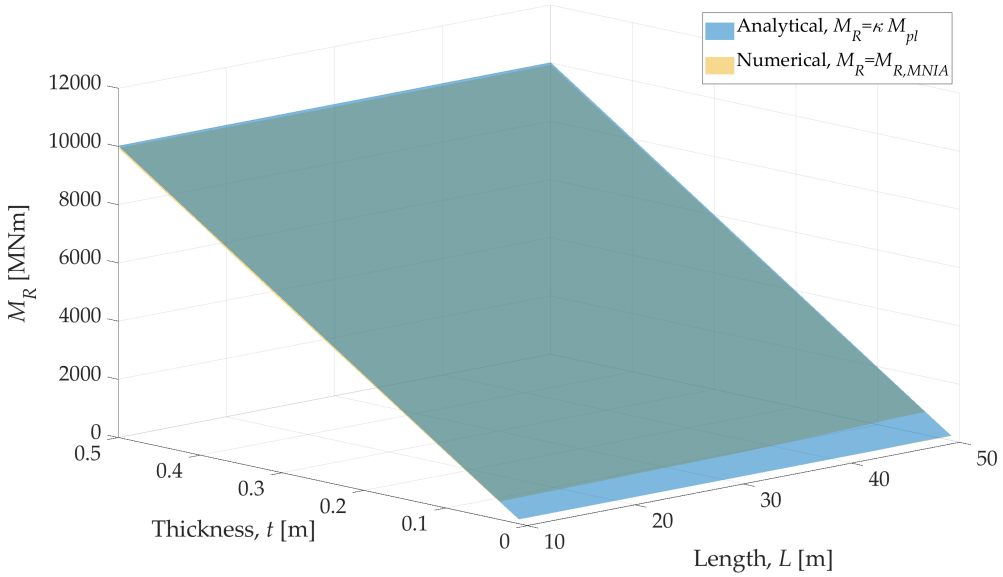

Figure 5.24: Comparison of reduced plastic moment resistances for FTQC C

The same trend is seen for FTQC A and B, although the deviations are smaller, as illustrated in Figure 5.25. The maximal relative error is 1.9% for FTQC A, 2.2% for FTQC B and 2.4% for FTQC C. Since FTQC C exhibits the largest deviation, the following figures are presented for this particular class.

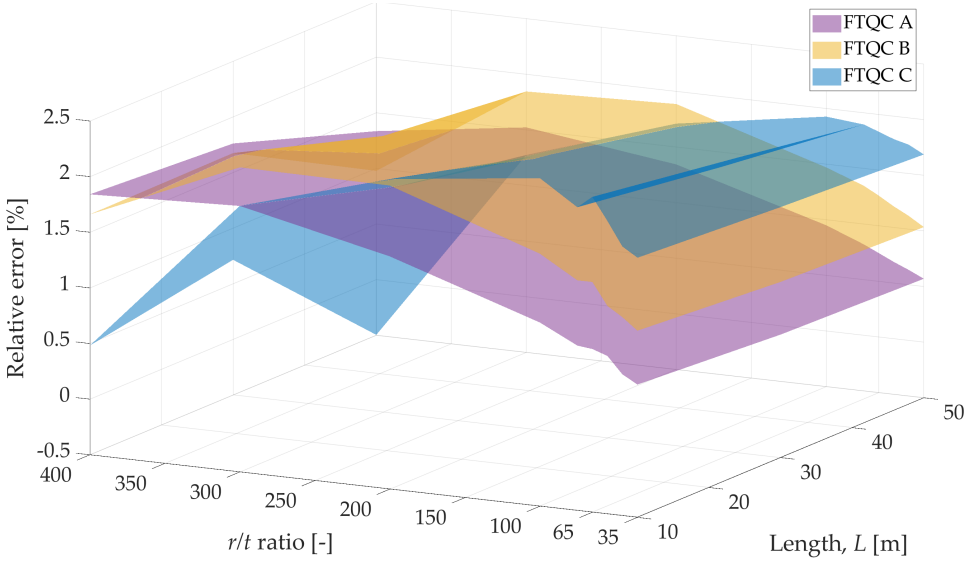

Figure 5.25: Relative error in the analytically calculated κ for all FTQC

It should be noted that the values of $M_{pl,I}$ may contain minor inaccuracies, consistent with the trend observed in MNA. The analytical values are assumed to represent the true values as discussed earlier. As the maximum relative error is 3%, no corrective measures are applied.

In Figure 5.26, the variation of the analytical and numerical values of κ with respect to thickness and length is shown. It is again observed that the analytical values are higher than the numerical ones, which means that the expression for κ in prEN 1993-1-6 [19] is unconservative.

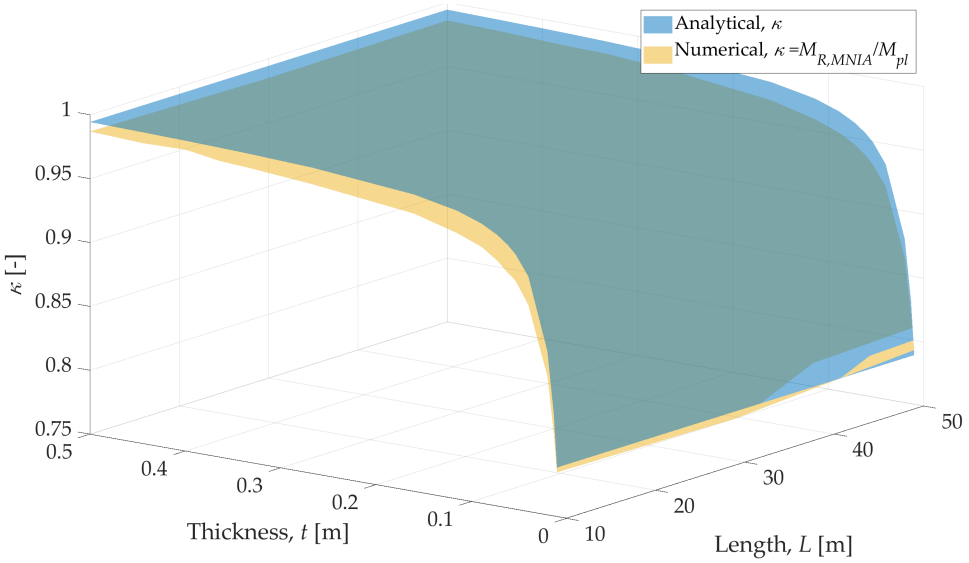

Figure 5.26: Comparison of the parameter κ based on prEN 1993-1-6

As explained in section 4.3, the expression for κ in prEN 1993-1-6, shown in (5.10), is a simplified version of the original formulation derived by Wang et al. [28], which is valid for $r/t \geq 100$. Three expressions for κ were developed by Wang et al. [28] depending on the r/t ratio, as shown earlier in (4.13)–(4.15). Figure 5.27 visualises κ as determined according to Wang et al. [28]. They are slightly more conservative for larger thicknesses, as the analytical results lie below the numerical ones.

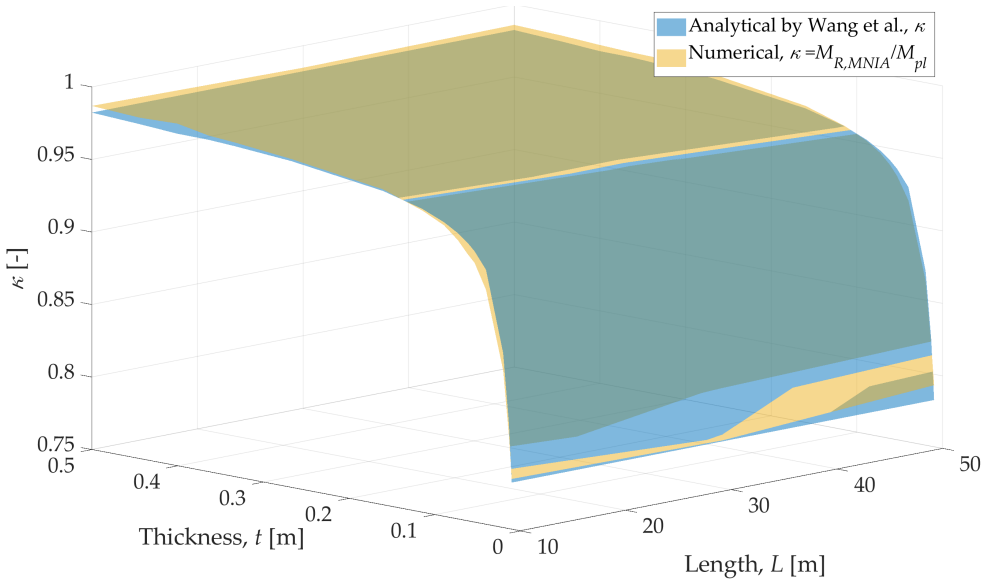

Figure 5.27: Comparison of the parameter κ based on Wang et al. [28]

The corresponding relative errors for all FTQC are presented in Figure 5.28. As expected, they are lower than those in Figure 5.25, where the κ values were calculated using the expression provided in prEN 1993-1-6. The maximum relative error is 1.5% for FTQC C, 1.3% for FTQC B and 1.0% for FTQC A. Since there already exist accurate and well-established expressions for κ there is no reason to perform a reformulation.

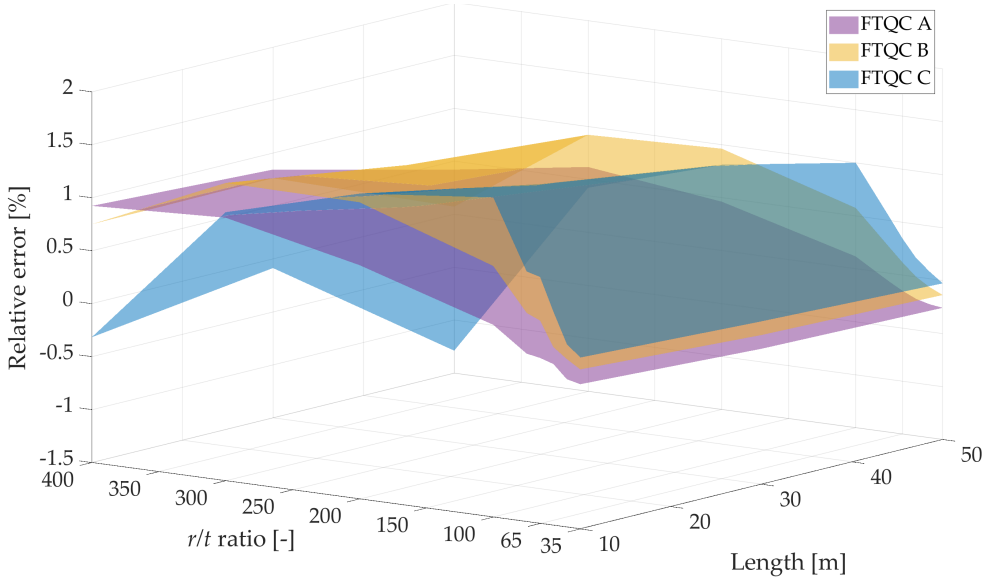

Figure 5.28: Relative error in the analytically calculated κ based on Wang et al. [28]

5.7 Perfect Characteristic Buckling Moment

The perfect characteristic buckling moment $M_{Rk,perfect}$ is determined numerically using GMNA. Analytically, the method provided in prEN 1993-1-6 is not derived in such a way that $M_{Rk,perfect}$ can be determined directly. To determine $M_{Rk,perfect}$ analytically in this project, the method is applied with the imperfection amplitude $\delta_0 = 0$. Reference is made to appendix A, where the procedure is described in detail. The analytical and numerical results are shown in Figure 5.29. In most parts of the plot, the analytical values are higher than the numerical ones. However, for geometries with smaller thicknesses and larger lengths, the numerical results exceed the analytical values. A similarity can be observed between Figure 5.29 and Figure 5.1, which presents the results for GMNIA FTQC C, as both show that the numerical results exceed the analytical values in approximately the same area. The relative error in the analytical results is shown in Figure 5.30, with the extremes being 15.7% and -9.4%. The relative error becomes quite large at smaller thicknesses. These large errors are not surprising, as the analytical method is not based on the assumption $\delta_0 = 0$. Moreover, the GMNA analysis type is not used to derive any parameters or resistances in the method.

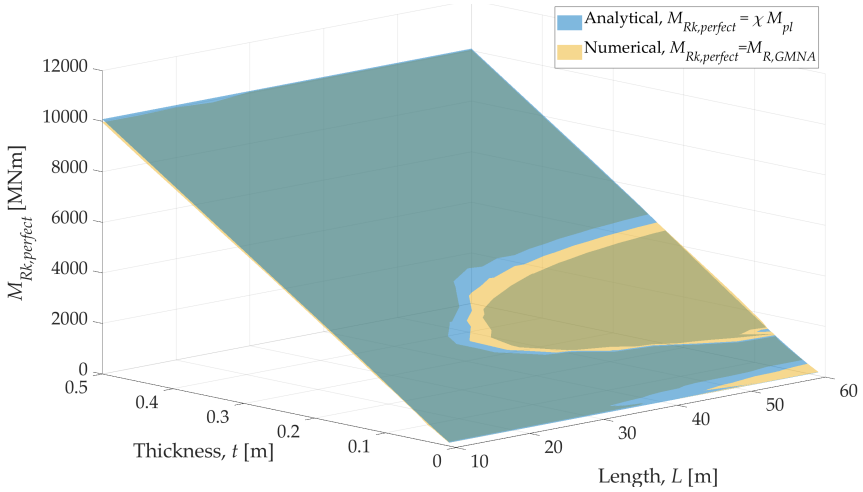

Figure 5.29: Comparison of perfect characteristic buckling resistances

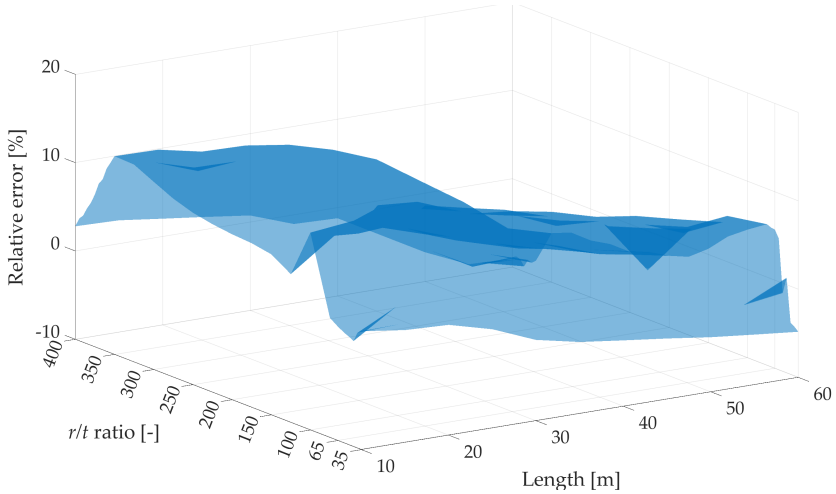

Figure 5.30: Relative error in the analytically calculated perfect char. buckling resistances

5.8 Overall Assessment

This section concludes the assessment of the analytical buckling verification method given in prEN 1993-1-6:2023 [19] by connecting the numerical results from the different analysis types in capacity curves and comparing them with different analytical methods. Moreover, the influence of the static system on the bending moment resistances is evaluated for selected geometries to investigate a possible extension of the method's validity.

Three analytical capacity curves are shown in Figure 5.31 together with numerical results from GNIA, MNIA and GMNIA for $L = 10$, 30 and 50 m for FTQC A. It should be noted that each of the three analytical curves corresponds to a single value of Ω. With the geometries studied in the project, a maximum of three models share the same Ω value, which explains the scatter of the results. Nonetheless, there is good agreement between the results from the different analysis types. However, this issue prevents the optimisation of the method as a whole, as it is not possible to determine the range boundary values λ_0, β, η_0 and η_p without a continuous capacity curve. While individual capacity curve parameters can still be optimised, there is no guarantee that they will align with the existing expressions for the range boundary values.

Figure 5.31 can be compared to the sketch of the capacity curve defined by the different analysis types in Figure 3.3. Note that the numerical results are normalised using the analytical $M_{pl,I}$. Furthermore, the boundaries for the elastic, plastic and elastic-plastic regions are set corresponding to the curve for $\Omega = 2$, although different boundary values apply for each curve.

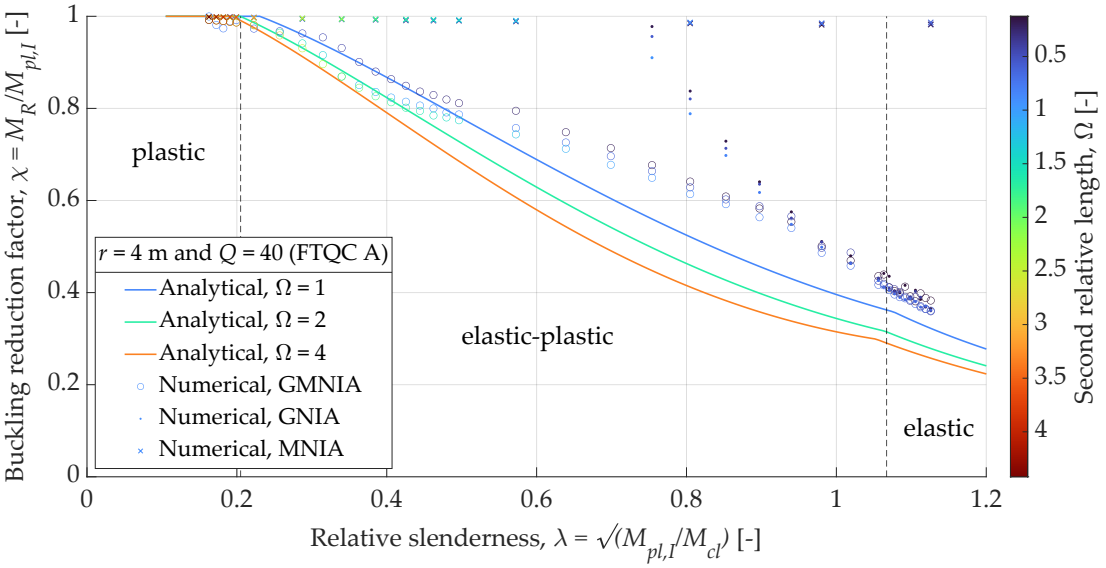

Figure 5.31: Capacity curve for FTQC A

The GNIA results are expected to follow the GMNIA results in the elastic range, as can be observed around $\overline{\lambda} = 1.1$. In the elastic-plastic range, the GNIA data points appear to form three curves corresponding to the three selected lengths, and they all lie above the GMNIA results. It should be noted that referring to them as continuous

curves is not entirely accurate, since the data points cannot be directly connected due to differing Ω values. Still, a tendency can be observed for points with Ω values that lie close to each other — for example, the dark blue ones, which fall approximately within the range $0.125 < \Omega < 0.5$.

The results obtained from MNIA form an approximately horizontal line near $\chi = 1$. The small deviation might be due to the fact that the numerical values of $M_{pl,I}$ are not exact, as discussed in section 5.6. These numerical values are smaller than the analytical ones, which explains why the values of χ are slightly less than 1.

Three analytical capacity curves are plotted for $\Omega = 1$, 2 and 5 to provide a basis for comparison with the numerical results from GMNIA. In reality, only the numerical results corresponding to geometries with the specified Ω values are expected to lie on these curves. Nevertheless, certain trends can still be identified from the capacity curve. The analytical method exhibits both conservative and unconservative behaviour in different parts of the elastic-plastic region. For example, at $\overline{\lambda} \approx 0.5$ to 1.1, the method is conservative. For smaller values of $\overline{\lambda}$, the analytical method becomes unconservative. Note that the relative slenderness for typical monopiles is between approximately 0.34 and 0.46 for $f_y = 315$ MPa. The results presented in section 5.1 indicate that the analytical method is unconservative for monopiles, a trend that is also observed in the capacity curve.

Previously, in Figure 2.30, it was shown how the shape of the curve in the elastic-plastic region depends on whether the value of η is greater than, less than or equal to 1. For $\eta = 1$ the curve is a straight line, $\eta < 1$ produces a convex curve, and $\eta > 1$ results in a concave curve. However, as observed in Figure 5.31, the results from GMNIA in the elastic-plastic region do not form a straight line, nor do they consistently follow a concave or convex shape. This is because the value of η varies throughout the region and is not constant, as could be interpreted based on Figure 2.30. What can be observed more precisely is that the numerical results form a combination of convex and concave curves throughout the elastic-plastic region. This possibly indicates that the value of η needs to be adjusted so that it matches the numerical results better.

5.8.1 Comparison with Other Analytical Methods

In Figure 5.32, the results from GMNIA are compared with three analytical methods, namely those presented in prEN 1993-1-6:2023 Annex D and E, and the currently valid one in EN 1993-1-6/A1:2017 Annex E. The methods are described and compared in section 2.4.3. The analytical capacity curves are all shown for $\Omega = 1$ and to enable the comparison of the three methods, M_{pl} is used as reference resistance instead of $M_{pl,I}$. It is observed that all three methods are unconservative in the region that is valid for monopiles.

The method in prEN 1993-1-6:2023 Annex E fits better with the numerical results in the elastic region, however, it is actually more conservative than the other methods in a large part of the elastic-plastic region. EN 1993-1-6 states that the stress-based method in Annex D is conservative if applied to relatively thick-walled cylinders with certain geometries and loading conditions. This statement holds only if the buckling stress $\sigma_{x,Rk}$ is converted to a buckling moment resistance M_{Rk} using the elastic section

modulus W_{el} in the elastic-plastic region as well, as shown in Figure 5.32. A more precise value of M_{Rk} in that region can be calculated with the elastic-plastic section modulus W_{ep}, found by linear interpolation between the elastic and plastic section moduli W_{el} and W_{pl} using the relative slenderness $\overline{\lambda}$. In that way, the fit is improved and the method is no longer overly conservative. The buckling moment resistance is calculated as per (5.11).

$$M_{Rk} = \sigma_{x,Rk} W \tag{5.11}$$

The χ values determined using the currently valid method given in EN 1993-1-6/A1:2017 Annex E appear to be between the χ values from the other two methods in the elastic region and a part of the elastic-plastic region. This means that the current method in Annex E is less conservative than the proposed one in the elastic-plastic region for $\overline{\lambda}$ values larger than approximately 0.5. However, the method appears to be highly unconservative at the beginning of the elastic-plastic region, which is something that has been adjusted in the proposed method.

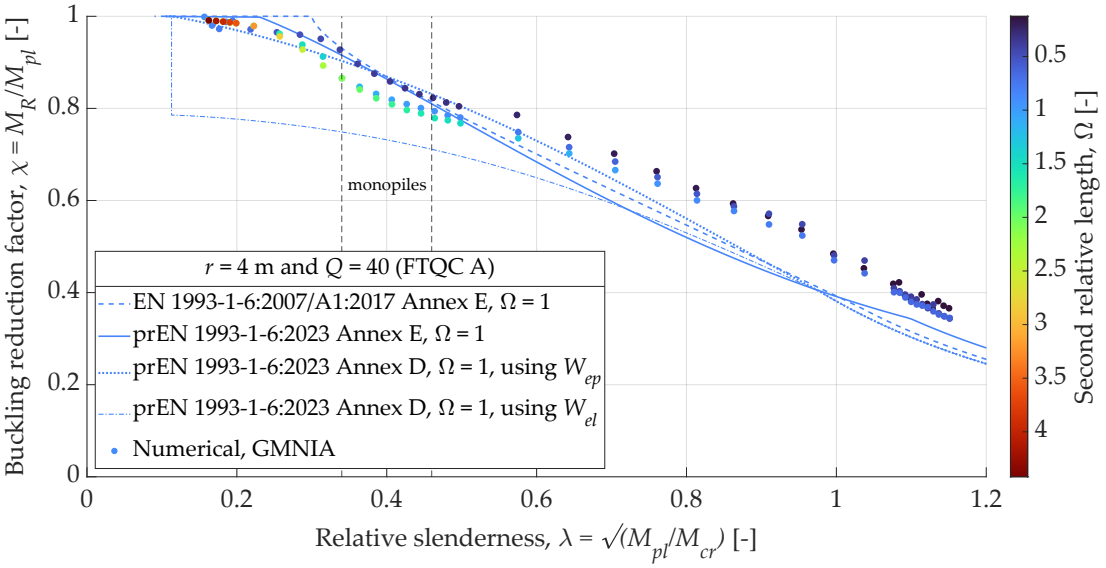

Figure 5.32: Capacity curve for FTQC A

It should be noted that the new expressions for the parameters C_m and α_G are not used in the analytical capacity curves, as they would become even more unconservative. Instead, the new expressions can possibly be used to make the analytical method fit better with numerical results for models with a limited dimple in the next chapter.

The section concludes with a recommendation to use the method in prEN 1993-1-6:2023 Annex E for monopiles with the assumptions mentioned in the introduction of this chapter, as it is the least unconservative and provides the closest fit to the numerical results. Nevertheless, care should be taken when applying the method to avoid overestimating the true capacity, especially for $r/t < 50$.

5.8.2 Effect of Supports

The difference between the characteristic buckling resistance M_{Rk} for a clamped cylinder, as assumed in EN 1993-1-6, and a cantilever cylinder is of particular interest,

as it raises the question of whether the method could be extended to cover other types of global boundary conditions. A selection of geometries is examined for FTQC A, as shown in Table 5.2.

Table 5.2: M_{Rk} for different support condition (FTQC A)

Length L [m]	r/t [-]	Global boundary conditions	Numerical M_{Rk} [MNm]	Difference
10	35	Clamped Cantilever	2 119 2 137	0.8%
	400	Clamped Cantilever	75.8 73.8	-2.7%
30	35	Clamped Cantilever	1 996 1 994	-0.1%
	400	Clamped Cantilever	73.5 69.3	-5.7%
60	35	Clamped Cantilever	2 002 2 049	2.3%
	400	Clamped Cantilever	68.4 69.0	0.9%

By examining the values, no clear trend can be observed. For some models, the clamped cylinder provides a higher resistance, while for others, the cantilever cylinder results in a higher resistance. There is also no clear correlation between the geometries and the difference in resistance between the two support conditions. However, it should be noted that for some models, the difference is so small that it is negligible. Therefore, it may be worth conducting further analyses covering a wider range of lengths and r/t ratios to determine whether the current method can be extended and formally considered applicable to cantilever cylinders.

This page is intentionally left blank.

6 Effect of Conditions in Monopiles

As discussed in chapter 3, the current analytical buckling verification methods in EN 1993-1-6 assume cylinders under uniform global bending with a full-circumferential dimple at midspan. In contrast, monopiles typically experience an increasing bending moment distribution, and according to the tolerance requirements in the standard, see section 2.4.2, the extent of possible dimples or weld depressions must be limited in both axial and circumferential directions. These two conditions presumably cause the analytically calculated buckling resistances to become conservative for monopiles. The aim of this chapter is therefore to reveal the extent of potential conservatism as well as to propose a way to mitigate it for each of the two conditions separately.

6.1 Effect of Moment Distribution

This section aims to assess the increase in buckling resistance associated with the elastic critical moment M_{cr}, by generating a linearly increasing moment distribution in cantilever cylinders and deriving a fitted expression for M_{cr} using LBA, corresponding to set 2 in the research plan described in section 3.2.3.

Assuming a uniform bending moment distribution implies that the maximum moment occurring in a cross-section acts along the entire length of the cylinder. In contrast, a cantilever cylinder is exposed to a lower level of loading compared to a structure under uniform bending, since the maximum moment is only present at the fixed end. As described earlier in section 3.1, the moment is assumed to increase linearly from top to bottom, which is a simplification of the real moment distribution in monopiles. To generate a linearly increasing bending moment distribution, a shear force is applied at the top as described in section 4.1.2.

A new parameter ψ is introduced, defined as the ratio between the two end moments as given in (6.1). The analyses are performed with varying ψ values.

$$\begin{aligned} \psi &= \frac{M_{top}}{M_{bottom}} \\ \psi &= \{0.00,\ 0.25,\ 0.50,\ 0.75,\ 1.00\} \end{aligned} \tag{6.1}$$

Models with $\psi = 1$ are equivalent to those in LBA set 1, where the moment distribution is uniform. Figure 6.1 shows the size of the shear force and the bending moment to achieve the respective models with different ψ values. The moment at the bottom is defined as 1.0 MNm, ensuring that the load multiplier from the LBA corresponds to M_{cr}.

Preliminary analyses revealed that for $\psi = 0$, shear buckling occurs at short lengths and high r/t ratios. Since shear buckling is beyond the scope of this project, a maximum r/t ratio is chosen as 100, and for that value, pure shear buckling is avoided at lengths $L \geq 25$ m. Models with other r/t ratios and lengths are excluded

from further investigations. As in chapter 5, the primary focus is on r/t ratios above 35. Since no capacity curve needs to be mapped in this context, it is not necessary to investigate all r/t ratios between 35 and 100. Rather, it is sufficient to include a reasonable number of data points to perform a reliable fit. Therefore, a subset of representative values is selected, given in (6.2). As a result, the total number of analyses in set 2 is reduced from the original 429 to 192.

$$r/t = \{35, 45, 55, 65, 75, 100\} \tag{6.2}$$

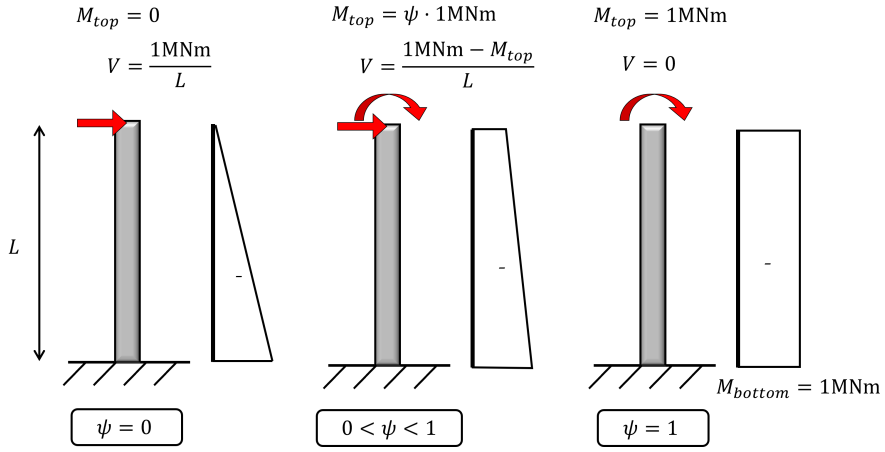

Figure 6.1: Values of applied moment and shear force depending on ψ

6.1.1 Eigenmodes

The eigenmode for a cylinder subjected to a shear force and the corresponding moment looks different compared to a cylinder under uniform bending moment, as shown in Figure 6.2.

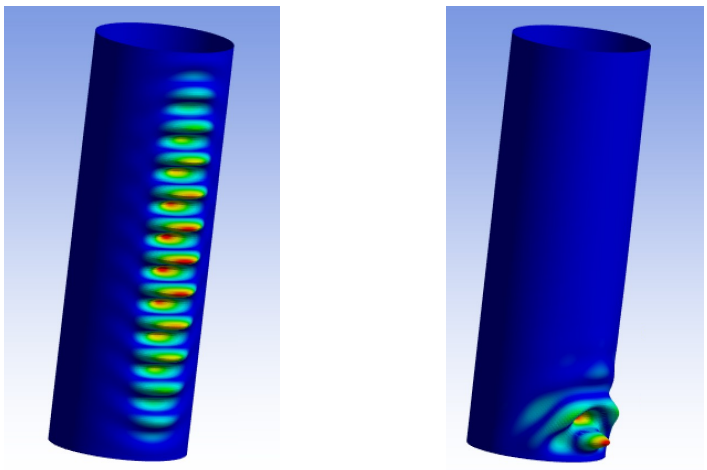

a) Pure bending b) Increasing moment due to shear force

Figure 6.2: Eigenmodes due to different load effects

There are two main differences. First, buckles do not occur along the entire length in the case of an increasing moment, as they do with a uniform moment. Instead,

the buckles appear near the bottom, where the bending moment is largest. Second, the buckles differ in appearance. The buckles in Figure 6.2 a) occur due to pure bending, whereas those in Figure 6.2 b) result from a combination of shear and bending moment.

It is observed that the larger the value of ψ, the more the buckling pattern resembles that of pure bending, as shown in Figure 6.3. It is also observed that increasing the length leads to buckling patterns that more closely resemble those caused by pure bending. This is expected, as the bending moment in long cylinders is more dominant than the shear force.

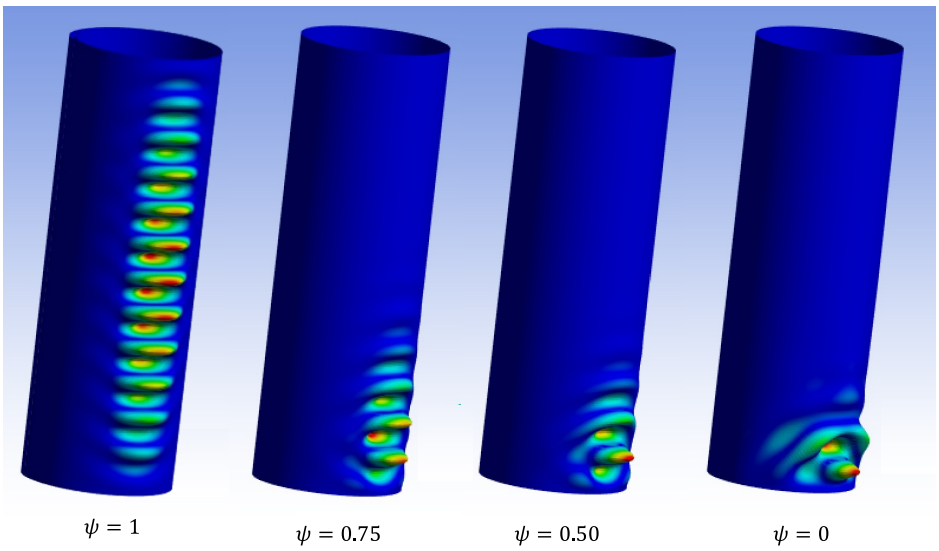

Figure 6.3: Appearence of eigenmode for different ψ values

6.1.2 Assessment of Results

By performing LBA, M_{cr} can be determined numerically for each geometry. The results are shown in Figure 6.4 for $L = 25$, 35, 45 and 60 m, as a function of the moment ratio ψ and the relative length ω.

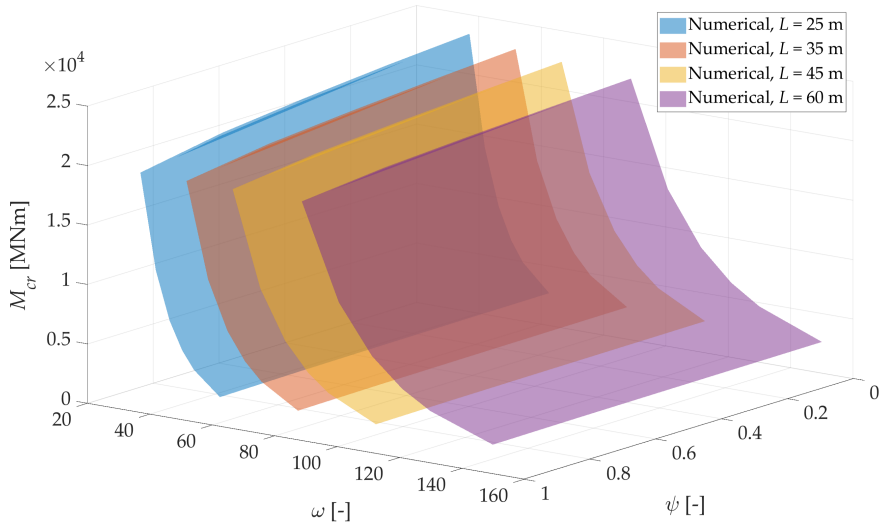

Figure 6.4: Comparison of numerical results

It is not apparent in the 3D plot above how M_{cr} varies depending on the value of ψ. Therefore, a 2D plot is shown in Figure 6.5 where results are visualised for $L = 25$ and 60 m for all r/t ratios.

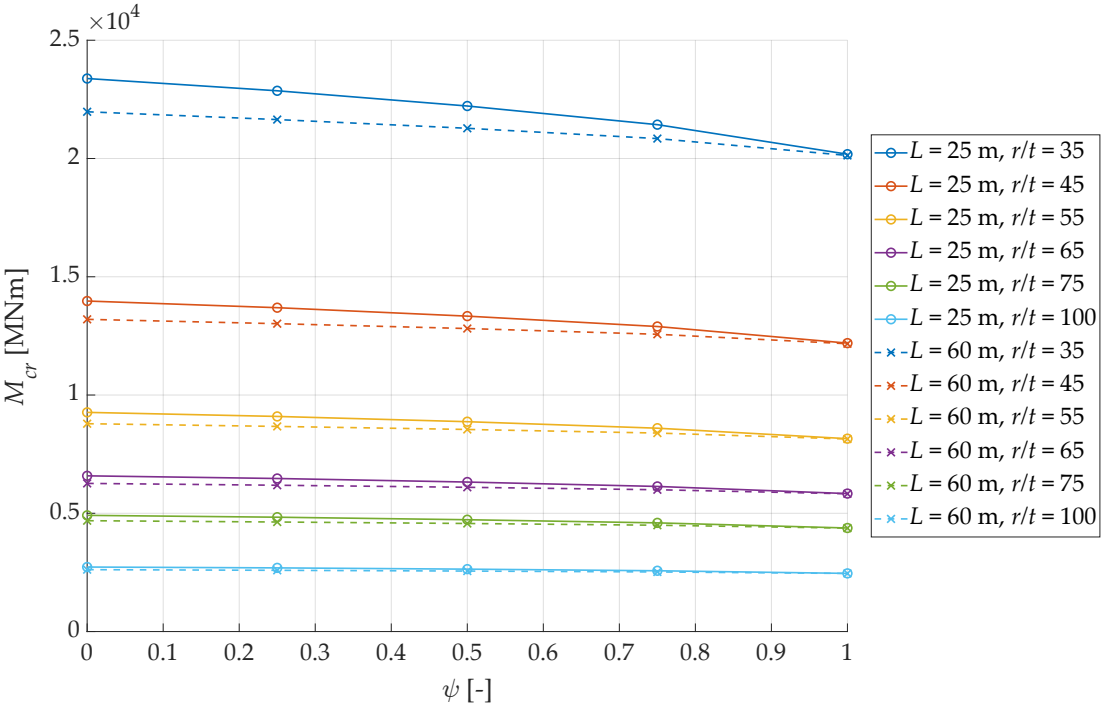

Figure 6.5: Comparison of numerical results

Several trends can be observed from the plot above, including that the highest resistance occurs at $\psi = 0$, and that it decreases as ψ approaches 1. It is also evident that a smaller length and r/t ratio result in greater buckling resistance. For example, the resistance is consistently higher for $L = 25$ m across all r/t ratios compared to $L = 60$ m. Hence, M_{cr} is seen to vary as a function of the length, the r/t ratio and ultimately ψ. Furthermore, it is observed that each set of five data points appears to follow a second-degree polynomial.

6.1.3 New expression for C_m

Recall that M_{cr} is determined as the product of the classical elastic critical moment M_{cl} and the parameter C_m as shown in (6.3).

$$\begin{aligned} M_{cr} &= C_m M_{cl} \\ C_m &= 1 + \frac{4}{\omega^2} \\ \omega &= \frac{L}{\sqrt{rt}} \end{aligned} \tag{6.3}$$

The original expression for C_m depends on ω, i.e. on the length and the r/t ratio. A new expression for C_m is sought that includes a dependency on ψ as well. Figure 6.6 shows the dependency of C_m on ψ and ω for selected lengths. This allows a surface to be fitted to the data points for each length. Note that $C_m = M_{LBA}/M_{cl}$ as $M_{LBA} = M_{cr}$.

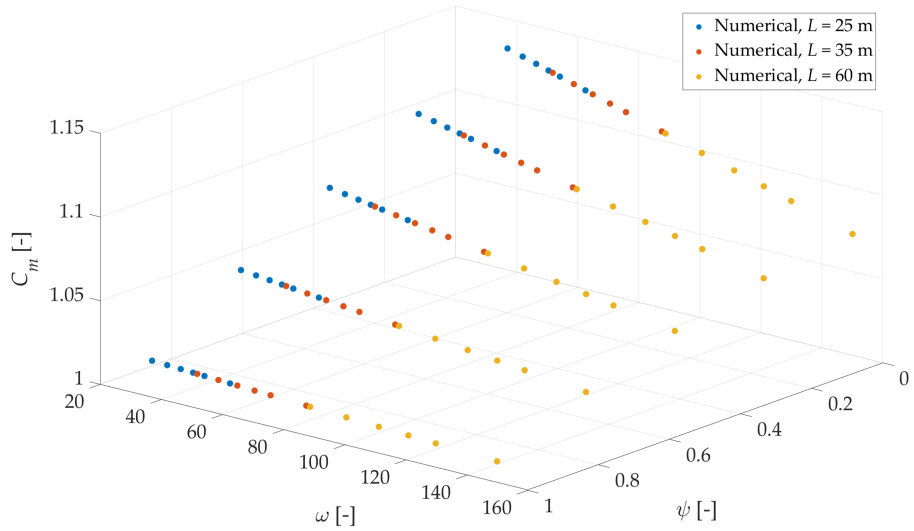

Figure 6.6: Comparison of numerical results

The Curve Fitting Toolbox [47] in the software MATLAB [48] is used to fit a polynomial surface for each length. The degree of the independent variables ψ and ω can be selected, which determines the final form of the polynomial function. It turns out that a second-degree fit in ψ works quite well. However, it is debatable whether ω should vary linearly or quadratically. The polynomial function consists of six terms when ψ and ω vary quadratically as shown in (6.4). And it consists of five terms when ψ varies quadratically and ω linearly as shown in (6.5).

$$f(\psi,\omega) = a_0 + a_1\psi + a_2\omega + a_3\psi^2 + a_4\psi\omega + a_5\omega^2 \tag{6.4}$$

$$f(\psi,\omega) = a_0 + a_1\psi + a_2\omega + a_3\psi^2 + a_4\psi\omega \tag{6.5}$$

Figure 6.7 shows how C_m varies with respect to ω for different values of ψ. It does not appear that ω varies linearly, especially for $\psi = 0$. However, by fitting a surface where the independent variables vary quadratically, the coefficient a_5 in the last term is found to be nearly zero. Since the function in (6.5) provides a sufficiently accurate fit, this form is adopted in the following. The reduced number of terms also makes the function more manageable.

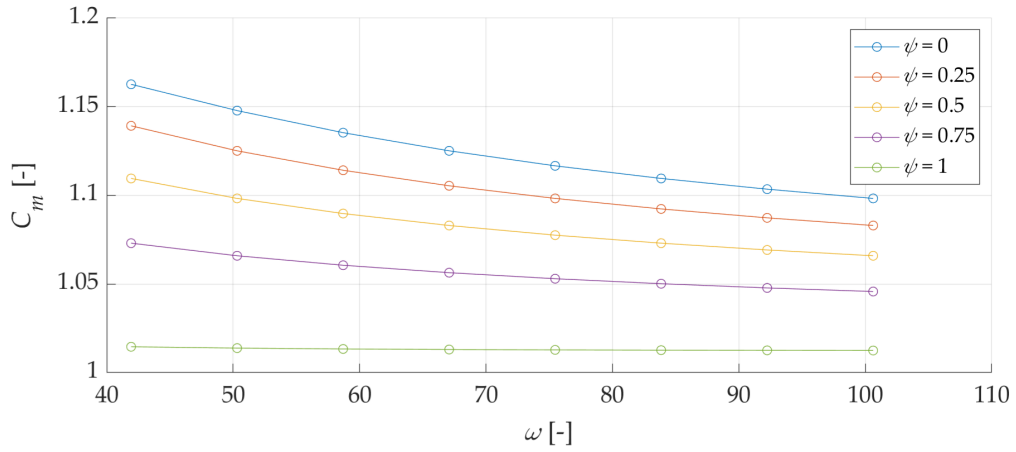

Figure 6.7: Numerical values of C_m as a function of ω

The next step is to determine suitable expressions for the coefficients a_i. Currently, there is no connection between the individual surfaces fitted for each value of L. The fits obtained for the different lengths are used to derive expressions for the coefficients. Figure 6.8 shows the coefficients as functions of L/r. Note that the radius r is constant in this study, but it is included to normalise L, thereby keeping the expressions dimensionless.

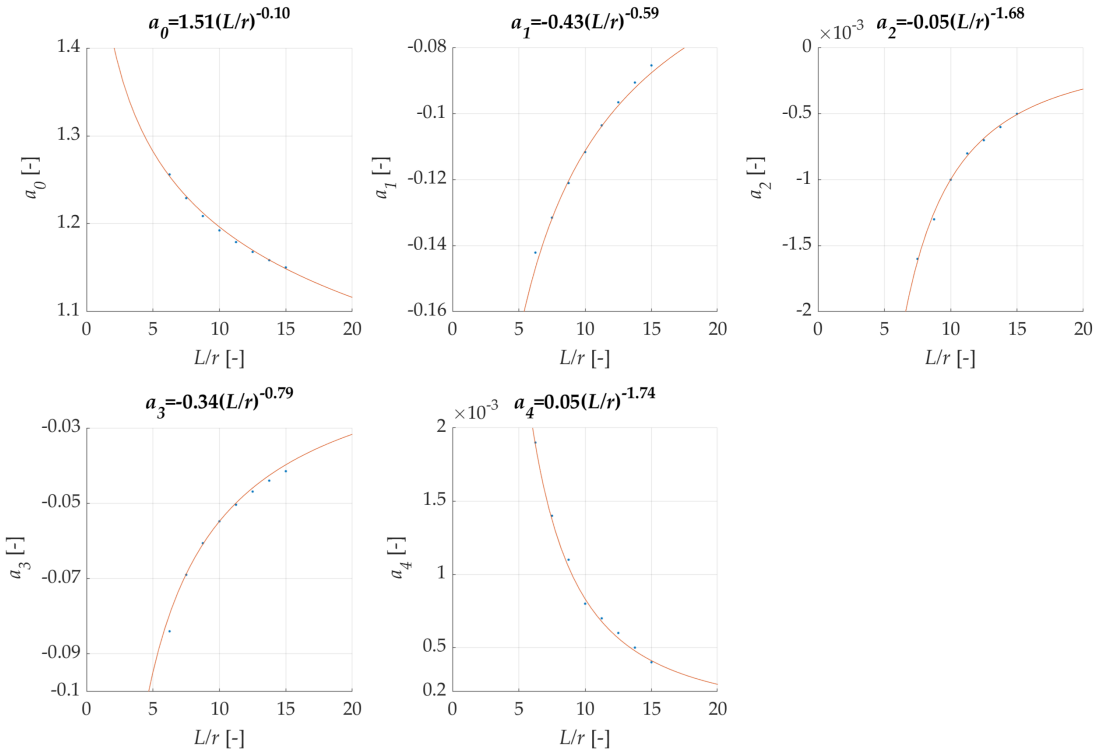

Figure 6.8: Fit for the coefficients a_i

A final expression for C_m in the interval $0 \leq \psi < 1$ is now established depending on ψ, ω and L, as shown in (6.6), while the coefficients are given in (6.7). For $\psi = 1$, the parameter C_m can be determined according to the rewritten expression found in section 5.2, which is listed again in (6.6).

$$C_m = \begin{cases} 1.025 \left(\frac{r}{t}\right)^{-0.0035} + \frac{4}{\omega^2} & \text{for} \quad \psi = 1 \\ a_0 + a_1\psi + a_2\omega + a_3\psi^2 + a_4\psi\omega & \text{for} \quad 0 \leq \psi < 1 \end{cases} \tag{6.6}$$

where:

$$a_0 = 1.51 \left(\frac{L}{r}\right)^{-0.10}, \quad a_1 = -0.43 \left(\frac{L}{r}\right)^{-0.59}, \quad a_2 = -0.05 \left(\frac{L}{r}\right)^{-1.68}$$
$$a_3 = -0.34 \left(\frac{L}{r}\right)^{-0.79}, \quad a_4 = 0.05 \left(\frac{L}{r}\right)^{-1.74} \tag{6.7}$$

Figure 6.9 presents a comparison between the new expression and the numerical results for $L = 25$ m. In some regions, the expression overestimates the value of C_m by 0.9 % at most, and in others, it underestimates C_m by 3.9 %. This shows a good agreement between the fit and the numerical results.

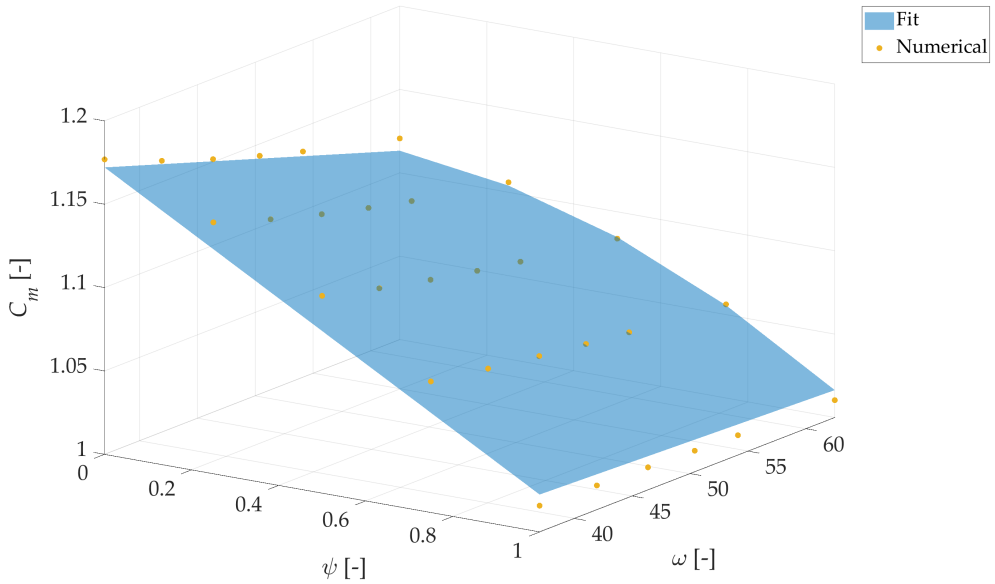

Figure 6.9: Comparison of numerical results and fit for $L = 25$ m

To better illustrate how well the fit matches the data points, Figure 6.10 can be considered. It can be seen that the fits resemble parabolic curves.

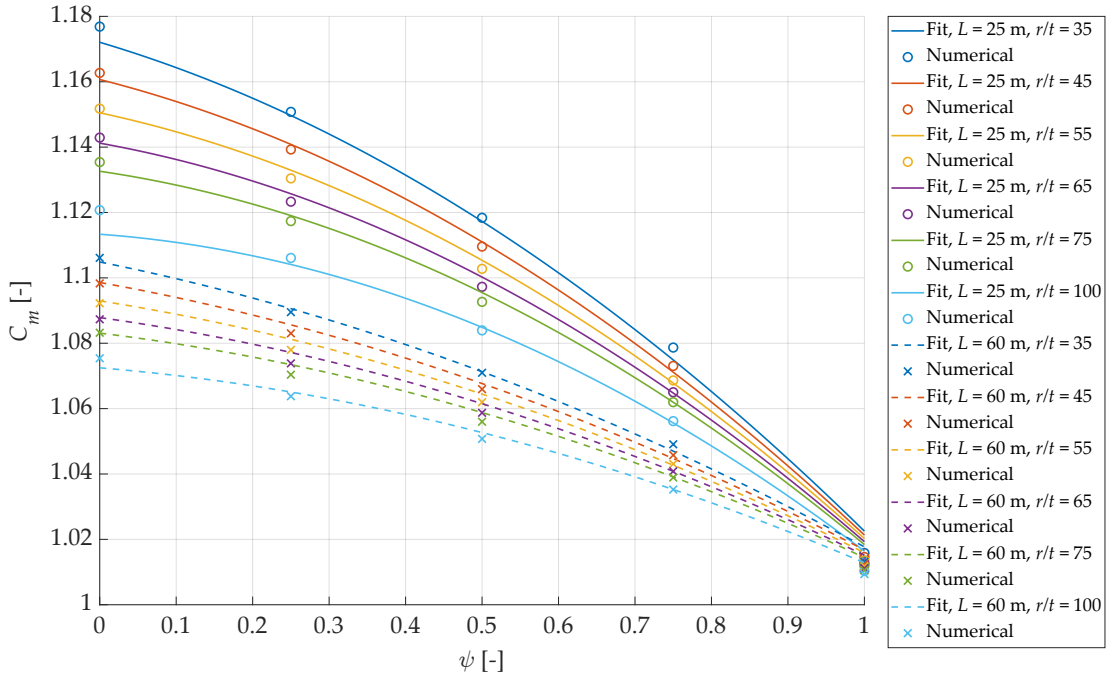

Figure 6.10: Comparison of numerical results and corresponding fits

Figure 6.11 shows a comparison of the numerical and fitted M_{cr} for $L = 25$ m.

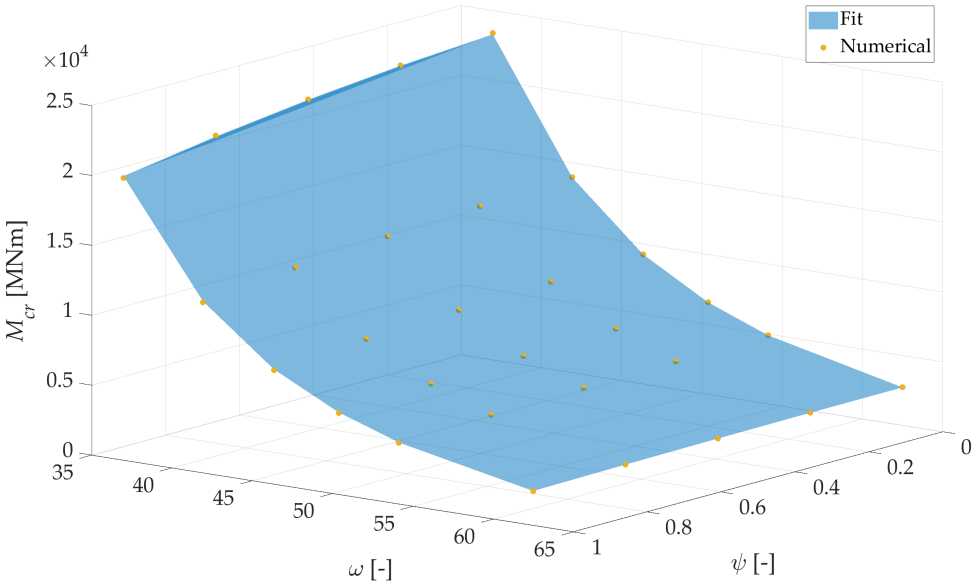

Figure 6.11: Comparison of numerical results and fit for $L = 25$ m

6.1.4 GMNIA with Increasing Moment

In the following, the compatibility of the new expression for C_m with the analytical method in prEN 1993-1-6 is investigated. Therefore, additional GNMIA analyses with increasing moment are carried out, using the geometries given in (6.8) and FTQC A. Based on information provided by Vattenfall, ψ ranges from 0.59 to 0.65. Nevertheless, a single value of $\psi = 0.5$ is investigated to enable comparison with the previously presented results, which include calculations for $\psi = 0.5$.

$$\begin{aligned} r/t &= \{35, 55, 75\} \\ L &= \{25, 45, 60\} \text{ m} \end{aligned} \tag{6.8}$$

Given that the maximum moment occurs at the bottom of the cylinder, the imperfection should be positioned in that region at the most critical location, namely where it leads to the lowest resistance. Therefore, the imperfection is placed at five different positions within the lower quarter of the cylinder in order to identify the most critical location. Figure 6.12 shows an example of the imperfection placements for $L = 25$ m, where position 1 corresponds to a distance of 3 m from the bottom to the centre of the imperfection, and position 5 corresponds to the centre of the imperfection being located at $L/4$. Between positions 1 and 5, the imperfection is placed at three additional equally spaced locations. It should be noted that the height of the imperfection corresponds to the double of the linear meridional bending half-wavelength, i.e. 2Λ. For the selected geometries, 2Λ ranges from 1.8 to 3.2 m.

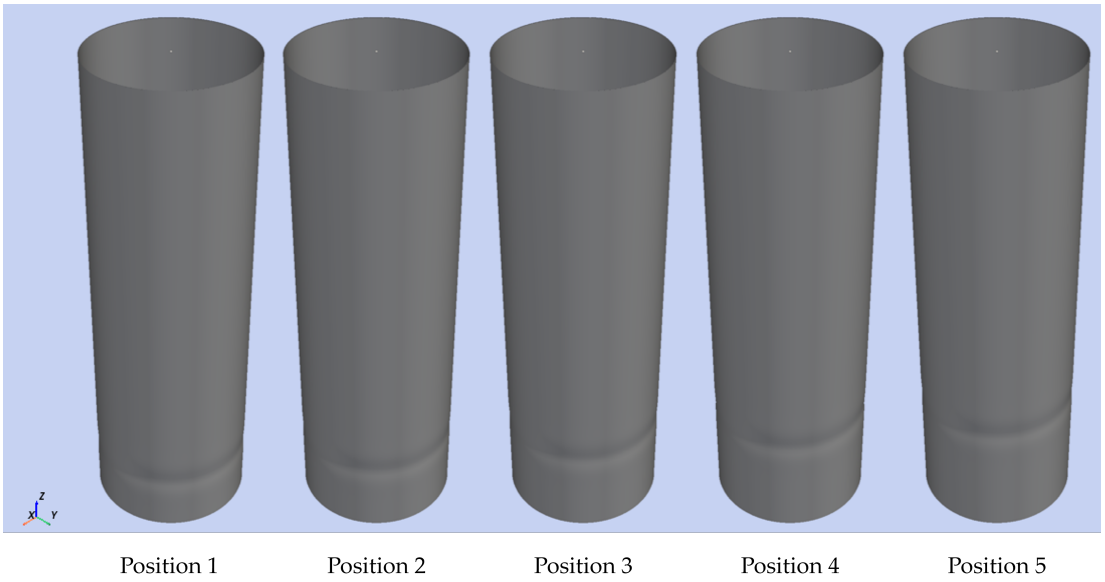

Figure 6.12: Imperfection positions for $L = 25$ m

Figure 6.13 shows a comparison between the characteristic buckling resistance M_{Rk} for the previously performed GMNIA analyses corresponding to set 1 with uniform bending moment, and the newly performed GMNIA analyses with increasing moment. The models with increasing moment exhibit significantly higher resistances — with the largest difference being 12.3% and the smallest 7.0%. This indicates that there is considerable capacity to gain by reformulating the method to be based on increasing bending moment instead of uniform bending moment. A cluster of five data points can be seen at various locations in Figure 6.13, corresponding to analyses of the same geometry but with varying positions of the imperfection.

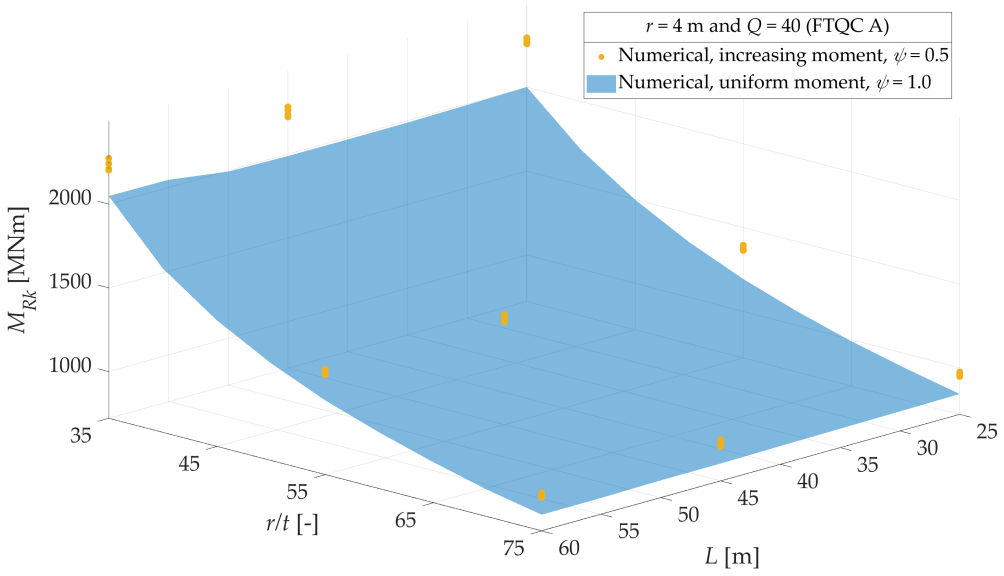

Figure 6.13: Comparison of numerical results for $\psi = 0.5$ and 1

By considering Figure 6.14, it can be seen that the most critical location is not necessarily where the moment is largest. For $L = 60$ m, the lowest value of M_{Rk} occurs when the imperfection is located at either position 2 or 3, depending on the r/t ratio. However, for $L = 25$ m, the most critical case is when the imperfection is located at position 1 for all r/t ratios. A clear correlation can be observed between the cylinder length, the r/t ratio and the most critical location of the imperfection, which may be linked to the shapes of the eigenmodes associated with the different geometries.

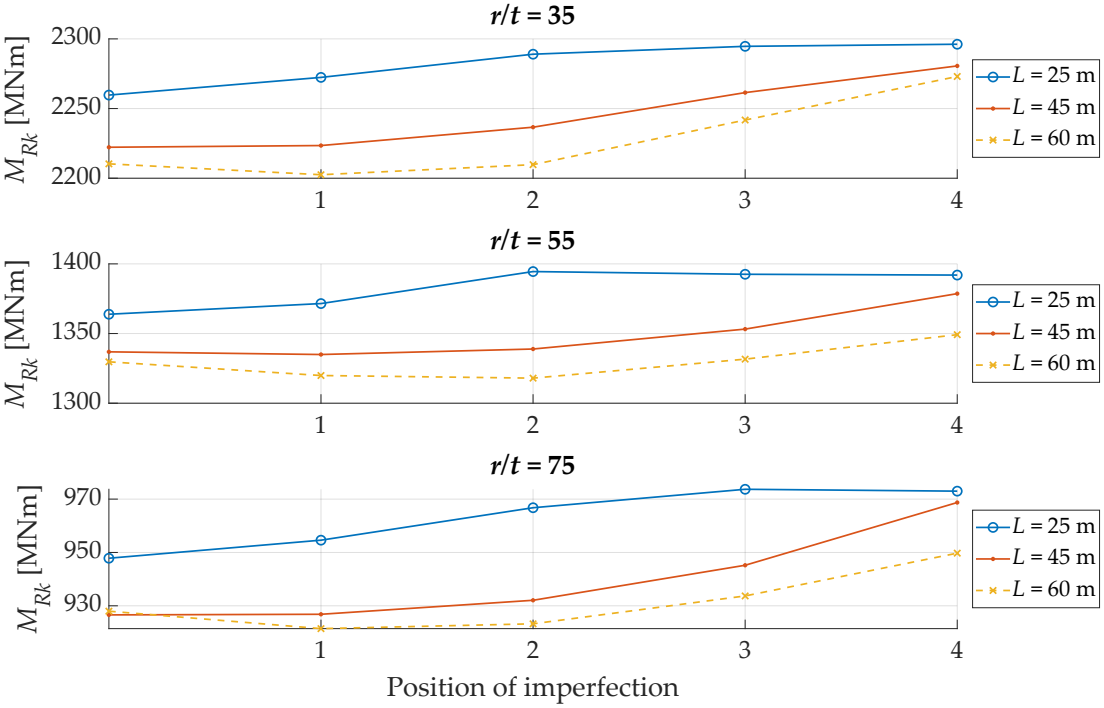

Figure 6.14: Effect of imperfection position on the characteristic buckling resistance (FTQC A)

Figure 6.15 shows the shape of the eigenmodes for different lengths and r/t ratios. Note that for geometries with the same r/t ratio, the height of the largest buckles is the same, since $\Lambda = 2.444\sqrt{rt}$. It appears that for larger r/t ratios, the buckles become narrower. For $L = 25$ m, the pattern covers a smaller area, i.e. smaller height and width, compared to $L = 60$ m, meaning there are fewer buckles. This might explain why the critical location of an imperfection is not at the very bottom for $L = 60$ m, as the critical buckle is located in the centre of the buckling pattern, i.e. at a slightly higher position along the cylinder. This implies that for the design of an actual structure, the imperfection should be introduced at the most critical location of the eigenmode, which is the point where buckling is most likely to initiate.

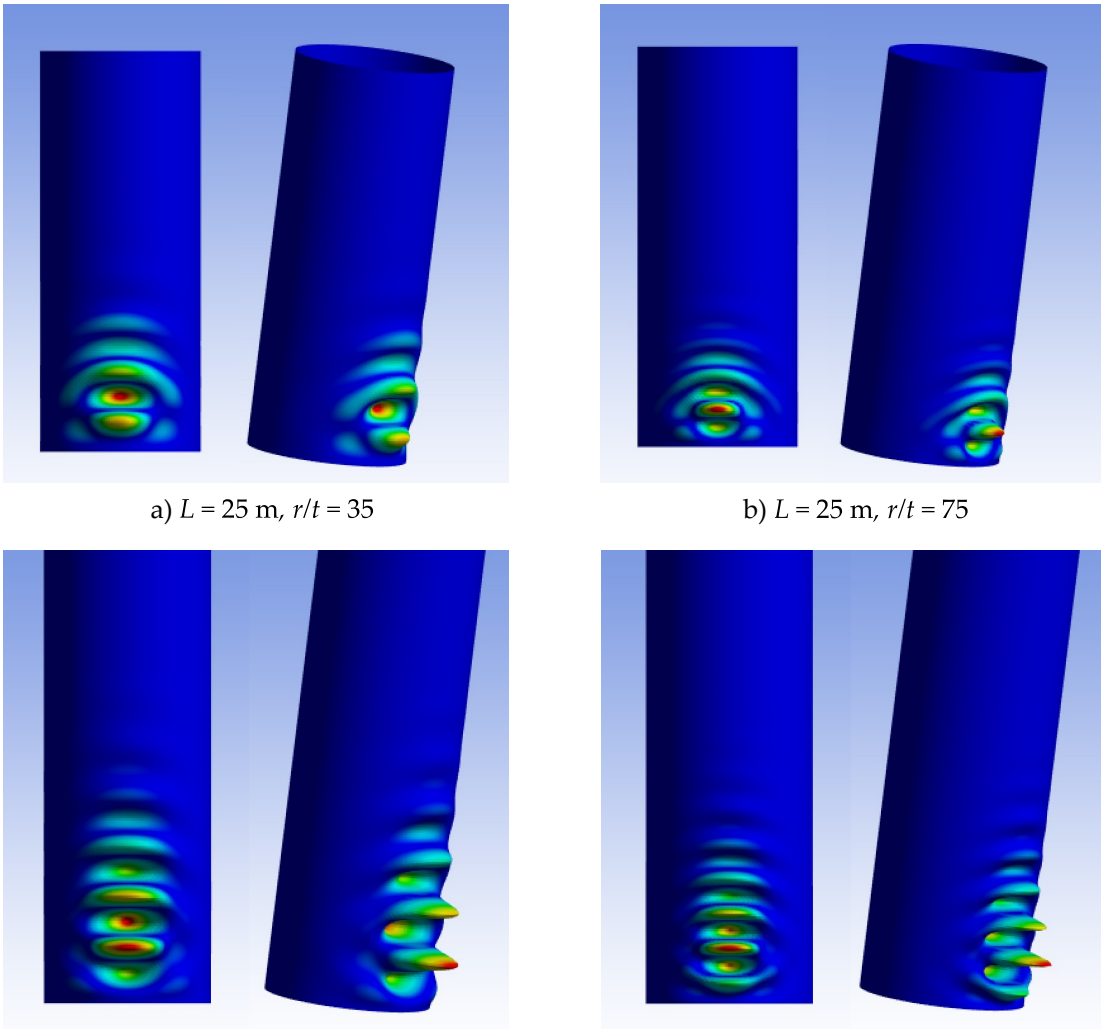

a) $L = 25$ m, $r/t = 35$

b) $L = 25$ m, $r/t = 75$

c) $L = 60$ m, $r/t = 35$

d) $L = 60$ m, $r/t = 75$

Figure 6.15: Eigenmodes for different lengths and r/t ratios

The elastic critical buckling resistance M_{cr} is included in the method through the calculation of the slenderness $\overline{\lambda} = \sqrt{M_{pl,I}/M_{cr}}$. A higher value of M_{cr} will naturally increase the characteristic buckling resistance M_{Rk}, although not significantly. As an attempt to align the analytical method better with the numerical results, it can be considered to multiply M_{Rk} by C_m, see (6.9).

$$\chi = \frac{C_m M_{Rk}}{M_{pl,I}}, \qquad \chi \leq 1 \tag{6.9}$$

Figure 6.16 shows the buckling reduction factor depending on the r/t ratio and length. The analytical results for χ with $\psi = 0.5$ are calculated as given in (6.9). As for $\psi = 1$, C_m is simply excluded. The surface representing the analytical results for uniform moment provides lower values of χ compared to the numerical results. The new analytical results for increasing moment are closer to the numerical results, with some being on the conservative side and others on the unconservative side. A strong correlation between the numerical and analytical results for increasing moment cannot be expected, since C_m is fitted to results from LBA rather than GMNIA. As a result, C_m does not account for either the amplitude or the location of the imperfection.

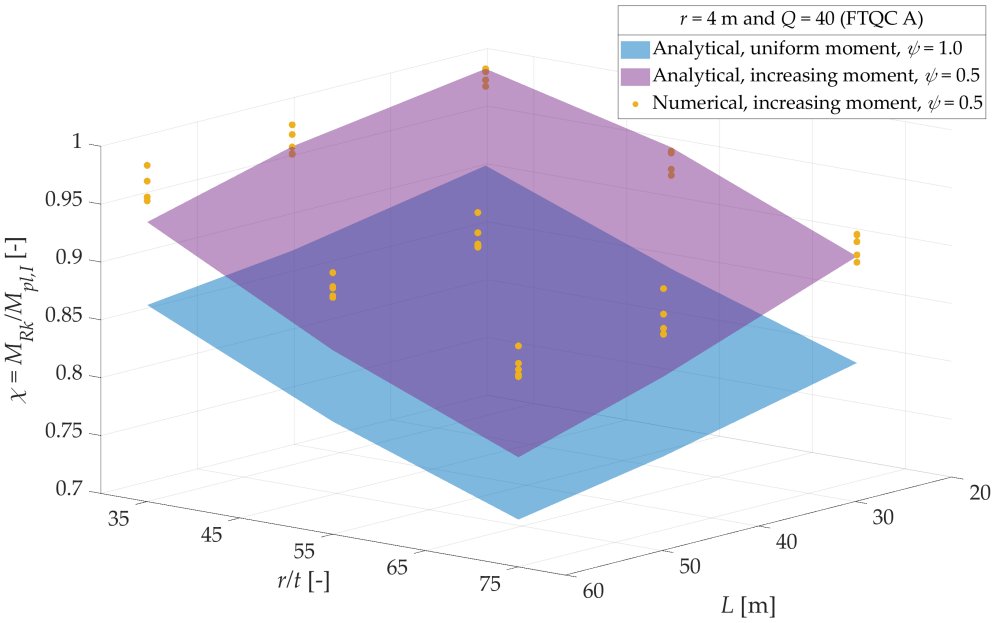

Figure 6.16: Comparison of results (FTQC A)

This section can be concluded by stating that the moment distribution has a significant influence on the buckling resistance. The new expression for C_m can be used to determine a more accurate value of M_{cr} and, accordingly, a more accurate relative slenderness $\overline{\lambda}$ leading to an increase of the buckling reduction factor χ. It is also possible to multiply C_m with the final χ value, but caution should be exercised to ensure that the result does not fall on the unconservative side. There is also potential for further development of the method, for example by fitting C_m or a new parameter to GMNIA results, where the parameter should depend on the size and location of the imperfection.

6.2 Effect of Imperfection Form

As discussed in chapter 3, the analytical methods assume a geometric imperfection in the form of a full-circumferential dimple at midspan, even though EN 1993-1-6 limits the tolerable size of a possible dimple not only in the axial but in the circumferential direction as well. In light of that, it is investigated in the following how the characteristic buckling moment resistance is affected by the extent or form of the applied geometric imperfection. Numerical results for cylinders with a full-circumferential dimple were presented in chapter 5, including a comparison with analytical values. The same is done below for cylinders with a limited dimple, concluding with comparing the two sets of numerical results and evaluating the effect of imperfection form.

Since the analytical method was found to be unconservative for a wide range of possible monopile geometries, it is compared here with numerical results for cylinders with a limited dimple, despite the fact that it was not developed based on that assumption. Results from 429 geometrically and materially nonlinear analyses of imperfect

cylinders (GMNIA) are presented in Figure 6.17 together with the analytically calculated buckling moment resistances for excellent fabrication tolerance quality class, FTQC A.

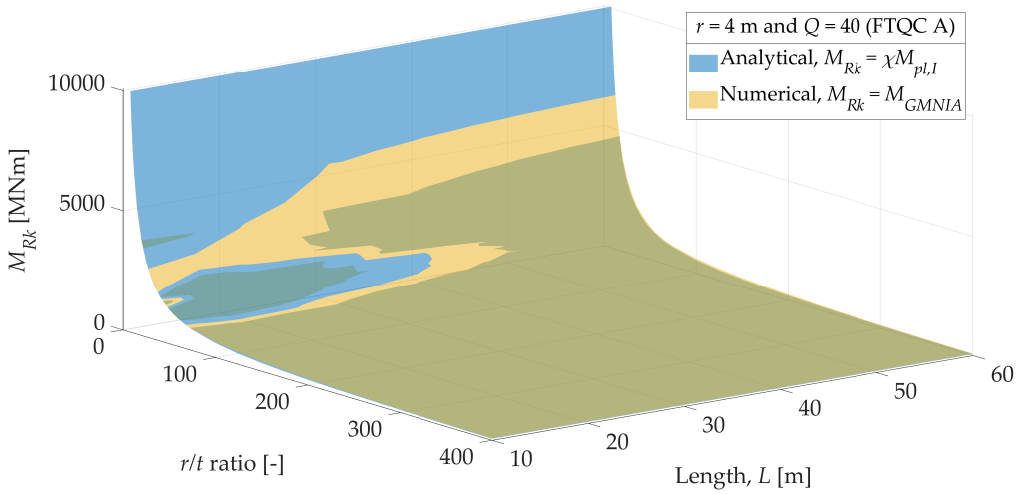

Figure 6.17: Comparison of characteristic buckling moment resistances

The same set of results is visualised in Figure 6.18 in normalised form in terms of the buckling reduction factor, where the deviation between the values is more prominent. Both figures show that the analytical method is still unconservative for large thicknesses or low r/t ratios, as well as for certain moderate thicknesses when combined with smaller lengths. This might seem somewhat surprising, but as expected, the extent of the unconservative region is reduced compared to cylinders with a full-circumferential dimple. On the other hand, a significant deviation can be observed at low thicknesses or high r/t ratios, which is especially visible in Figure 6.18. Results for FTQC B and C show a similar pattern, although the deviation increases with the imperfection amplitude, and thus the unconservative region becomes gradually smaller.

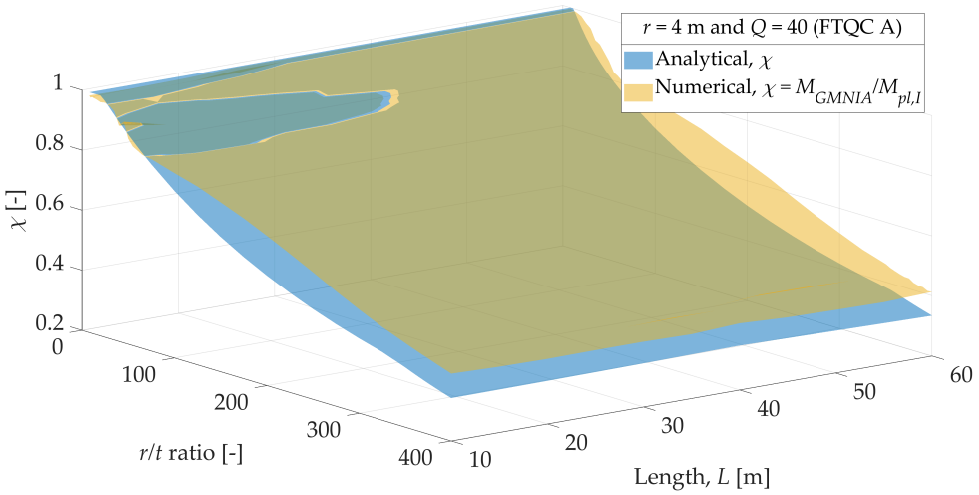

Figure 6.18: Comparison of buckling reduction factors

A similar observation can be made when looking at Figure 6.19, which shows numerical results for cylinders with full-circumferential and limited dimples. The difference is smallest at large thicknesses or small r/t ratios and increases with r/t as well as with the imperfection amplitude. The highest relative difference between models with the two imperfection forms is 17.7% for FTQC A in general and reduces to 7.1% when only possible monopile geometries are considered.

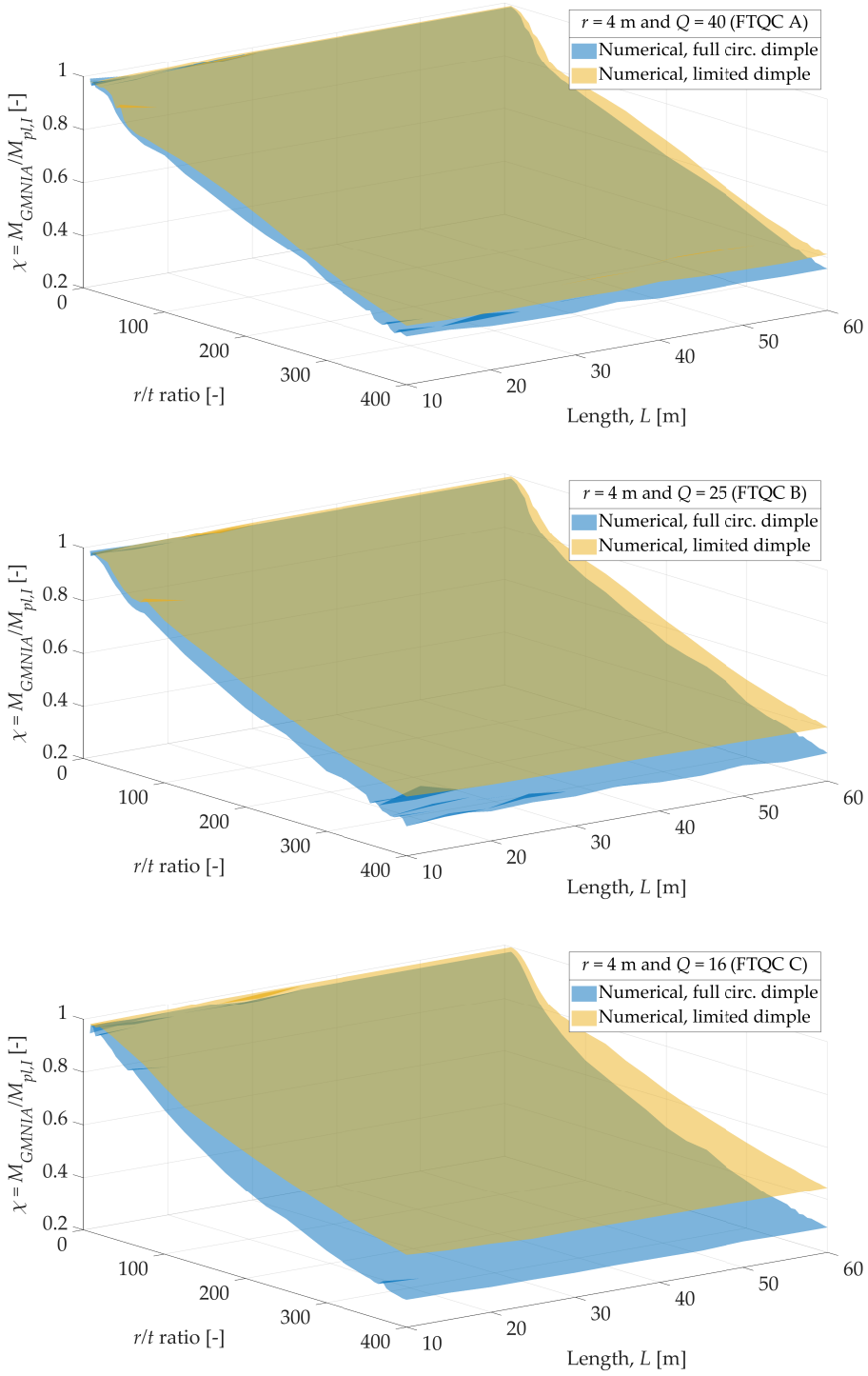

Figure 6.19: Comparison of numerically calculated buckling reduction factors

The buckling reduction factor is plotted for the three standard quality classes in Figure 6.20, focusing on possible monopile geometries. It can be observed that the analytical values in FTQC A are in fact unconservative for lengths up to 30 – 40 m, depending slightly on the r/t ratio, and even outside that range, the highest relative deviation is 6.8%. The deviation increases with the imperfection amplitude, and the analytical method becomes fully conservative in FTQC C.

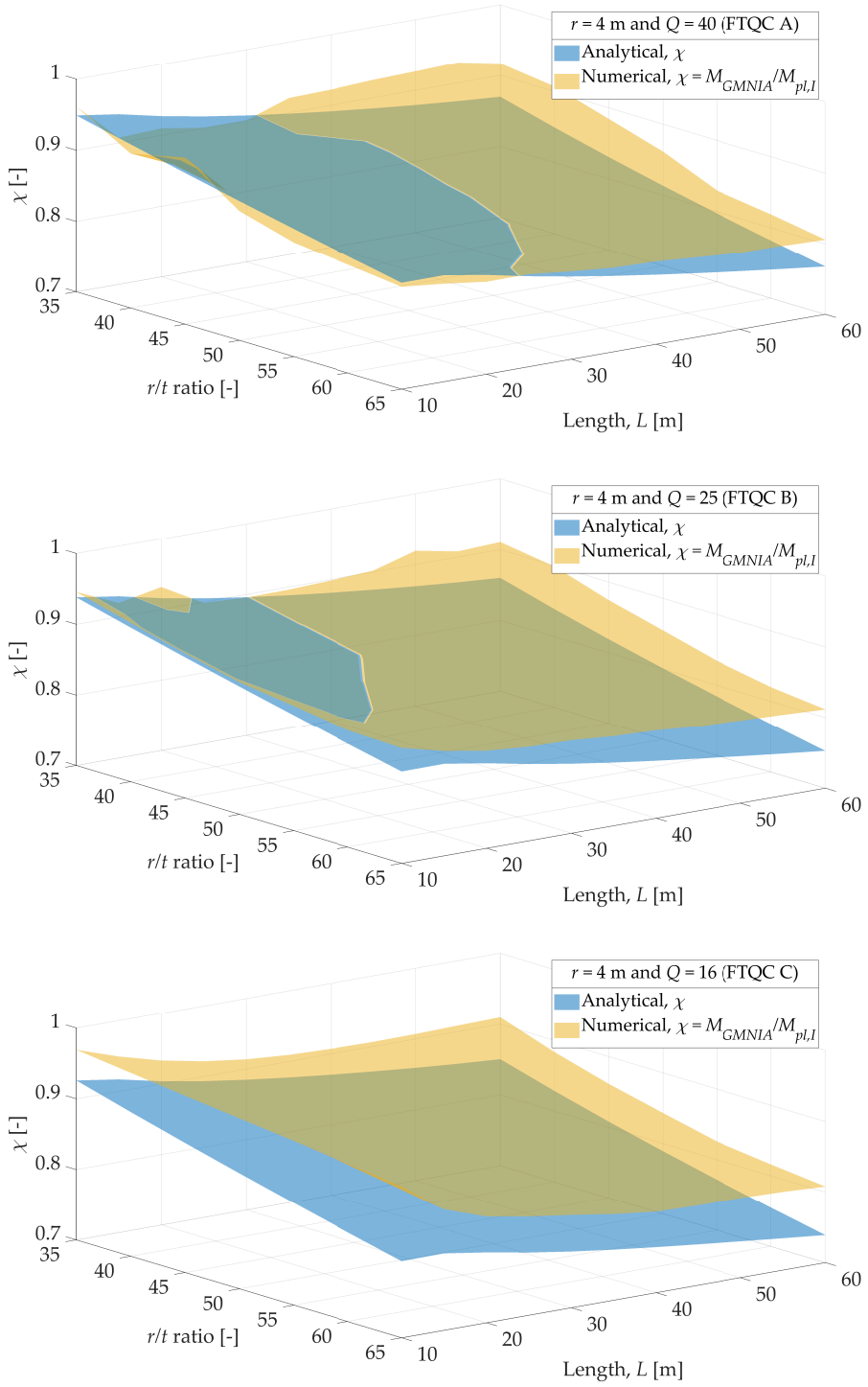

Figure 6.20: Comparison of buckling reduction factors for monopile geometries

The relative deviations between the numerical and analytical results are visualised in Figure 6.21, where positive values indicate higher numerical results. The analytically calculated values can be slightly shifted closer to the numerical ones in an average sense (i.e. decreasing the mean relative deviation) by using the reformulated expressions for C_m and α_G from chapter 5. However, all capacity curve parameters need to be rewritten to make the analytical method appropriate for cylinders with a limited dimple.

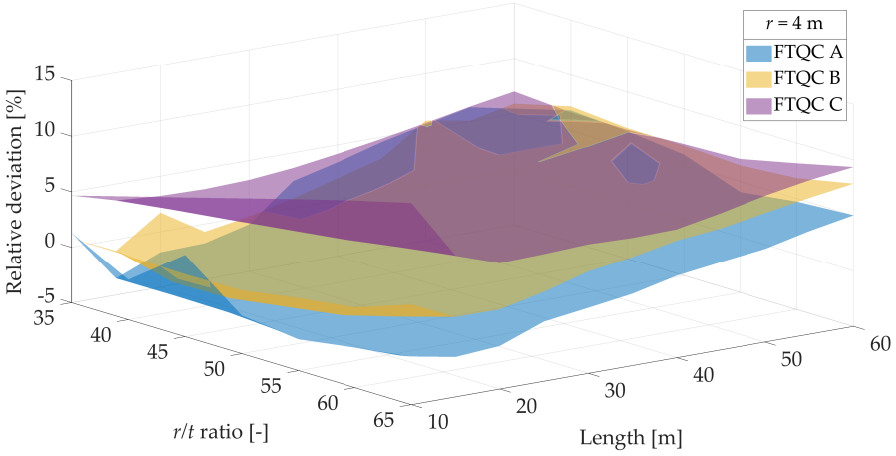

Figure 6.21: Deviation between numerical and analytical results for monopile geometries

The results can also be presented as traditional capacity curves, depicted in Figure 6.22 for FTQC A. Similarly to the case with full-circumferential dimple, analytical curves are shown for three selected Ω values, whereas the majority of the numerical data points correspond to different Ω and thus would lie on different curves. When comparing the figure to Figure 6.18, it can be seen that they resemble each other. The analytical method is rather conservative for slender and very slender structures, i.e. high relative slenderness or high r/t ratio, and gradually becomes less conservative and eventually unconservative as the slenderness decreases.

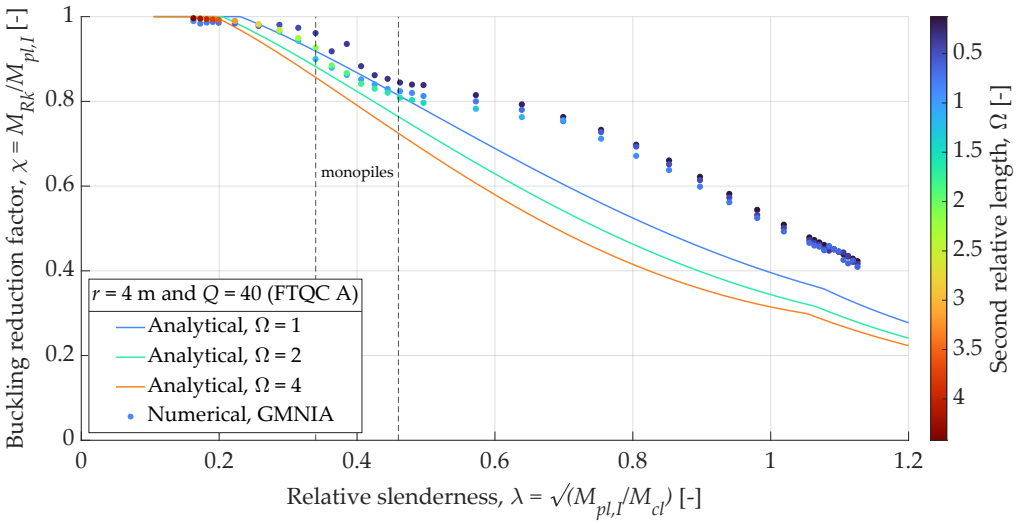

Figure 6.22: Capacity curves with numerical results for cylinders with limited dimple

Due to the fact that the numerical results correspond to distinct capacity curves, it is not possible to reformulate the capacity curve parameters at the boundaries, i.e. $\overline{\lambda}_0$, β, η_0 and η_p, based on calculations for the chosen geometries. Therefore, the planned GNIAs and MNIAs for cylinders with a limited dimple are not performed. The adaptation of the existing analytical method, assuming a full-circumferential dimple, to cases with a limited dimple would require a more careful selection of cylinder dimensions so that several geometries with equal Ω values can be obtained. However, based on the results, it can be concluded that the existing method is probably appropriate enough for preliminary dimensioning of typical monopiles in FTQC A and B, and it is even slightly unconservative in some cases. For FTQC C, the method is fully conservative and leads to larger deviations from the numerically calculated resistances.

This page is intentionally left blank.

7 Discussion

A research plan was presented in section 3.2.3 to achieve the objectives outlined in the problem statement, and it was structured around the differences between the implicit assumptions behind the analytical method and the actual conditions present in a monopile. The research plan consisted of three calculation sets, which were presented in Table 3.3. In set 1, the numerical models were constructed as cantilever cylinders under uniform global bending with a full-circumferential dimple, with the results assessed in chapter 5. In set 2, the models experience a linearly increasing moment distribution instead of a uniform one. While in set 3, the models included a limited dimple imperfection instead of a full-circumferential one. In sets 2 and 3, more attention was given to the conditions encountered in a monopile, and the results were discussed in chapter 6.

Some adjustments to the research plan were made as the project progressed. Table 7.1 is a revised version of Table 3.3, showing an overview of the analyses that actually were carried out in this project and how the results were used. In the following, the outcome of each analysis type across the respective sets is summarised, along with an explanation of any changes that were made.

Table 7.1: Overview of conducted simulations

Set	Analysis type	Number of r/t	L	Q	Total no. of simulations	Achieved purpose
1	LBA	39	11	–	429	Assessment & reformulation of C_m
	MNA	16	3	–	48	Assessment of M_{pl}
	MNIA	16	3	3	144	Assessment of κ
	GNA	39	11	–	429	Assessment & reformulation of α_G
	GNIA	39	11	3	1 287	Assessment of α_I
	GMNA	39	11	–	429	Input to GMNIA
	GMNIA	39	11	3	1 287	Assessment of M_{Rk}
2	LBA	6	8	–	192*	New C_m for increasing moment
	GMNIA	3	3	1	45**	Assessment of new C_m
3	MNIA	0	0	0	0	–
	GNIA	0	0	0	0	–
	GMNIA	39	11	3	1 287	Assessment of M_{Rk}

* Number of investigated ψ: 4

** Number of investigated ψ: 1, number of dimple positions: 5

7.1 Set 1

The LBAs in the 1st set are performed as initially planned with the goal of assessing and thereafter rewriting the parameter C_m, since it is conservatively set to 1 in prEN 1993-1-6:2023. The expression for C_m was taken from EN 1993-1-6/A1:2017 and was

revised in this report. With the new expression, the elastic critical moment M_{cr} can be determined more accurately.

The number of studied r/t ratios for the materially nonlinear analyses MNA and MNIA was reduced from 39 to 16. The initial choice of 39 was made in order to map the capacity curve. However, as the results from MNA and MNIA were expected to form a horizontal line at $\chi = 1$ in a capacity curve, such extensive analysis was not considered necessary. During the assessment of M_{pl}, it was found that the exact value could not be obtained with the constructed numerical model. It is assumed that the exact value of M_{pl} can be found using the analytically derived expression, since the expression is well established. No further action was taken, as the deviation between the numerical and analytical results was minimal. Regarding the assessment of κ, it was found that the expressions derived by Wang et al. [28] are more accurate than the one provided in prEN 1993-1-6. Since reliable and accurate expressions for κ already exist based on numerical calculations, it was deemed unnecessary to attempt further optimisation.

The GNAs were carried out as planned, including all 39 r/t ratios and 11 lengths. The purpose of these analyses was to assess the geometric reduction factor α_G and eventually revise its expression. The results showed that there was room for improvement, as the expression provided in prEN 1993-1-6 was found to be conservative in certain regions and provided underestimated values of α_G. Consequently, a revised expression was proposed to better align with the numerical results. With increasing values of α_G, the buckling reduction factor χ also increases, which in turn raises the characteristic buckling resistance M_{Rk}.

The main purpose of the GMNA was to determine the characteristic buckling resistance of the perfect structure $M_{Rk,\text{perfect}}$ in order to use it as the applied load in the GMNIA. As described in chapter 4, it is recommended to apply a load that is close to the actual resistance of the structure and $M_{Rk,\text{perfect}}$ is considered a suitable estimate. Another purpose of the GMNA results was to compare them with those from the GMNIA and to verify that $M_{Rk,\text{perfect}}$ is indeed greater than M_{Rk}. Although this comparison was not explicitly presented in the report, it was conducted as part of the internal verification process.

The objective of the GMNIA in set 1 was to assess the characteristic buckling resistance M_{Rk}, as well as to assess and potentially revise the expressions for the range boundary values η_0, η_p, $\overline{\lambda}_0$, and β. During the process, it was found that a consistent value of Ω is required in order to map a capacity curve. In other words, each value of Ω forms a separate capacity curve. To determine the range boundary values, a continuous capacity curve is needed, which was unfortunately not achievable with the results available. As a result, only an assessment of M_{Rk} was carried out. Surprisingly, it was found that the analytical method is unconservative for the geometry of monopiles, contrary to what is typically assumed about analytical methods. In other words, the method is actually unsafe when compared to the numerical results. However, it should be kept in mind that the assumption of a uniform moment is not valid in the case of monopiles, and the formation of a full-circumferential dimple is not realistic, which keeps a certain level of conservatism in the method.

The number of simulations for the GNIA was carried out as planned. The aim was

to assess the imperfection reduction factor α_I and potentially reformulate its expression. There was clearly room for adjustment to make the parameter less conservative in certain regions. However, this was not pursued because the numerical results from the GMNIA showed that the analytical method is already unconservative. Modifying α_I to make it less conservative would only increase this unconservatism of the method, which is not the intention.

It should be noted that the optimised expressions for C_m and α_G should not be used together with the current method, as this method is already unconservative. It was anticipated that the numerical results for the models with a limited dimple would yield larger resistances than those predicted by the current analytical method. Therefore, the parameters C_m and α_G were optimized with the intention of applying them within the analytical method, in order to increase the analytical results and achieve better alignment with the numerical results for models with a limited dimple.

7.2 Set 2

The number of investigated r/t ratios and lengths for the LBA in set 2 was reduced from what was initially planned. The main reason was the exclusion of all geometries that would experience pure shear buckling, as the focus in this project is solely on buckling caused by bending. Therefore, r/t ratios above 100 were excluded, along with lengths below 25 m. In LBA set 1, r/t ratios below 35 were disregarded, and thus also in set 2. Lastly, only six r/t ratios were chosen between $35-100$. The numerical results showed that the elastic critical moment M_{cr} for models with an increasing moment was higher than for models with a uniform moment, which led to the development of a new expression for C_m that determines a more acurrate value of M_{cr}.

Some GMNIA analyses, which were not initially planned, were carried out to investigate the difference in resistance between the numerical models with increasing moment and the analytical method derived based on uniform moment. When dealing with an increasing moment in a cantilever, the maximum moment occurs at the fixed end of the cylinder, which means that the imperfection should not be located at midspan but should instead be moved towards the support to account for the worst possible scenario. The imperfection was placed at five different heights within the lower quarter of the cylinder. Note that the imperfection took the form of a full-circumferential dimple to make the results more comparable with the analytical method. It was found that between 7% and 12% larger resistance could be gained by accounting for the increasing moment when dealing with monopiles. Even though C_m was fitted so that a more accurate value of M_{cr} could be determined, it was not enough to significantly increase the buckling resistance. As an additional measure and an attempt to align the analytical results with the numerical ones, the buckling reduction factor χ was increased by multiplying it with C_m. This produced reasonable results, but should only be implemented with careful consideration. It is important to consider where the imperfection should be placed in the model to represent the worst possible scenario. Therefore, it could be considered to either modify C_m or introduce an entirely new parameter that accounts for this. Moreover, it is important to note

that the actual moment distribution in a monopile is not linearly increasing, as it is simplified to be in this project, and that should also be taken into account.

7.3 Set 3

In set 3, only the GMNIA analyses were carried out as planned. This was due to the GMNIA results, which revealed that the analytical method was still unconservative in some areas when comparing it to the numerical results with a limited dimple as shown again in Figure 7.1 for FTQC A.

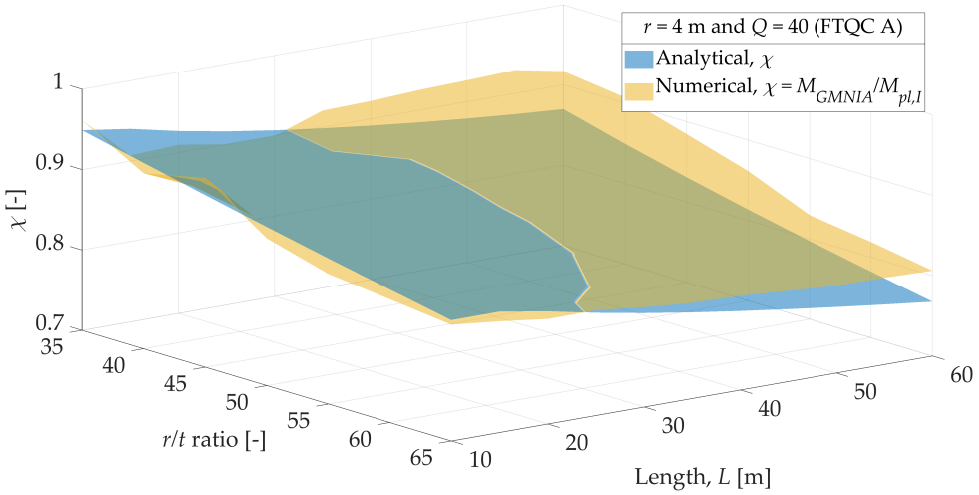

Figure 7.1: Comparison of analytical and numerical resuts for monopile geometries

The purpose of performing MNIA and GNIA with a limited dimple was to rewrite κ and α_I, which would most likely lead to an increase in these parameters. However, this was deemed unnecessary in order to avoid making the analytical method even more unconservative. By examining Figure 7.1, it can be seen that the analytical method only starts to become conservative at lengths above 30 m, and the conservatism increases with the length. Nevertheless, the method can still be considered sufficiently reliable for lengths up to 40 m, given that the partial safety factor can account for its slight unconservatism seen for FTQC A.

Note that the optimised parameters C_m and α_G from set 1 can be used to slightly increase the buckling resistance, but caution should be exercised, as this must not be done in regions where the method is unconservative. Furthermore, the new expressions should ideally be validated experimentally before use.

As mentioned previously, based on what is observed in Figure 7.1, there is room for improvement of the method for lengths greater than approximately 30 m. However, this would require a complete reformulation of the method to ensure that appropriate expressions are also obtained for the boundary range values η_0, η_p, $\overline{\lambda}_{,0}$, and β. Unfortunately, this was not possible, as the investigated geometries did not provide numerical results that could map a capacity curve for specific Ω values, which is essential for determining the boundary range values.

It is worth noting that due to the ongoing improvements in fabrication quality within the wind industry, geometric imperfections are being reduced. Today, monopiles are manufactured in such a high quality that they often surpass the requirements of FTQC A, as Vattenfall has given insight about. As seen in the results presented earlier in the report, the numerical and analytical values align more closely when the imperfection amplitude is reduced. This means that smaller deviations can be expected if the tolerance levels achieved in monopile manufacturing are taken into account. However, in the current method, it is not permitted to define a custom value for the fabrication tolerance quality Q. There are both advantages and drawbacks to permitting a user-defined Q value. The immediate advantage is that it allows for the calculation of higher buckling resistances. The main drawback is that the analytical method may become too unconservative if Q exceeds 40, as concluded from the trend observed in Figure 6.20 for FTQC A, B, and C. In this trend, the method shifts from being conservative for FTQC C to becoming unconservative in certain areas for FTQC A. However, higher Q values have not been investigated in this project, but it would be interesting to explore this in more depth to assess whether the method is compatible with such a modification.

Lastly, it should be noted that analytical methods are generally expected to provide conservative estimates of structural resistance. However, this is not the case for the present method, as the capacity curve parameters are explicitly derived from numerical results.

This page is intentionally left blank.

8 Conclusion

As stated in the introduction, there is a notion in the wind industry that the currently used analytical buckling verification methods might be overly conservative for wind turbine supporting structures such as monopiles. In light of that, the present thesis set out to investigate the appropriateness of the analytical buckling verification methods in EN 1993-1-6 to typical monopiles and to potentially optimise some of the expressions with respect to geometry, boundary conditions and geometric imperfections. Focus was primarily directed towards the novel reference resistance design method in the standard's Annex E, developed for cylinders in uniform global bending. Four conditions in monopiles were identified in section 3.1 as likely causes of conservatism due to their deviation from the assumptions behind the analytical method, namely, the radius-to-thickness ratios, the global support conditions, the internal force distributions and the extent of geometric imperfections. The investigations involved 5 577 numerical calculations of different types and led to the following findings.

- The method can realistically predict the characteristic buckling moment resistance also for cylinders with $r/t < 50$, even though it is formally limited to $50 \leq r/t \leq 2\,000$. However, in most cases, it provides slightly unconservative results. The relative error in the method for typical monopile geometries varies between -4.9% and 6.6%.

- Global support conditions only have a limited influence on the characteristic buckling moment resistance, and the method provides a good overall fit to cantilever cylinders, even though it was developed for cylinders supported at both ends. Based on a brief study comparing numerical results for clamped and cantilever cylinders, the relative difference varies between -2.6% and 2.3% for typical monopile geometries.

- Considering a more realistic linearly increasing bending moment distribution in the cylinder instead of a uniform one leads to a significant increase in the characteristic buckling moment resistance. For cylinders with a typical monopile geometry in FTQC A, the relative increase varies between 7.0% and 12.3%.

- Limiting the circumferential extent of a dimple has a considerable effect on the characteristic buckling moment resistance; however, this effect reduces with decreasing r/t ratio and increasing quality parameter. For cylinders with a typical monopile geometry in FTQC A, the highest relative deviation between models with a full-circumferential and a limited dimple is 7.1%, but the analytical method still provides unconservative results in many cases.

Based on these findings, the highest potential for optimising the analytical method for typical monopiles lies in the reformulation of the capacity curve parameters so that they can account for different bending moment distributions. The first step towards

achieving that has been taken in section 6.1, where a new expression is proposed for the parameter C_m, which can take a linearly increasing bending moment distribution into account. Furthermore, a brief investigation has been conducted aiming to identify the most critical position of a dimple along the cylinder, together with a crude attempt to modify the analytically calculated buckling reduction factor. Hopefully, this work, together with other studies within the topic, will provide valuable input for future research.

Bibliography

[1] D. Kallehave, B. W. Byrne, C. LeBlanc Thilsted, and K. K. Mikkelsen, "Optimization of monopiles for offshore wind turbines," *Philosophical Transactions of the Royal Society A: Mathematical, Physical and Engineering Sciences*, vol. 373, no. 2035, p. 20 140 100, Feb. 28, 2015, ISSN: 1364-503X, 1471-2962. DOI: 10.1098/rsta.2014.0100.

[2] J. D. Winkel, "Large diameter dolphin piles: The effect of the inner soil on their local buckling resistance," 2016. URL: Link.

[3] "Monopiles - CS Wind Offshore." (), URL: Link (visited on 03/20/2025).

[4] M. Salvadori and R. Heller, *Structure in Architecture* (Prentice-Hall International Series in Architecture). Englewood Cliffs, NJ, USA: Prentice-Hall, 1963.

[5] S. Jerath, *Structural Stability Theory and Practice: Buckling of Columns, Beams, Plates, and Shells*. Hoboken, NJ, USA: John Wiley & Sons, 2021, ISBN: 9781119694502.

[6] C. H. Yoo and S. C. Lee, *Stability of Structures: Principles and Applications*. Oxford, UK: Butterworth-Heinemann, 2011, ISBN: 9780123851222.

[7] A. Chajes, *Principles of Structural Stability Theory* (Civil Engineering and Engineering Mechanics Series). Englewood Cliffs, NJ, USA: Prentice-Hall, 1974, ISBN: 9780137099641.

[8] CEN/TC 250, *Eurocode 3 - Design of steel structures - Part 1-1: General rules and rules for buildings* (EN 1993-1-1), 2nd ed. Brussels, Belgium: European Committee for Standardization, 2022.

[9] Dr. Minas E. Lemonis. "Column buckling," calcresource. (Mar. 1, 2024), URL: Link (visited on 02/26/2025).

[10] eigenplus. "Flexural torsional buckling and lateral torsional buckling," LinkedIn. (Jan. 2025), URL: Link (visited on 02/26/2025).

[11] CEN/TC 250, *Eurocode 3 - Design of steel structures - Part 1-5: Plated structural elements* (EN 1993-1-5), 2nd ed. Brussels, Belgium: European Committee for Standardization, 2024.

[12] CEN/TC 250, *Eurocode 3 - Design of steel structures - Part 1-6: Strength and Stability of Shell Structures* (EN 1993-1-6), 1st ed. Brussels, Belgium: European Committee for Standardization, 2007.

[13] G. Gerard and H. Becker, "Handbook of Structural Stability Part I: Buckling of Flat Plates," New York University, Washington, Technical Note NACA TN 3781, Jul. 1, 1957. DOI: 10.2172/4343548.

[14] A. Meidell, "Computer aided material selection for circular tubes designed to resist axial crushing," *Thin-Walled Structures*, vol. 47, no. 8, pp. 962–969, Aug. 2009, ISSN: 02638231. DOI: 10.1016/j.tws.2009.02.003.

[15] ECCS TC8 TWG 8.4, *Buckling of Steel Shells: European Design Recommendations* (ECCS 125), 5th ed., J. M. Rotter and H. Schmidt, Eds. Brussels: European Convention for Constructional Steelwork, 2008.

[16] A. Taras, J. Nseir, and N. Boissonnade, "Cylindrical Shell Buckling Strength according to the "Overall Method" of Eurocode 3 - Background and applicability to the design of high strength steel slender circular hollow sections," presented at the Structural Stability Research Council Annual Stability Conference, Toronto, Canada: SSRC, Mar. 2014.

[17] J. M. Rotter, "Cylindrical shells under axial compression," in *Buckling of Thin Metal Shells*, London: Spon Press, 2004, pp. 42–87, ISBN: 9780419241904.

[18] N. Yamaki, *Elastic Stability of Circular Cylindrical Shells* (North-Holland Series in Applied Mathematics and Mechanics v. 27). Amsterdam: North-Holland, 1984, ISBN: 9780444868572.

[19] CEN/TC 250, *Eurocode 3 - Design of steel structures - Part 1-6: Strength and Stability of Shell Structures* (draft, prEN 1993-1-6), 2nd ed. Brussels, Belgium: European Committee for Standardization, 2023.

[20] A. J. Sadowski, M. T. Morata, L. Kathirkamanathan, M. Seidel, and J. M. Rotter, "On the existing test dataset of isotropic cylindrical metal shells under axial compression and the design of modern metal civil engineering shells," *Structural Safety*, vol. 102, p. 102 285, May 2023, ISSN: 01674730. DOI: 10.1016/j.strusafe.2022.102285.

[21] J. M. Rotter, A. J. Sadowski, and L. Chen, "Nonlinear stability of thin elastic cylinders of different length under global bending," *International Journal of Solids and Structures*, vol. 51, no. 15, pp. 2826–2839, Aug. 2014, ISSN: 00207683. DOI: 10.1016/j.ijsolstr.2014.04.002.

[22] O. Fajuyitan, A. J. Sadowski, and J. M. Rotter, "A study of imperfect cylindrical steel tubes under global bending and varying support conditions," presented at the Eighth International Conference on ADVANCES IN STEEL STRUCTURES, Lisbon, Portugal, 2015.

[23] CEN/TC 250, *Eurocode 3 - Design of steel structures - Part 1-6: Strength and Stability of Shell Structures* (EN 1993-1-6:2007/A1), 1st ed. Brussels, Belgium: European Committee for Standardization, 2017.

[24] DNV GL, *Buckling strength of shells* (Recommended practice — DNVGL-RP-C202). DNV GL AS, 2019.

[25] A. J. Sadowski and A. Filippidis, "The capacity curve framework of EN 1993-1-6 (2025): Cylindrical shells under uniform meridional compression vs uniform bending," *Journal of Constructional Steel Research*, vol. 225, p. 109 167, 2025, ISSN: 0143-974X. DOI: https://doi.org/10.1016/j.jcsr.2024.109167.

[26] CEN/TC 250, *Eurocode 3 - Design of steel structures - Part 1-14: Design assisted by finite element analysis* (draft, prEN 1993-1-14), 2nd ed. Brussels, Belgium: European Committee for Standardization, 2023.

[27] J. Rotter, "The new method of reference resistance design for shell structures," *Proc. SDSS 2016, International Colloquium on Stability and Ductility of Steel Structures*, pp. 623–630, Jan. 2016.

[28] J. Wang, O. K. Fajuyitan, M. A. Orabi, J. M. Rotter, and A. J. Sadowski, "Cylindrical shells under uniform bending in the framework of reference resistance design," *Journal of Constructional Steel Research*, vol. 166, p. 105 920, Mar. 2020, ISSN: 0143974X. DOI: 10.1016/j.jcsr.2019.105920.

[29] A. Albers and S. Liborius Bruun, "Assessment of stability in large thin-walled tubular steel structures," Master's thesis, Aalborg University, Aalborg, Jun. 10, 2021.

[30] ANSYS, Inc., *Ansys Mechanical Enterprise Academic Research*, version 2024 R1.

[31] ANSYS, Inc., *Ansys Mechanical Enterprise Academic Student*, version 2024 R2.

[32] A. Kaszynski *et al.*, *PyMAPDL*, version 0.69.2, Jan. 22, 2024. URL: Link.

[33] SDU eScience Center, *UCloud*, version 2025.2.0. URL: Link.

[34] J. Teng and C. Song, "Numerical models for nonlinear analysis of elastic shells with eigenmode-affine imperfections," *International Journal of Solids and Structures*, vol. 38, no. 18, pp. 3263–3280, May 2001, ISSN: 00207683. DOI: 10.1016/S0020-7683(00)00222-5.

[35] J. M. Rotter and J.-G. Teng, "Elastic stability of cylindrical shells with weld depressions," *Journal of Structural Engineering*, vol. 115, no. 5, pp. 1244–1263, May 1989, ISSN: 0733-9445, 1943-541X. DOI: 10.1061/(ASCE)0733-9445(1989)115:5(1244).

[36] K. K. Yadav and S. Gerasimidis, "Imperfection insensitivity of thin wavy cylindrical shells under axial compression or bending," *Journal of Applied Mechanics*, vol. 87, no. 4, p. 041 003, Apr. 1, 2020, ISSN: 0021-8936, 1528-9036. DOI: 10.1115/1.4045741.

[37] A. J. Sadowski *et al.*, "8-MW wind turbine tower computational shell buckling benchmark. part 1: An international 'round-robin' exercise," *Engineering Failure Analysis*, vol. 148, p. 107 124, Jun. 2023, ISSN: 13506307. DOI: 10.1016/j.engfailanal.2023.107124.

[38] ANSYS, Inc. "Mechanical APDL 2024 R2," Ansys Product Help. (), URL: Link (visited on 04/16/2025).

[39] CEN/TC 459/SC 3, *Hot rolled products of structural steel - Part 2: Techinical delivery conditions for non-alloy structural steels* (EN 10025-2). Brussels, Belgium: European Committee for Standardization, 2019.

[40] P. O'Kelly-Lynch, C. Long, F. D. McAuliffe, J. Murphy, and V. Pakrashi, "Structural design implications of combining a point absorber with a wind turbine monopile for the east and west coast of ireland," *Renewable and Sustainable Energy Reviews*, vol. 119, p. 109 583, Mar. 2020, ISSN: 13640321. DOI: 10.1016/j.rser.2019.109583.

[41] A. Roth *et al.*, "Stiffness analysis of load-bearing structures," Aalborg University, Aalborg, Dec. 21, 2023.

[42] A. J. Sadowski and J. M. Rotter, "Solid or shell finite elements to model thick cylindrical tubes and shells under global bending," *International Journal of Mechanical Sciences*, vol. 74, pp. 143–153, Sep. 2013, ISSN: 00207403. DOI: 10.1016/j.ijmecsci.2013.05.008.

[43] DNV GL, *Determination of structural capacity by non-linear finite element analysis methods* (Recommended practice — DNVGL-RP-C208). DNV GL AS, 2016.

[44] A. J. Sadowski, O. K. Fajuyitan, and J. Wang, "A computational strategy to establish algebraic parameters for the reference resistance design of metal shell structures," *Advances in Engineering Software*, vol. 109, pp. 15–30, Jul. 2017, ISSN: 09659978. DOI: 10.1016/j.advengsoft.2017.02.012.

[45] K. Dahl Schiøttz Damsgaard, "Non-linear finite element analysis," Aalborg University, 2024.

[46] P. Seide and V. I. Weingarten, "On the buckling of circular cylindrical shells under pure bending," *Journal of Applied Mechanics*, vol. 28, no. 1, pp. 112–116, Mar. 1, 1961, ISSN: 0021-8936, 1528-9036. DOI: 10.1115/1.3640420.

[47] The MathWorks, Inc., *Curve Fitting Toolbox*, version 23.2, 2023.

[48] The MathWorks, Inc., *MATLAB*, version R2023b, 2023.

A Analytical Methods in EN 1993-1-6

The aim of this appendix is to describe in detail how the buckling reduction factor χ is determined in EN 1993-1-6 for shell structures, where geometric nonlinearity, plasticity and imperfections are taken into account. Two relevant methods are presented for unstiffened cylindrical shells, one from Annex D and the other from Annex E. The calculation method in Annex D is stress-based and assumes uniform axial compression in the shell wall, whereas the one in Annex E is resistance-based for cylinders under uniform global bending. First, the capacity curve parameters calculated identically in both methods are presented, followed by the expressions specific for each method.

The relative length of a shell can be characterised in several ways. In EN 1993-1-6, the two relative length parameters ω and Ω are chosen since they vary linearly with the length L and normalise it relative to the radius r and wall thickness t, which control the behaviour of the shell. The expressions are given in (A.1) and (A.2).

$$\omega = \frac{L}{r}\sqrt{\frac{r}{t}} = \frac{L}{\sqrt{rt}} \tag{A.1}$$

$$\Omega = \frac{L}{r}\sqrt{\frac{t}{r}} = \omega\frac{t}{r} \tag{A.2}$$

where ω is the first relative length
Ω is the second relative length
L is the length of the cylinder
r is the radius of cylinder middle surface
t is the thickness of the shell

The buckling reduction factor χ depends on the value of the relative slenderness $\overline{\lambda}$ as shown in (A.3). χ can hereafter be calculated using different parameters.

$$\begin{aligned}
\chi &= \chi_h - \frac{\overline{\lambda}}{\overline{\lambda}_0}(\chi_h - 1) && \text{for } \overline{\lambda} \le \overline{\lambda}_0 \\
\chi &= 1 - \beta\left(\frac{\overline{\lambda} - \overline{\lambda}_0}{\overline{\lambda}_p - \overline{\lambda}_0}\right)^{\eta} && \text{for } \overline{\lambda}_0 < \overline{\lambda} < \overline{\lambda}_p \\
\chi &= \frac{\alpha}{\overline{\lambda}^2} && \text{for } \overline{\lambda}_p \le \overline{\lambda}
\end{aligned} \tag{A.3}$$

where χ is the buckling reduction factor
χ_h is the buckling reduction factor in the hardening zone at $\overline{\lambda} = 0$
$\overline{\lambda}$ is the relative slenderness of the shell
$\overline{\lambda}_0$ is the squash limit relative slenderness (value of $\overline{\lambda}$ above which resistance reduction due to instability or geometric change occurs)
β is the plastic range factor in buckling interaction

where $\overline{\lambda}_p$ is the plastic limit relative slenderness (value of $\overline{\lambda}$ below which plasticity affects the stability)
η is the interaction exponent
α is the elastic buckling reduction factor

The plastic limit relative slenderness is calculated using (A.4).

$$\overline{\lambda}_p = \sqrt{\frac{\alpha}{1-\beta}} \tag{A.4}$$

The expression for the interaction exponent η in (A.5) applies to both methods; however, the individual factors are determined differently in each of them. The determination of all the factors is described in detail for each method in its respective section.

$$\eta = \frac{\overline{\lambda}(\eta_p - \eta_0) + \overline{\lambda}_p \eta_0 - \overline{\lambda}_0 \eta_p}{\overline{\lambda}_p - \overline{\lambda}_0} \tag{A.5}$$

where η_p is the value of the interaction exponent at $\overline{\lambda} = \overline{\lambda}_p$
η_0 is the value of the interaction exponent at $\overline{\lambda} = \overline{\lambda}_0$

The imperfection amplitude δ_0 is given in (A.6).

$$\frac{\delta_0}{t} = \frac{1}{Q}\sqrt{\frac{r}{t}} \tag{A.6}$$

where δ_0 is the imperfection amplitude used in design calculation
Q is the fabrication tolerance quality parameter

Here, the fabrication tolerance quality parameter Q depends on the specified fabrication tolerance quality class, as shown in Table A.1. The tolerances match those specified in the execution standard EN 1090.

Table A.1: Values of fabrication tolerance quality parameters

Fabrication tolerance quality class	Description	Q
Class A	Excellent	40
Class B	High	25
Class C	Normal	16

In the following sections, the parameters used for each method are distinguished by subscripts. The method in Annex D, based on a cylinder under uniform axial compression, uses the subscript 'x', while the method in Annex E, based on a cylinder under uniform global bending, uses the subscript 'b'.

A.1 Annex D: Stress-based methods

The method in Annex D is stress-based buckling design, where the characteristic axial buckling stress $\sigma_{x,Rk}$ is obtained by multiplying the characteristic yield strength f_{yk} by the buckling reduction factor as shown in (A.7).

$$\sigma_{x,Rk} = \chi_x f_{yk} \tag{A.7}$$

In the following section, a description of the determination of the necessary parameters to determine the buckling reduction factor is provided. Both methods in EN 1993-1-6:2007 and prEN 1993-1-6:2023 are presented. Some aspects remain unchanged for both methods. Any differences are clearly highlighted.

The relative slenderness depends on the characteristic yield strength f_{yk} and the elastic critical axial buckling stress $\sigma_{x,cr}$, as shown in (A.8).

$$\overline{\lambda}_x = \sqrt{\frac{f_{yk}}{\sigma_{x,cr}}} \tag{A.8}$$

A.1.1 Critical Axial Buckling Stress

The elastic critical axial stress is given in (A.9).

$$\sigma_{x,cr} = \frac{1}{\sqrt{3\,(1-\nu^2)}} E C_x \frac{t}{r} = 0.605 E C_x \frac{t}{r} \tag{A.9}$$

where E is Young's modulus
ν is Poisson's ratio
C_x is a coefficient in axial compression critical buckling resistance

Disregarding the coefficient C_x, the expression is derived using classical linear Donnell-type shell buckling theory applied to medium-length cylinders under uniform axial compression. The coefficient C_x accounts for whether it is a short or long cylinder. The classification of the length of the cylinders is given below:

	EN 1993-1-6:2007	prEN 1993-1-6:2023
Short cylinder	$\omega \leq 1.7$	
Medium-length cylinder	$1.7 \leq \omega \leq 0.5\frac{r}{t}$	$1.7 \leq \omega \leq 1.43\frac{r}{t}$
Long cylinder	$\omega > 0.5\frac{r}{t}$	$\omega > 1.43\frac{r}{t}$

The coefficient can be calculated as shown in (A.10) depending on the classification of the length. However, in prEN 1993-1-6:2023, long cylinders are calculated as medium-length cylinders.

Short cylinder	$C_x = 1.36 - \frac{1.83}{\omega} + \frac{2.07}{\omega^2}$	
Medium length cylinder	$C_x = 1$	
Long cylinder	$C_x = C_{x,N}$	(only in EN 1993-1-6:2007)

(A.10)

$C_{x,N}$ can be determined as shown in (A.11) where C_{xb} is a parameter depending on the boundary conditions and can be found using Table D.1 in EN 1993-1-6.

$$C_{x,N} = \max \begin{cases} 0.6 \\ 1 + \dfrac{0.2}{C_{xb}} \left(1 - 2\omega \dfrac{t}{r}\right) \end{cases} \tag{A.11}$$

The reduction of the buckling stress is represented by the parameter $C_{x,N}$. The extent of the reduction depends on whether the edges of the cylinder are axially restrained or not, which is covered by the parameter C_{xb}.

A.1.2 Axial Buckling Parameters

A.1.2.1 EN 1993-1-6:2007

The axial elastic imperfection factor α_x is a function of the imperfection amplitude δ_0/t, as shown below.

$$\alpha_x = \frac{0.62}{1 + 1.91(\delta_0/t)^{1.44}} \tag{A.12}$$

In this version of the Eurocode, the axial squash limit slenderness λ_{x0}, the plastic range factor β_x and the interaction exponent η_x are fixed values as given in (A.13).

$$\overline{\lambda}_{x0} = 0.2 \qquad \beta_x = 0.6 \qquad \eta_x = 1.0 \tag{A.13}$$

These parameters are used to determine the axial buckling reduction factor χ_x. It should be noted that $\chi_x = 1$ for $\overline{\lambda}_x \leq \overline{\lambda}_{x0}$, since hardening is ignored.

A.1.2.2 prEN 1993-1-6:2023

A significant difference between EN 1993-1-6:2007 and prEN 1993-1-6:2023 is that the plastic range factor β_x and interaction exponent η_x are not constants. The plastic range factor depends on the imperfection amplitude, as shown in (A.14).

$$\beta_x = 1 - \frac{0.75}{1 + 1.1\delta_0/t} \tag{A.14}$$

The interaction exponent is calculated using equation (A.5) where the values η_{x0} and η_{xp} are given in (A.15).

$$\begin{aligned} \eta_{x0} &= 1.35 - 0.10\frac{\delta_0}{t} \\ \eta_{xp} &= \frac{1}{0.45 + 0.72\delta_0/t} \end{aligned} \tag{A.15}$$

The value of the squash limit slenderness is reduced to $\overline{\lambda}_{x0} = 0.1$. This affects the size of the elastic-plastic zone. The axial elastic imperfection factor α_x now consists of two contributions, as shown in (A.16).

$$\alpha_x = \alpha_{xG}\alpha_{xI} \tag{A.16}$$

The factor α_{xG} takes geometric nonlinearity into account and has a fixed value of $\alpha_{xG} = 0.83$, whereas α_{xI} takes geometric imperfections into account and is calculated as per (A.17).

$$\alpha_{xI} = \frac{1}{1 + 2.2(\delta_0/t)^{0.75}} \tag{A.17}$$

Lastly, the hardening limit χ_{xh} is introduced, relevant for thick-walled cylinders.

$$\chi_{xh} = 1.10 \tag{A.18}$$

A.2 Annex E: Resistance-based methods

The method in Annex E is a resistance-based buckling verification for cylinders under uniform global bending, where the characteristic buckling moment resistance M_{Rk} is calculated as the product of the buckling reduction factor and the reference plastic moment resistance, as shown in (A.19).

$$M_{Rk} = \chi_b M_{pl} \qquad \text{or} \qquad M_{Rk} = \chi_b M_{pl,I} \tag{A.19}$$

Note that different values of the reference plastic moment resistance are used in the current standard EN 1993-1-6/A1:2017 and its future edition prEN 1993-1-6:2023, as described in the following. Other parameters differ in the two editions as well, and they are also highlighted below.

A.2.1 Bending moment resistances and slenderness

The *reference plastic moment resistance* used as a normalising parameter for the capacity curve is defined as shown in (A.20), as a lower-bound approximation using a plastic section modulus, where the second term, only containing the thickness, is disregarded. As such, it gives a close approximation in cases with high radius-to-thickness ratios and is suitable for most cylindrical shells used in practice.

$$M_{pl} = 4r^2 t f_{yk} \tag{A.20}$$

To be able to define the buckling resistance of very imperfect cylinders in the traditional way and maintain the physical meaning of the factors that describe the capacity curve, it is necessary to include the effect of imperfections in the normalising parameter, which in case of global bending is the reference plastic moment resistance, M_{pl}. Therefore, a reduced reference plastic moment resistance accounting for imperfections is introduced in the future version of Annex E, calculated as given below. In that way, imperfections are included in both the relative slenderness and the buckling reduction factor.

$$M_{pl,I} = \left(0.2 + \frac{0.8}{1 + 0.23(\delta_0/t)^2}\right) M_{pl} \tag{A.21}$$

The *elastic critical moment* in the current version of Annex E is defined as shown in (A.22). In the future version, only the simplified expression of the approximate value is specified with a note stating that the precise value is somewhat affected by the end boundary conditions, increasing slightly at shorter lengths. That effect can be taken

into account through the coefficient C_m, which is defined as shown in (A.23). The value of C_m varies between 1 and approximately 1.15 for most unstiffened cylindrical shells in practical application. For wind turbine monopiles, the upper limit is much lower, approximately 1.01, resulting in only a slight increase of M_{cr}.

$$M_{cr} = \frac{\pi C_m}{\sqrt{3(1-\nu)^2}} Ert^2 \approx 1.90 Ert^2 \tag{A.22}$$

$$C_m = 1 + \frac{4}{\omega^2} \tag{A.23}$$

Based on the reference resistances, the *relative slenderness* in bending is calculated as shown below, according to EN 1993-1-6/A1:2017 on the left and prEN 1993-1-6:2023 on the right.

$$\overline{\lambda}_b = \sqrt{\frac{M_{pl}}{M_{cr}}} \qquad \text{or} \qquad \overline{\lambda}_b = \sqrt{\frac{M_{pl,I}}{M_{cr}}} \tag{A.24}$$

A.2.2 Factors for range limits

The *plastic range factor* β_b and the *squash limit relative slenderness* $\overline{\lambda}_{b0}$ for cylinders in bending are calculated using (A.25) and (A.26), respectively. Note that the expressions from prEN 1993-1-6:2023 (on the right) provide more realistic results due to the inclusion of additional dependence on length and, for $\overline{\lambda}_{b0}$, also on imperfection amplitude. Both factors are computed ignoring the stiffening effect of the combination of imperfections and ovalisation, since these effects individually reduce the stiffness, and it cannot be ensured that they occur at the same place.

$$\beta_b = 1 - \frac{0.6}{1 + 1.2(\delta_0/t)^{0.8}} \qquad \text{or} \qquad \beta_b = 1 - \frac{0.785}{1 + 1.3\sqrt{\delta_0/t}} f_\Omega \tag{A.25}$$

$$\overline{\lambda}_{b0} = 0.3 \qquad \text{or} \qquad \overline{\lambda}_{b0} = \frac{0.3}{1 + 0.4\sqrt{\delta_0/t}} f_\Omega \tag{A.26}$$

where f_Ω is a length function defined as

$$f_\Omega = \min \begin{cases} 0.7 + \dfrac{0.44}{1 + 1.66\Omega^{1.87}} \\ 1.0 \end{cases} \tag{A.27}$$

A.2.3 Factors for elastic buckling

The *elastic buckling reduction factor* α_b consists of two contributions in both editions of the standard, as shown below, although the contributing parameters are calculated differently.

$$\alpha_b = \alpha_{bG} \alpha_{bI} \tag{A.28}$$

The *geometric reduction factor* α_{bG} in EN 1993-1-6/A1:2017 is defined as a function of the relative length, as shown in (A.29). The theoretical background of the expressions is briefly described in section 2.3.2 based on a study by Rotter et al. [21].

$$\alpha_{bG} = \begin{cases} 1.93 - 0.5(\omega - 3.8)^2 - 0.44(\omega - 3.8)^3 & \text{for short: } 3 \leq \omega < 4.8 \\ 0.85 + 0.029(\omega - 7.1)^2 & \text{for med.: } 4.8 \leq \omega < 8.6 \\ 0.92 & \text{for med.: } 8.6 \leq \omega < 0.5(r/t) \\ 1.07\dfrac{1 - 0.22\Omega + 0.061\Omega^{2.94}}{1 + 0.12\Omega^{2.94}} & \text{for trans.: } 0.5 \leq \Omega < 7.0 \\ 0.516 & \text{for long: } \Omega \geq 7.0 \end{cases} \tag{A.29}$$

In prEN 1993-1-6:2023, the expressions for α_{bG} are simplified to the forms shown in (A.30), based on a study by Wang et al. [28].

$$\alpha_{bG} = \begin{cases} 0.9 & \text{for } \Omega < 0.5 \\ 0.5 + (0.38\sin(0.85\Omega) + 0.48\cos(0.85\Omega))\mathrm{e}^{-0.8\Omega} & \text{for } \Omega \geq 0.5 \end{cases} \tag{A.30}$$

The other contribution is from the *imperfection reduction factor* α_{bI}, as shown in (A.31). Similarly to the factors for range limits, notice the additional dependency on the relative length, indicating that α_{bI} not only accounts for geometric imperfections but also geometric nonlinearity as a result of the imperfections.

$$\alpha_{bI} = \frac{1}{1 + 2\left(\dfrac{\delta_0}{t}\right)^{0.8}} \qquad \text{or} \qquad \alpha_{bI} = \frac{1}{1 + \left(0.7 + \dfrac{1.05}{1 + 0.42\Omega^{2.8}}\right)\left(\dfrac{\delta_0}{t}\right)^{0.7}} \tag{A.31}$$

A.2.4 Factors for inelastic buckling

The *interaction exponent* η_b in EN 1993-1-6/A1:2017 is defined as shown in (A.32).

$$\eta_b = 0.65 + 0.2(\delta_0/t) \tag{A.32}$$

In prEN 1993-1-6:2023, the expression is modified to the one shown earlier in (A.5), using the values at the boundaries η_{b0} and η_{bp} defined as shown below.

$$\eta_{b0} = \begin{cases} 1.0 & \text{for } \Omega < 4.5 \\ 0.133\,(12 - \Omega) & \text{for } 4.5 \leq \Omega < 7.5 \\ 0.6 & \text{for } 7.5 \leq \Omega \end{cases} \tag{A.33}$$

$$\eta_{bp} = \begin{cases} 0.08\,(12 - \Omega) & \text{for } \Omega < 5 \\ 0.16\,(12 - \Omega) & \text{for } \Omega \geq 5 \end{cases} \tag{A.34}$$

Lastly, the hardening limit χ_{bh}, mainly relevant for thick-walled cylinders, is set to a constant in both editions.

$$\chi_{bh} = 1.0 \qquad \text{or} \qquad \chi_{bh} = 1.05 \tag{A.35}$$

This page is intentionally left blank.

B Codes

This appendix contains the Python code for a single numerical analysis, used as a master script to construct batch scripts for each analysis type. For clarity and a better overview, the script is divided into the following parts:

Program code B.1: Module import and launch

```
import math as mt
import numpy as np
import matplotlib.pyplot as plt

from ansys.mapdl.core import launch_mapdl
mapdl = launch_mapdl(nproc=4, additional_switches='-dmp')
mapdl.mute = True
print(mapdl)
```

Program code B.2: Parameter definition

```
# General constants

pi = mt.pi


# Geometric parameters

L = 10.00                       # Length of cylinder [m]
r = 4.000                       # Middle radius of cylinder [m]
t = 0.080                       # Uniform thickness of cylinder [m]
CylSize = 1                     # Size of cylinder (1 - half, 2 - full)

Lambda = 2.444*mt.sqrt(r*t)     # Linear meridional bending half-wavelength [m]


# Geometric imperfection parameters

ImpForm = "none"                # Imperfection form (none, full - full-circ., lmtd - limited)
Q = 40                          # Fabrication quality parameter [-]
zdimp = L/2                     # z coordinate of dimple [m] (max. L/2, always on lower half)

d0 = t/Q*mt.sqrt(r/t)           # Imperfection amplitude [m]


# Material parameters

```

```
E = 200000                      # Young's modulus [MPa]
nu = 0.3                        # Poisson's ratio [-]
fy = 315                        # Yield strength [MPa]
Et = 0.000*E                    # Tangent modulus [MPa]

Ep = E*Et/(E-Et)                # Plastic tangent modulus [MPa]


# Mesh parameters

Quad = 1                        # Quadratic elements (0 - no, 1 - yes)
NumElem = 5                     # Number of elements per Lambda [-]
MaxESize = 0.25                 # Max. allowable element size [m]

ESize = min(Lambda/NumElem, MaxESize)   # Desired element size [m]
nm = mt.ceil(pi*r/ESize/5)*5*CylSize    # Number of elements along the circumference [-]
nn = mt.ceil(L/ESize/4)*4               # Number of elements along the length [-]


# Model parameters

LoadApl = "for"          # Load application (def - deformation control, for - force control)
StatSys = "cntl"         # Static system of the model (cntl - cantilever, clmp - clamped)


# Analysis parameters

AnaType = "LBA"          # Analysis type (LBA, MNA, GNA, GMNA, imperfection can be set above)
NumMode = 2              # Number of buckling modes in LBA
SolMthd = "ALM"          # Solution method in NAs (NRM - Newton-Raphson, ALM - Arc-length)

if AnaType == "GNA":     # Number of initial substeps in NAs
    NumSbst = 200
elif AnaType == "MNA":
    NumSbst = 30
elif AnaType == "GMNA":
    if r/t < 200:
        NumSbst = 100
    else:
        NumSbst = 200


# Analytical resistances of full cylinder

Ncl = 2*pi*E*t*t/mt.sqrt(3*(1-nu**2))   # Classical elastic critical compression [MN]
Npl = 2*pi*r*t*fy                       # Reference plastic compression resistance [MN]
print("Ncl = ", Ncl)
print("Npl = ", Npl)

Mcl = E*r*t*t*pi/mt.sqrt(3*(1-nu**2))   # Classical elastic critical moment [MNm]
Mcr = 2*E*r*t*t                         # Approx. elastic critical moment [MNm]
Mpl = (4*r*r*t+1/3*t**3)*fy             # Reference plastic moment resistance [MNm]
print("Mcl = ", Mcl)
print("Mcr ~= ", Mcr)
print("Mpl = ", Mpl)


# Applied loads

  # NOTE: Application of shear is only supported for cantilever static system!

LoadType = "M"           # Type of applied load (N - axial, M - moment, V - shear with M)
Psi = 0.5                # End moment ratio (when LoadType = "V") [-]

```

```
  # Prescribed deformations (deformation control)
uX = 0                  # Transverse end displacement [m]
uZ = 0                  # Axial end displacement [m]
rY = 0                  # End rotation [rad]

  # Prescribed forces (force control)
if AnaType == "LBA":                            # Applied loads in LBA
    if LoadType == "N":
        N = CylSize/2                              # Axial compression [MN]
    elif LoadType == "M":
        M = CylSize/2                              # Bending moment [MNm]
    elif LoadType == "V":
        V = CylSize/2*(1-Psi)/L                    # Shear force [MN]
        M = CylSize/2*Psi                          # Bending moment [MNm]
elif AnaType =="GNA":                           # Applied loads in GNA/GNIA
    if LoadType == "N":
        N = CylSize/2*Ncl                          # Axial compression [MN]
    elif LoadType == "M":
        M = CylSize/2*Mcr                          # Bending moment [MNm]
elif AnaType == "MNA":                          # Applied loads in MNA/MNIA
    if LoadType == "N":
        N = CylSize/2*Npl                          # Axial compression [MN]
    elif LoadType == "M":
        M = CylSize/2*Mpl                          # Bending moment [MNm]
elif AnaType =="GMNA":                          # Applied loads in GMNA/GMNIA
    if LoadType == "N":
        N = CylSize/2*min(Ncl, Npl)                # Axial compression [MN]
    elif LoadType == "M":
        M = CylSize/2*min(Mcl, Mpl)                # Bending moment [MNm]
    elif LoadType == "V":
        V = CylSize/2*(1-Psi)*1.2*min(Mcl, Mpl)/L  # Shear force [MN]
        M = CylSize/2*Psi*1.2*min(Mcl, Mpl)        # Bending moment [MNm]
```

Program code B.3: Model setup

```
# Resetting MAPDL and starting preprocessor

mapdl.clear()
mapdl.prep7()


# Element definition

if Quad == 1:
    mapdl.et(1, "SHELL281")      # 8-noded structural shell (quadratic)
    mapdl.keyopt(1, 8, 2)        # Store data for top, bottom and middle surfaces
else:
    mapdl.et(1, "SHELL181")      # 4-noded structural shell (bilinear)
    mapdl.keyopt(1, 3, 2)        # Full integration with incompatible modes
    mapdl.keyopt(1, 8, 2)        # Store data for top, bottom and middle surfaces

mapdl.et(2, "CONTA177", kop2=2, kop4=0)        # 3D line-to-surface contact element with MPC
mapdl.keyopt(2, 12, 5)                         # Bonded behavior of contact surface
mapdl.et(3, "TARGE170", kop2=1, kop4="111111") # 3D target surface with user-defined DOF
mapdl.keyopt(3, 10, 1)                         # Including stress stiffening effects


# Material definition

mapdl.mp("EX", 1, E)             # Young's modulus of material 1
mapdl.mp("PRXY", 1, nu)          # Poisson's ratio of material 1

if AnaType == "MNA" or AnaType == "GMNA":
```

```
    mapdl.tb("BISO", 1)          # Setting material model to bilinear isotropic hardening
    mapdl.tbdata(1, fy, Ep)      # Setting yield strength and plastic tangent modulus


# Section definition

mapdl.sectype(1, "SHELL")        # Defining a shell section with ID 1
if AnaType == "MNA" or AnaType == "GMNA":
    mapdl.secdata(t, 1, "", 5)   # Setting thickness, material and no. of integration points
else:
    mapdl.secdata(t, 1, "", 3)   # Setting thickness, material and no. of integration points


# Modelling geometry (incl. division for mesh)

if ImpForm == "none":
    mapdl.k(1, 0, 0, 0)          # Defining keypoint 1 at bottom of cylinder axis
    mapdl.k(2, 0, 0, L)          # Defining keypoint 2 at top of cylinder axis
    mapdl.k(3, r, 0, 0)          # Defining keypoint 3 at bottom of middle surface
    mapdl.k(4, r, 0, L)          # Defining keypoint 4 at top of middle surface
    mapdl.l(3, 4)                # Defining line 1 between keypoints 3 and 4
    mapdl.arotat(1, pax1=1, pax2=2, arc=180*CylSize, nseg=5*CylSize) # Rotating line 1

    mapdl.lsel("S", "LINE", "", 1, 4*CylSize+2)
    mapdl.lesize("ALL", ndiv=nn)               # Setting meridional number of elements
    mapdl.lsel("INVE")
    mapdl.lesize("ALL", angsiz=180*CylSize/nm) # Setting circumferential number of elements
    mapdl.lsel("ALL")

elif ImpForm == "full":
    mapdl.k(1, 0, 0, 0)          # Defining keypoint 1 at bottom of cylinder axis
    mapdl.k(2, 0, 0, L)          # Defining keypoint 2 at top of cylinder axis

    kID = [10+i for i in range(1, nn+2)]
    z = np.linspace(0, L, num=nn+1)
    count = 0

    for i in range(0, nn+1):
        w = d0*mt.exp(-pi/Lambda*abs(z[i]-zdimp))*
        ↪  (mt.cos(pi/Lambda*abs(z[i]-zdimp))+mt.sin(pi/Lambda*abs(z[i]-zdimp)))
        mapdl.k(kID[i], r-w, 0, z[i])
        count = count + 1
        if count == 5:
            mapdl.bsplin(kID[i-4], kID[i-3], kID[i-2], kID[i-1], kID[i])
            count = 1

    mapdl.arotat("ALL", pax1=1, pax2=2, arc=180*CylSize, nseg=5*CylSize) # Rotating lines

    mapdl.lsel("S", "LINE", "", 1, nn/4*(4*CylSize+2))
    mapdl.lesize("ALL", ndiv=4)                # Setting meridional number of elements
    mapdl.lsel("INVE")
    mapdl.lesize("ALL", angsiz=180*CylSize/nm) # Setting circumferential number of elements
    mapdl.lsel("ALL")

elif ImpForm == "lmtd":
    mapdl.csys(1)                # Activating cylindrical coordinate system

    z = np.linspace(0, L, num=nn+1)
    theta = np.linspace(0, 180*CylSize, num=nm+1)
    kID = np.arange(1, (nm + 1) * (nn + 1) + 1).reshape(nn + 1, nm + 1)

    for i in range(0, nn+1):
        countm = 0
        for j in range(0, nm+1):
```

```
            w = d0*mt.exp(-pi/Lambda*abs(z[i]-zdimp))*
            ↪  (mt.cos(pi/Lambda*abs(z[i]-zdimp))+mt.sin(pi/Lambda*abs(z[i]-zdimp)))*
            ↪  mt.exp(-pi**2*r/Lambda*abs(theta[j]/180-1))*
            ↪  (mt.cos(pi**2*r/Lambda*abs(theta[j]/180-1))+
            ↪  mt.sin(pi**2*r/Lambda*abs(theta[j]/180-1)))
            mapdl.k(kID[i][j], r-w, theta[j]+180, z[i])
            countm = countm + 1
            if countm == 6:
                mapdl.bsplin(kID[i][j-5], kID[i][j-4], kID[i][j-3], kID[i][j-2], kID[i][j-1],
                ↪  kID[i][j])
                countm = 1

    for j in range(0, nm+1):
        countn = 0
        for i in range(0, nn+1):
            countn = countn + 1
            if countn == 5:
                mapdl.bsplin(kID[i-4][j], kID[i-3][j], kID[i-2][j], kID[i-1][j], kID[i][j])
                countn = 1

    for i in range(0, nn):
        for j in range(0, nm):
            mapdl.a(kID[i][j], kID[i][j+1], kID[i+1][j+1], kID[i+1][j])

    mapdl.aesize("ALL", 1)

    mapdl.csys(0)                # Activating Cartesian coordinate system


# Generating FE mesh

mapdl.mat(1)                     # Setting material type to 1
mapdl.secnum(1)                  # Setting section type to 1
mapdl.type(1)                    # Setting element type to 1

mapdl.mshkey(1)                  # Activating mapped meshing
mapdl.amesh("ALL")               # Meshing all areas


# Boundary conditions - bottom

mapdl.real(1)                            # Setting element real constant to 1
mapdl.type(2)                            # Setting element type to 2

mapdl.nsel("S", "LOC", "Z", 0)           # Selecting all nodes at the bottom
mapdl.esurf()                            # Generating contact elements
mapdl.nsel("ALL")                        # Reselecting all nodes

mapdl.type(3)                            # Setting element type to 3

RPbtm = mapdl.n("", 0, 0, 0, mute=False) # Creating bottom reference node
mapdl.tshap("PILO")                      # Activating pilot node type target surface
mapdl.e(RPbtm)                           # Creating target element from reference node
mapdl.tshap()                            # Resetting target surface activation

mapdl.d(RPbtm, "UX", 0)                  # Defining BC in bottom reference node
mapdl.d(RPbtm, "UY", 0)
mapdl.d(RPbtm, "UZ", 0)
mapdl.d(RPbtm, "ROTX", 0)
mapdl.d(RPbtm, "ROTZ", 0)

if LoadType == "M" and StatSys == "clmp":
    if LoadApl == "def":
        mapdl.d(RPbtm, "ROTY", -rY)
```

```
    else:
        mapdl.f(RPbtm, "MY", -M)
else:
    mapdl.d(RPbtm, "ROTY", 0)


# Boundary conditions - top

mapdl.real(2)                           # Setting element real constant to 2
mapdl.type(2)                           # Setting element type to 2

mapdl.seltol(1.0e-6)                    # Defining selection tolerance
mapdl.nsel("S", "LOC", "Z", L)          # Selecting all nodes at the top
mapdl.esurf()                           # Generating contact elements
mapdl.nsel("ALL")                       # Reselecting all nodes

mapdl.type(3)                           # Setting element type to 3

RPtop = mapdl.n("", 0, 0, L, mute=False)  # Creating top reference node
mapdl.tshap("PILO")                     # Activating pilot node type target surface
mapdl.e(RPtop)                          # Creating target element from reference node
mapdl.tshap()                           # Resetting target surface activation
mapdl.components["compRPtop"] = "NODE", [RPtop]

if StatSys == "clmp":                   # Defining BC in top reference node
    mapdl.d(RPtop, "UX", 0)
    mapdl.d(RPtop, "UY", 0)
    mapdl.d(RPtop, "ROTX", 0)
    mapdl.d(RPtop, "ROTZ", 0)
    if LoadType == "N":
        mapdl.d(RPtop, "ROTY", 0)
elif CylSize == 1:
    mapdl.d(RPtop, "UY", 0)
    mapdl.d(RPtop, "ROTX", 0)
    mapdl.d(RPtop, "ROTZ", 0)

if LoadType == "N":
    if LoadApl == "def":
        mapdl.d(RPtop, "UZ", -uZ)
    else:
        mapdl.f(RPtop, "FZ", -N)
elif LoadType == "V":
    if LoadApl == "def":
        mapdl.d(RPtop, "UX", uX)
        mapdl.d(RPtop, "ROTY", rY)
    else:
        mapdl.f(RPtop, "FX", V)
        mapdl.f(RPtop, "MY", M)
elif LoadApl == "def":
    mapdl.d(RPtop, "ROTY", rY)
else:
    mapdl.f(RPtop, "MY", M)


# Boundary conditions - symmetry plane

if CylSize == 1:
    mapdl.nsel("S", "LOC", "Y", 0)      # Selecting all nodes on symmetry plane
    mapdl.nsel("U", "LOC", "Z", 0)      # Unselecting nodes at the bottom
    mapdl.nsel("U", "LOC", "Z", L)      # Unselecting nodes at the top
    mapdl.dsym("SYMM", "Y")             # Defining symmetry DOF
    mapdl.nsel("ALL")                   # Reselecting all nodes


```

```
# Plotting

mapdl.eplot()                              # Plotting FE mesh


# Exiting normally from preprocessor

mapdl.allsel()
mapdl.finish()
```

Program code B.4: Linear analysis - solution and postprocessing

```
if AnaType == "LBA":

  # Static analysis with prestress effects (LA)

    mapdl.slashsolu()                      # Entering solution processor

    mapdl.antype("STATIC")                 # Starting a new static analysis
    mapdl.pstres("ON")                     # Activating prestress effects
    mapdl.time(1)                          # Setting the time for the load step
    output = mapdl.solve(mute=False)       # Solving the problem + extracting solution info
    print(output)                          # Printing solution info

    mapdl.finish()                         # Exiting normally from solution processor


  # Postprocessing LA results

    mapdl.post1()                          # Entering postprocessor

    mapdl.nsel("S", "NODE", "", RPbtm)     # Selecting constrained bottom node
    reactF = mapdl.prrsol("F", mute=False).to_list() # Extracting reaction forces
    reactM = mapdl.prrsol("M", mute=False).to_list() # Extracting reaction moments
    print("RFbtm: ", reactF)               # Printing reaction forces
    print("RMbtm: ", reactM)               # Printing reaction moments
    mapdl.nsel("ALL")                      # Selecting all nodes

    if StatSys == "clmp" or CylSize == 1:
        mapdl.nsel("S", "NODE", "", RPtop)  # Selecting constrained top node
        reactF = mapdl.prrsol("F", mute=False).to_list() # Extracting reaction forces
        reactM = mapdl.prrsol("M", mute=False).to_list() # Extracting reaction moments
        print("RFtop: ", reactF)           # Printing reaction forces
        print("RMtop: ", reactM)           # Printing reaction moments
        mapdl.nsel("ALL")                  # Selecting all nodes

    mapdl.finish()                         # Exiting normally from postprocessor


  # Eigenvalue buckling analysis (LBA)

    mapdl.slashsolu()                      # Entering solution processor

    mapdl.antype("BUCKLE")                 # Starting a new buckling analysis
    mapdl.bucopt("LANB", NumMode, 0, "", "RANGE")  # Specifying buckling analysis options
    mapdl.mxpand()                         # Expanding and writing mode shapes
    output = mapdl.solve(mute=False)       # Solving the problem + extracting solution info
    print(output)                          # Printing solution info

    mapdl.finish()                         # Exiting normally from solution processor


  # Postprocessing LBA results
```

```
52
53      mapdl.post1()                           # Entering postprocessor
54
55      mapdl.set(sbstep=1)                     # Activating buckling mode 1
56      LMB = mapdl.post_processing.time        # Extracting buckling load multiplier
57      print("LMB: ", LMB)                     # Printing buckling load multiplier of mode 1
58
59      if 1 == 1:                              # Plotting buckling mode shapes
60          mapdl.set("FIRST")
61          for i in range(1, NumMode+1):
62              mapdl.post_processing.plot_nodal_displacement("NORM", smooth_shading=True)
63              mapdl.set("NEXT")
64
65      mapdl.finish()                          # Exiting normally from postprocessor
```

Program code B.5: Nonlinear analysis - solution and postprocessing

```
1   if AnaType == "GNA" or AnaType == "MNA" or AnaType == "GMNA":
2
3     # Static analysis with nonlinearity
4
5       mapdl.slashsolu()                       # Entering solution processor
6
7       mapdl.antype("STATIC")                  # Starting a new static analysis
8       mapdl.time(1)                           # Setting the time for the load step
9
10      if AnaType == "GNA" or AnaType == "GMNA":
11          mapdl.nlgeom("ON")                    # Activating geometric nonlinearity
12
13      if SolMthd == "NRM":                    # Options for Newton-Raphson method
14          mapdl.nropt("FULL", "", "ON")         # Full Newton-Raphson with symmetric matrices
15          mapdl.lnsrch("AUTO")                  # Automatic line search
16          mapdl.nsubst(NumSbst, 10000, NumSbst) # Specifying the number of substeps
17      elif SolMthd == "ALM":                  # Options for arc-length method
18          mapdl.autots("OFF")                   # Disableing automatic time stepping
19          mapdl.nsubst(NumSbst)                 # Specifying initial number of substeps
20          mapdl.arclen("ON", 1, 1/1000)         # Activating arc-length method
21          mapdl.arctrm("L")                     # Enableing termination at limit point
22
23      mapdl.outres("ALL", "NONE")             # Resetting solution data output
24      mapdl.outres("NSOL", "ALL", "compRPtop")
25      output = mapdl.solve(mute=False)        # Solving the problem + extracting solution info
26      print(output)                           # Printing solution info
27
28      mapdl.finish()                          # Exiting normally from solution processor
29
30
31    # Postprocessing results from nonlinear analysis
32
33      mapdl.post1()                           # Entering postprocessor
34
35      n = int(mapdl.solution.n_cmss)          # Number of substeps in the analysis
36
37      if LoadApl == "def":
38          DPF = [0.0]
39          FX = [0.0]
40          FZ = [0.0]
41          MY = [0.0]
42          mapdl.nsel("S", "NODE", "", RPbtm)    # Selecting bottom reference node
43          mapdl.set("FIRST")                    # Activating first substep
44          for i in range(1, n+1):
45              res0 = mapdl.post_processing.time
46              res1 = mapdl.prrsol("FX", mute=False).to_list()
```

```
            res2 = mapdl.prrsol("FZ", mute=False).to_list()
            res3 = mapdl.prrsol("MY", mute=False).to_list()
            DPF = np.concat((DPF, [res0[]))      # Deformation proportionality factors [-]
            FX = np.concat((FX, [res1[0][1]]))  # Horizontal reactions [MN]
            FZ = np.concat((FZ, [res2[0][1]]))  # Vertical reactions [MN]
            MY = np.concat((MY, [res3[0][1]]))  # Bending moment reactions [MNm]
            mapdl.set("NEXT")                   # Activating next substep
        mapdl.nsel("ALL")                    # Selecting all nodes
        print("DPF: ", DPF)
        print("FX: ", FX)
        print("FZ: ", FZ)
        print("MY: ", MY)

        plt.plot(DPF, FX, "b-o")
        plt.xlabel("Deformation proportionality factor [-]")
        plt.ylabel("Horizontal reaction in bottom RP [MN]")
        plt.show()

        plt.plot(DPF, FZ, "b-o")
        plt.xlabel("Deformation proportionality factor [-]")
        plt.ylabel("Vertical reaction in bottom RP [MN]")
        plt.show()

        plt.plot(DPF, MY, "b-o")
        plt.xlabel("Deformation proportionality factor [-]")
        plt.ylabel("Bending moment reaction in bottom RP [MN]")
        plt.show()

    elif LoadApl == "for":
        LPF  = [0.0]
        disX = [0.0]
        disZ = [0.0]
        rotY = [0.0]
        mapdl.nsel("S", "NODE", "", RPtop)    # Selecting top reference node
        mapdl.set("FIRST")                    # Activating first substep
        for i in range(1, n+1):
            res0 = mapdl.post_processing.time
            res1 = mapdl.post_processing.nodal_displacement("X")
            res2 = mapdl.post_processing.nodal_displacement("Z")
            res3 = mapdl.post_processing.nodal_rotation("Y")
            LPF  = np.concat((LPF, [res0]))         # Load proportionality factors [-]
            disX = np.concat((disX, res1.tolist())) # Horizontal displacement of top RP [m]
            disZ = np.concat((disZ, res2.tolist())) # Vertical displacements of top RP [m]
            rotY = np.concat((rotY, res3.tolist())) # Rotation of top RP [rad]
            mapdl.set("NEXT")                       # Activating next substep
        mapdl.nsel("ALL")                    # Selecting all nodes
        print("LPF: ", LPF)
        print("disX: ", disX)
        print("disZ: ", disZ)
        print("rotY: ", rotY)

        plt.plot(disX, LPF, "b-o")
        plt.xlabel("Horizontal displacement of top RP [m]")
        plt.ylabel("Load proportionality factor [-]")
        plt.show()

        plt.plot(disZ, LPF, "b-o")
        plt.xlabel("Vertical displacement of top RP [m]")
        plt.ylabel("Load proportionality factor [-]")
        plt.show()

        plt.plot(rotY, LPF, "b-o")
        plt.xlabel("Rotation of top RP [rad]")
        plt.ylabel("Load proportionality factor [-]")
```

```
111         plt.show()
112
113     mapdl.finish()                          # Exiting normally from postprocessor
```

Program code B.6: Exit MAPDL

```
1 mapdl.exit()
```

This page is intentionally left blank.


STUDENT REPORT
AALBORG UNIVERSITY